THE DESIGN OF A HONEYCOMB BICYCLE HELMET FOR PREVENTION OF

TRAUMATIC BRAIN INJURY

THE DESIGN OF A HONEYCOMB BICYCLE HELMET FOR PREVENTION OF

TRAUMATIC BRAIN INJURY

By ANNIE KING, B.A.Sc.

A Thesis Submitted to the School of Graduate Studies in Partial Fulfilment of the Requirements

for the Degree Master of Applied Science

McMaster University MASTER OF APPLIED SCIENCE (2023) Hamilton, Ontario

(School of Biomedical Engineering)

TITLE:	The design of a honeycomb bicycle helmet for prevention of traumatic brain injury
AUTHOR:	Annie King, B.A.Sc. (Queen's University)
SUPERVISORS:	Cheryl E. Quenneville, B.A.Sc., M.E.Sc., Ph.D.
	Bosco Yu, B.A.Sc., M.A.Sc., Ph.D.
NUMBER OF PAGES:	xv, 146

Lay Abstract

Traditional foam bicycle helmets prevent skull fracture, but do not prevent many brain injuries, such as concussion. Honeycomb could be a suitable alternative due to its ability to absorb energy in the loading direction that causes head rotation, to prevent brain injuries. An elastic honeycomb helmet design was proposed to protect against brain injury and to be reusable for multiple impacts.

Quasi-static testing was performed on flat honeycomb samples to determine the most suitable design. The honeycomb design was scaled for real-world impacts and the design was incorporated into the form of a full-scale helmet. Helmet prototypes were 3D-printed for future testing.

This work presented a new helmet design that has potential to prevent brain injury in a bicycle accident, and as such, reduce its social and economic burden. As well, the honeycomb helmet design showed potential for reusability, which would have substantial benefits to consumers.

Abstract

Bicycling is a popular activity around the world and a frequent source of head injury. Traditional expanded polystyrene (EPS) foam helmets reduce the risk of skull fracture (caused by the radial contact forces), but do not reduce the risk of diffuse traumatic brain injury (TBI), such as concussion (caused by rotational motion of the head from the tangential forces). Hexagonal honeycomb could be suitable for head protection due to its energy absorbing capabilities and anisotropy, where it is weaker under shear loading to reduce rotation. Therefore, a helmet design was proposed that is made of hexagonal honeycomb with 5-7 defects to accommodate the curvature of the head and made of thermoplastic polyurethane (TPU) to be potentially reusable for multiple impacts.

The properties of flat honeycomb samples were explored, where 3D-printing was employed for rapid prototyping. Two arrangements of 5-7 defects were tested and shown to decrease the strength of the honeycomb. A relative density most suitable for head protection was determined based on the results of quasi-static compression and shear testing.

As real-world accidents occur at higher rates, dynamic impact tests were performed on the chosen honeycomb design, with various impact conditions. Honeycomb showed greater anisotropy than EPS foam, which is beneficial for diffuse TBI protection, and potential to be reusable. The results were used to scale the honeycomb design for dynamic impact conditions. A helmet model was developed based on the geometry of an existing EPS foam helmet and helmet prototypes were 3D-printed to be used in future drop tower impact tests.

This work presented a new helmet design that has potential to reduce the risk of sustaining TBI in a bicycle accident, and as such, reduce its social and economic burden. As well, the

honeycomb helmet design showed potential for reusability, which would have substantial benefits

to consumers.

Acknowledgements

I would like to begin by thanking my supervisors, Dr. Cheryl Quenneville and Dr. Bosco Yu for their mentorship. I appreciate the opportunity to do my Master's degree under your guidance and it was a pleasure to work with you. Your encouragement, support, and positivity in facing challenges were motivating and inspiring. I have learned so much from both of you.

Thank you to everyone who contributed to the success of this project. Dr Wohl, thank you for your valuable insight and guidance as a member of my supervisory committee. Thank you to Tarick at Seven Star Sports for providing me with knowledge on the helmet industry and the helmet manufacturing process. Thank you to Dr. Oren Petel and Jenny at Carleton University for their collaboration in drop tower testing. Thank you to Michael, Mark, John, and Rob in the machine shop. You were an incredible support team through my Master's degree and taught me so much. Your patience is greatly appreciated. Days in the machine shop with you were some of my favourites.

Thank you to my lab mates in the Injury Biomechanics and Hybrid Materials Labs: Julia, Ali, Julian, Ariana, Fatemeh, Liam, Carson, Cole, Ary, Adam, Sarah, and Charlotte. An extra special thanks to Julia for being such a great mentor and friend.

Thank you to all of my friends and family for your support. Thank you to my sisters for encouraging me and always being only a phone call away. Thank you to my parents for being the reason I love and am passionate about scientific research. Dad, thank you for sharing your statistics expertise, working through research challenges with me on the phone, and caring so much about my work every step of the way. Mom, thank you for sending me every helmet paper you came

across, being as passionate about my work as I am, and having so much confidence in me. Thank you to my partner, Brodie, for being my biggest support – I am so grateful for you.

Table of Contents

List of Figures

List of Tables

List of Abbreviations and Symbols

°	Degree
%	Percent
±	Plus/minus
EPS	Expanded polystyrene
TBI	Traumatic Brain Injury
DAI	Diffuse Axonal Injury
NFL	National Football League
ATD	Anthropomorphic test device
FEA	Finite element analysis
FEM	Finite element modeling
AIS	Abbreviated Injury Score
BrIC	Brain Injury Criteria
UBrIC	Universal Brain Injury Criteria
MIPS	Multidirectional Impact Protection System
CPSC	Consumer Product Safety Commission
ASTM	American Society for Testing and Materials
ISO	International Organization for Standardization
NOCSAE	National Operating Committee on Standards for Athletic Equipment
FDM	Fused Deposition Modeling
SLS	Selective Laser Sintering
3D	Three-dimensional

N	Sample size
ρ	Density
$\bar{\rho}$	Relative density
$\bar{\rho}_{lower}$	Lower relative density limit
$\bar{\rho}_{upper}$	Upper relative density limit
U_v	Energy absorption per unit volume
σ	Compressive stress
ε	Compressive strain
$\dot{\varepsilon}$	Compressive strain rate
σ_p	Peak compressive stress
σ_c	Compressive stress threshold for skull fracture
τ	Shear stress
δ	Shear strain
$\dot{\delta}$	Shear strain rate
τ_p	Peak shear stress
G	Shear modulus
v_i	Impact velocity
MPa	Megapascal
kJ	Kilojoules
N	Newtons
kN	Kilonewtons
m	Metres

mm   Millimetres

s   Seconds

Declaration of Academic Achievement

The following is a declaration that I, Annie King, completed the research outlined in this thesis and recognize the contributions of Dr. Cheryl Quenneville, Dr. Bosco Yu, Dr. Oren Petel, Jennifer Rovt, and Charlotte Fleet. I contributed to the helmet conceptualization and the study design. I developed design objectives, developed testing protocols, performed testing, analyzed data, and wrote the thesis document. Dr. Cheryl Quenneville and Dr. Bosco Yu contributed to the helmet conceptualization and study design, reviewed the experimental methods, and reviewed this thesis document. Dr. Oren Petel, Jennifer Rovt, and Charlotte Fleet helped perform tests and collect data.

Chapter 1 – Introduction

Overview: Bicycling is a popular activity around the world and a frequent source of head injury. Limitations of current helmets suggest the need for a new design. This chapter outlines the anatomy of the head and brain, the forces present in real-world bicycle accidents, common head injuries, and current gaps in helmet design and testing. A new bicycle helmet concept is introduced, and study objectives are defined for developing and testing the design.[1]

1.1   Motivation

Bicycling is a popular activity around the world as a form of exercise and means of transportation. Although bicycling provides health benefits [1], it is also a frequent source of injury. Over 600,000 individuals are treated in emergency rooms in the United States for bicycle-related injuries each year [2]. Of these, about 30% involve head injuries [2], which include skull fracture, facial fracture, and traumatic brain injury (TBI) [3]. Further, head injuries are the most common cause of death in bicycle-related accidents [4–6]. A case-control study that looked at coroner's data from bicycle-related fatalities in Canada determined that 55% were caused by head injuries [6]. Non-fatal head injuries also have long-term effects on quality of life, primarily due to irreversible brain damage [7]. The economic cost to society due to bicycle-related head injuries is estimated at approximately $3 billion per year in the United States [2].

---

[1] Due to the interdisciplinary nature of this work, a glossary of frequently used anatomical terms is included in Appendix A.

Traumatic brain injury is one of the leading causes of disability around the world and contributes to approximately 30% of all injury deaths [8]. Bicycling is the leading cause of sports-related TBIs treated in US emergency departments [9]. According to the Centers for Disease Control and Prevention, 596,972 individuals were treated in US emergency rooms for bicycle-related TBIs from 2009 to 2018 [10]. This number is likely even higher since less-severe head injuries are often not treated in emergency rooms and therefore go unreported [11].

Traditional expanded polystyrene (EPS) foam helmets effectively reduce the risk of fractures and severe TBI [12–14]. However, there is no scientific evidence that EPS foam helmets reduce the risk of diffuse TBI, such as concussion. Therefore, there is a need for advanced bicycle helmet technology that provides enhanced protection to reduce the frequency of TBI, and its social and economic burden.

1.2   Anatomy of the Head and Brain

The skull, also called the cranium, is a bony structure that encloses the brain (Figure 1.1). The brain is a complex organ, that with the spinal cord, makes up the central nervous system [15]. The brain has three parts: the cerebrum, the cerebellum, and the brainstem. The cerebrum makes up the majority of the brain's volume and is made up of two types of brain tissue: the cortex/grey matter and the white matter [16].
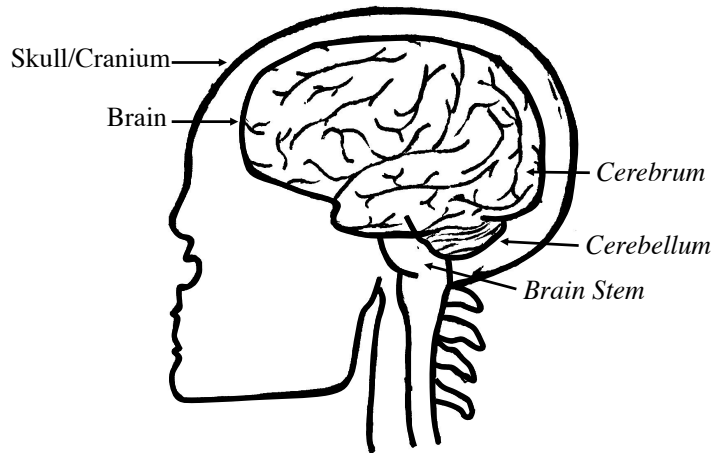
Figure 1.1: The Human Brain and Skull
The skull/cranium encloses the brain, which is made up of the cerebrum, cerebellum, and brain stem.

Under the cranium are the meninges – three membranes with the function of protecting the brain against trauma (Figure 1.2). The membrane closest to the skull is called the *dura mater*, which is a thick, strong layer of connective tissue. The term epidural refers to the space between the skull and the dura mater. Under the *dura mater* is the *arachnoid mater*, which is a thin membrane with a spiderweb-like appearance. Around the surface of the brain is the *pia mater*, which allows the flow of blood vessels to the brain tissue and helps to contain cerebrospinal fluid [15].
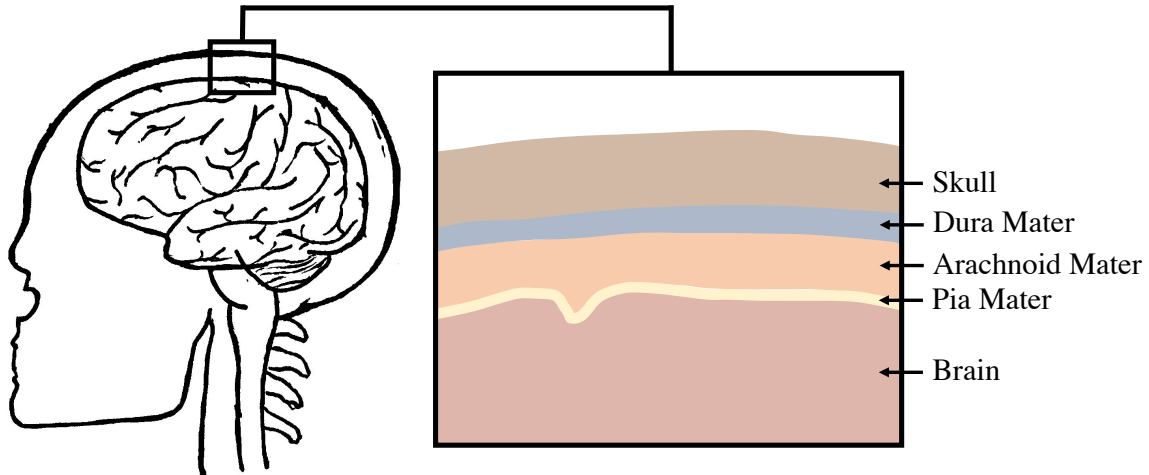
Figure 1.2: The Meninges
There are three layers of membrane under the cranium that make up the meninges, including the *dura mater*, *arachnoid mater,* and *pia mater*.

Neurons are the functional cells of the brain that transmit signals to other nerve cells, muscles, or gland cells. Neurons are made up of a cell body, an axon, and dendrites (Figure 1.3). Signals are received through the dendrites and then travel through the axon until the synapse, where the signals are then passed on to other neurons [17].
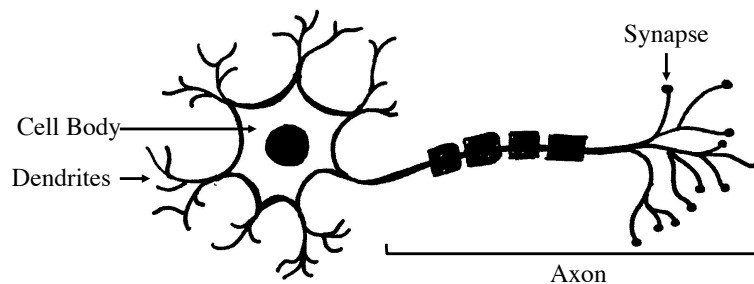
Figure 1.3: The Brain's Neurons
The three parts of a neuron (the functional cell of the brain) are the cell body, axon, and dendrites.

1.3   Head Impacts in Bicycle Accidents

Bicycle accidents can be caused by a variety of circumstances including interaction with other road users, failure of a bicycle component, or collision with road hazards or fixed objects [18]. Bicycle accidents are most commonly due to collisions with a motor vehicle or due to a cyclist fall [19]. The most common injury locations are to the upper extremities, lower extremities, and the head, which makes up 32%-50% of the cases [20, 21].

Head injuries are often caused by blunt impacts, which are typically oblique with respect to the impact surface, where radial and tangential force components are induced (Figure 1.4) [22–24]. The oblique impact force is made up of a radial force component that induces linear head kinematics, and a tangential force component that induces rotational head kinematics. Both the contact forces and the resulting inertial forces on the head are common injury mechanisms [25, 26].
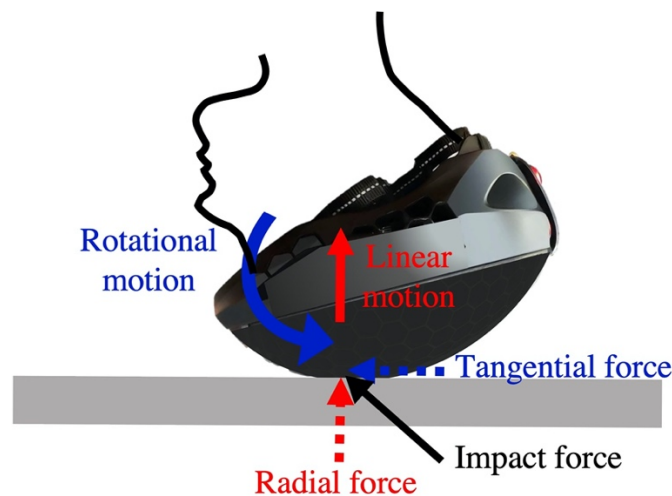
Figure 1.4: Loads and Head Motion in an Oblique Impact
Radial and tangential forces are transmitted to the head in an oblique impact, causing linear and rotational motion of the head, respectively.

In collisions with a motor vehicle, cyclist head impacts are usually to the hood, windshield, or roof of the vehicle [21]. From real-world accident reconstruction simulations involving a motor vehicle, the mean resultant head impact velocity was found to be 6.8 ± 2.7 m/s [22]. The average radial and tangential velocity components were 5.5 ± 3.0 m/s and 3.4 ± 2.1 m/s, respectively. In cyclist falls, two impact scenarios are common – falls after skidding and falls after hitting a curb, where in both, a head impact is typically with the ground [23].

1.4   Head Injury

Head injury includes skull fracture, facial fracture, and TBI [3]. The mechanisms of these injuries are relevant to understanding the limitations of current bicycle helmets and the gaps to be addressed with advanced helmet technology and testing.

1.4.1   Skull Fracture

Skull fractures are any break in the cranial bone and are present in 45–58% of patients admitted to the hospital following an accident that occurred while riding a bicycle [27, 28]. Skull fracture is caused by the radial force component of an impact causing stress to the cranial bone at the point of impact that exceeds its strength [29]. The risk of sustaining a skull fracture is typically measured according to peak linear acceleration, as this metric correlates with the level of stress on the skull [30]. Helmets have been specifically designed for the prevention of skull fracture and are tested through linear drop tests that induce the skull fracture mechanism of high contact stresses and linear head kinematics (Section 1.6). EPS foam helmets have been shown to reduce linear head acceleration by 67-78%, reducing the risk of skull fracture from 99.9% to 9.3-30.6% for impact velocities of 5.4 m/s and 6.3 m/s [12]. As well, according to real-world accident data that

considered patients admitted to the hospital following any type of bicycle-related accident, helmets reduce the incidence of skull fracture from 57% to 15% [28].

1.4.2   Focal Traumatic Brain Injury

Traumatic brain injury (TBI) is defined as damage to the brain as the result of a direct or inertial impact and can be categorized into two groups: focal injury and diffuse injury [31]. Focal injury occurs in a specific location of the brain and includes hematomas and contusions [32].

Hematomas (collection of blood in the brain) and contusions (bruising to the brain) are often a direct result of skull deformation following fracture [33]. Specifically, epidural hematoma is attributed to skull fracture in 90% of cases [34], where arteries between the *dura* and skull are torn [31]. Subdural hematomas are caused by the tearing of bridging veins between the *dura* and *arachnoid mater* [31]. A previous study based on autopsy data reported skull fractures to be present in 67% of patients with acute subdural hematoma [35]. Cerebral contusions at the site of impact (coup contusions) were found to be preceded by skull fracture in 60-80% of cases, caused by brain surface damage from skull deformation [31]. For all of the above focal TBIs that follow skull fracture, the injury mechanism is normal stress on the skull and the injury tolerance can be characterized by the skull fracture threshold.

There is also evidence that rotational motion can be the cause of focal injuries such as subdural hematoma, intracerebral hematoma, and cerebral contusions. In cases of subdural hematoma that do not follow a skull fracture, the blood vessels connecting the brain and the skull are stretched and torn by the relative motion during rotation of the head [36]. Intracerebral hematoma refers to bleeding within the functional brain tissue [31]. Brain strain is considered to be the main cause of ruptured cerebral veins and arteries [37]. Due to the brain's susceptibility to

strain from shear loading, rotational acceleration is the most likely injury predictor [38]. As well, contusions in the absence of skull fracture are associated with the shearing of the brain tissue against rough interior surfaces of the skull [31].

According to real-world data on patients admitted to the hospital following a bicycle-related accident, helmets were somewhat effective at protecting against focal TBIs, where the use of a helmet reduced the incidence of epidural hematoma from 31% to 11%, subdural hematoma from 30% to 7%, and contusions from 25% to 15% [28].

1.4.3   Diffuse Traumatic Brain Injury

Diffuse TBI occurs in a widespread area and includes concussion and diffuse axonal injury (DAI) [31]. DAI is diagnosed when there is severe physical damage to the brain's axons [31]. Concussion is defined by its associated symptomology as an alteration in mental functioning [39], which may involve unconsciousness and amnesia [40]. From a biomechanical point of view, concussion is synonymous with mild TBI – some form of damage to the brain as the result of a direct or inertial impact, and can include less-severe DAI [41]. It has been inferred that the symptomatology associated with concussion is representative of mechanical damage (cell death) in the regions of the brain associated with those particular functions [40]. For example, amnesia indicates damage to brain structures, such as the thalamus, that form the limbic system [42].

Therefore, research has focused on investigating tissue-level damage that may affect the transmission of signals through the brain, where *in vitro* models have shown that brain cell death is directly related to the amount of strain the tissue experiences and at what strain rate [44–46]. For example, biaxial stretching was applied to tissue from the rat cortex and cell death was

quantified for four days following. Strain, strain rate, and time post-stretching all significantly affected cell death [43].

Specifically, strain/damage in the brain's axons is thought to be a primary pathologic process indicative of diffuse TBI [47–51]. The biomechanics of axonal injury during trauma is explained by the brain's viscoelastic tissue properties [46], which means it behaves differently under varying loading conditions, and more specifically, its stiffness depends on the rate at which deformation occurs. During daily activities, axons in the brain are often deformed and subsequently restored to their original geometry without experiencing permanent damage [47]. However, during trauma, where deformation occurs rapidly, the brain tissue is much less ductile [49, 50]. In this case, on a microscopic scale, the uniaxial elongation of axons results in permanent breakage of the microtubules or complete disconnection from the neuron [47]. On a macroscopic scale and in severe cases, the result is tearing of the brain tissue [47]. Due to the importance of the brain's viscoelastic properties, axonal injury is dependent on both the magnitude of strain and the strain rate [47]. This injury mechanism applies across the severity spectrum from concussion to DAI, with the primary difference across the spectrum being the amount of brain tissue injured and the severity of injury at a given site within the brain [50].

Brain tissue is much more resistant to compressive loading than shear loading, with a bulk modulus of five to six orders of magnitude greater than the shear modulus [38]. This means the brain undergoes little change in size due to hydrostatic forces but provides limited resistance to changes in shape. Therefore, shear deformation is most likely to cause excessive brain tissue damage associated with TBI.

It has been inferred that these injurious brain strains are caused by the motion of the head following an impact event and therefore studies have examined the relationship between various

head kinematics and resulting brain strain. Rotational head motion has been linked to injurious levels of brain strain using *in vitro* models, monkeys, humans, and finite element analysis (FEA). Holbourn [25] first proposed rotational motion rather than linear motion of the head as the mechanism for brain injury. By modeling the brain as a homogeneous and incompressible 2D gel, it was determined that rotational motion had a greater influence on the levels of shear strain in the brain tissue compared to linear motion [25]. The prevalence of concussion following oblique versus linear impacts also suggests that rotational motion is the primary injury mechanism. For example, a study subjected squirrel monkeys to non-contact sagittal plane head motion [51]. Half were subjected to pure linear motion of the head, where the animals did not experience cerebral concussion. The other half were subjected to pure rotational motion of the head, where concussion was induced in all of the animals. Brain lesions were visible more frequently and at higher severity in the rotation group compared to the linear translation group [51]. FEA has shown that rotational head motion produces much higher magnitudes of strain in the brain compared to linear head motion, where head impacts from National Football League (NFL) games and from frontal impact sled tests to an anthropometric test device (ATD) (crash test dummy) have been used as inputs to a finite element model (FEM) of the human head [53, 54].

Holbourn [25] postulated that following an impact, in the absence of skull deformation, the strains that arise in the brain are due to the change in velocity of the head, which involves a combination of a change in linear velocity and a change in rotational velocity about a particular axis. The strain experienced by the brain tissue is proportional to the amount of relative motion between constituent particles of the brain. Linear acceleration forces primarily produce compressive strains, which create little relative motion between constituent parts of the brain.

Therefore, rotational kinematics are primarily responsible for relative motion and are the most likely mechanism of diffuse TBI [25].

This supports the findings from real-world accident analysis that showed helmets do not reduce the incidence of concussion or DAI, and concussion is the most common injury for both helmeted and un-helmeted riders [14, 55].

1.4.4   Implications for Helmet Testing

The literature outlined above regarding head injury mechanisms suggests that skull fracture and associated brain injuries are primarily caused by contact stresses and linear kinematics, whereas brain injury in the absence of skull fracture is largely associated with rotational kinematics. Correspondingly, the most effective way to prevent skull fracture and hematoma/contusion secondary to skull fracture would be to minimize the magnitudes of linear acceleration and peak radial impact force. On the other hand, the most effective way to reduce the incidence of concussion, DAI, and some hematoma and contusion cases would be to minimize the magnitudes of rotational kinematics caused by the tangential force component of an impact.

In assessing the effectiveness of helmets to protect against brain injuries, experimental impact tests are performed using ATDs and the resulting kinematics of the headform are measured in an attempt to predict brain injury risk. In interpreting the results of these experimental tests, it is imperative to understand the relationship between various external measurements of head kinematics and strain in the brain tissue. Studies have used experimental impacts to inform FE simulations, which have shown that rotational velocity of the head correlates best to brain strain and direction-specific thresholds should be used to predict injury risk [56, 57]. Studies have also developed combined metrics for predicting brain injury risk. The Brain Injury Criteria (BrIC) was

developed to account for directional dependence by including the effect of rotational velocity around three axes, along with critical values that correspond to a 50% risk of Abbreviated Injury Scale (AIS) 4+ brain injury [57]. The Universal Brain Injury Criteria (UBrIC) builds on the BrIC to include the effect of rotational head velocity and acceleration around a particular axis [58].

1.5   Current Bicycle Helmets

The goal of a bicycle helmet is to prevent injury caused by an impact to the head. To prevent both skull fracture and TBI, helmets must absorb sufficient energy to mitigate linear and rotational head accelerations.

1.5.1   Traditional EPS Foam Helmets

Traditional bicycle helmets are composed of an outer shell, an energy-absorbing layer, and a strap/retention system [59]. Both the outer shell and the energy-absorbing layer contribute to the impact protection mechanism. The outer shell is typically made from polycarbonate and its purpose is to protect the head from penetration by sharp objects, as well as to distribute the impact force over a larger surface area [60]. The energy-absorbing layer is typically made from expanded polystyrene (EPS) foam [59]. EPS foam is a type of cellular solid in which polystyrene forms the edges and faces of gas-filled pockets (known as cells) (Figure 1.5) [61]. The impact force is transmitted to the EPS foam layer from the polycarbonate shell, and energy not absorbed by the foam is then transmitted to the head and may pose a risk of injury.
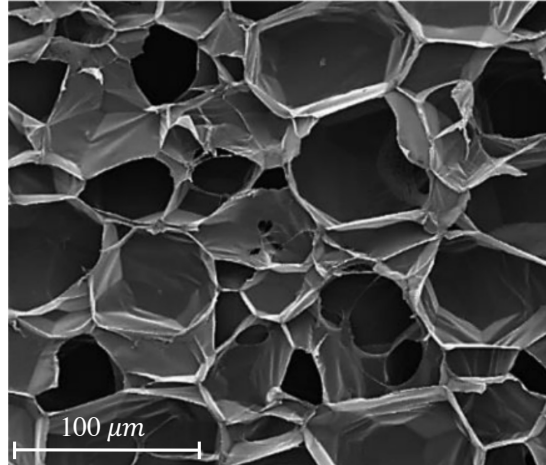
Figure 1.5: Cross-Sectional Micrography of EPS Foam
EPS foam, is the most commonly used material for bicycle helmets, is a closed cell foam with
the micrography shown (image adapted from [62]).

Since both radial and tangential force components contribute to the risk of head injury,
energy absorption in both the compressive and shear loading directions are relevant to studying
the effectiveness of EPS foam helmets. Under compressive stress the deformation mechanism of
EPS foam has three regimes: linear elastic, where the cell walls bend; plastic, where the cell walls
break; and densification, where the majority of the cell walls touch and the properties tend toward
those of the fully dense solid from which the foam is made (Figure 1.6) [61]. The amount of energy
the foam can absorb is given by strain energy – the area under the stress-strain curve up until
densification [61], typically defined as the global maximum of energy absorption efficiency [63].
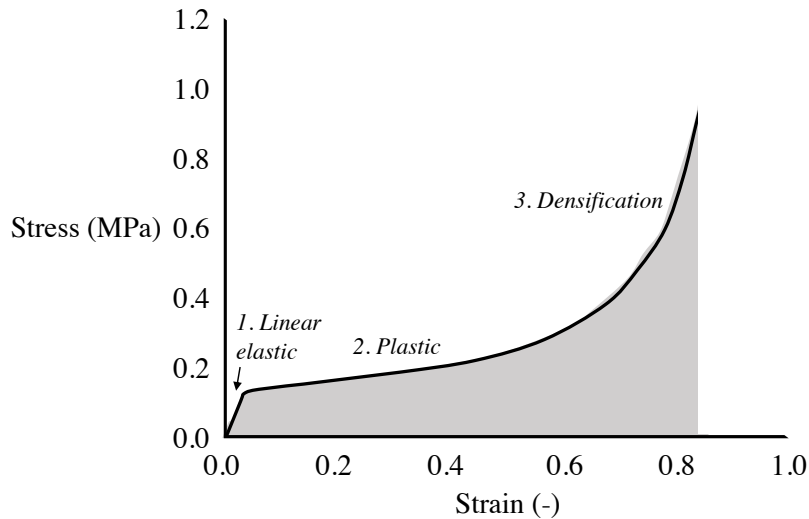
Figure 1.6: Stress-Strain Curve for EPS foam Under Compression
The stress-strain relationship for EPS foam under compressive loading is expected to have three regimes: linear-elastic, plastic, and densification.

EPS foam is effective in sufficiently reducing contact stress and linear head acceleration and therefore effective in preventing life-threatening injuries [12, 13]. On the other hand, EPS foam helmets have not been designed to prevent many types of TBI such as concussion and diffuse axonal injury [64]. The limitations of traditional helmets to protect the head in rotation are attributed to the mechanical response of the material – EPS foam does not sufficiently deform under shear loading to address rotational accelerations [61, 66] Shear stress that is not absorbed by helmet deformation or other mechanisms (such as sliding of the helmet on the human head [66]) is transferred to the head in the form of rotational acceleration. Due to its isotropic nature, the above limitations cannot be easily addressed by altering the characteristics of the EPS foam. For example, if the density and thickness of the EPS foam layer were altered to allow the material to undergo sufficient shear strain to prevent TBI, then there is a risk of the material compressing too easily and experiencing densification during severe impacts [67].

14

1.5.2   Helmets with Rotation-Damping Systems

Recently, bicycle helmets with dedicated rotation-damping systems have been introduced. Upon oblique impact, these helmets aim to mitigate shear stress transferred to the head by accommodating shear deformation themselves, while still protecting against radial contact forces [60, 67–69].

The most common rotation-damping system is the Multidirectional Impact Protection System (MIPS) (Täby, Sweden) slip liner [70] (Figure 1.7). The purpose of this thin polycarbonate plastic liner is to reduce the rotational acceleration of the head upon impact by permitting 10-15 mm of movement between the helmet and the head via a low-friction interface with the EPS foam layer [70]. The mechanism is supported by findings that movement between the head and helmet reduces peak rotational acceleration [71]. MIPS has been shown to reduce rotational acceleration by 22-28% and rotational velocity by 26-36% in oblique drop-tower impact tests, compared to EPS foam helmets [60, 69].

Figure 1.7: Bicycle Helmet with MIPS
MIPS, a thin polycarbonate plastic liner, is mounted inside an EPS foam helmet to reduce rotational head motion (image adapted from [72]).

WaveCel (Wilsonville, Oregon, USA) helmets contain a plastic cellular structure in addition to the EPS foam component, that acts to mitigate rotational kinematics (Figure 1.8) [70]. The cellular structure and the EPS foam make up approximately 15 mm and 10 mm of the thickness of the helmet, respectively [70]. Upon oblique impact, a built-in crease initiates folding of the cell walls to reduce peak linear acceleration [73]. Rotational acceleration is reduced by flexing/bending of the cell walls and gliding of the cellular structure relative to the EPS foam layer [73]. WaveCel has been shown to reduce rotational acceleration by 20-58%, rotational velocity by 39-70%, and linear acceleration by 15-25% in oblique drop-tower impact tests, compared to EPS foam helmets [69, 73].

Figure 1.8: WaveCel Bicycle Helmet
WaveCel helmets contain approximately 10 mm of EPS foam and 15 mm of a plastic cellular structure (image adapted from [75]).

HEXR helmets (HEXR, London, United Kingdom) are made with a polyamide-11 3D-printed honeycomb-like structure, based on 3D scans of the user's head geometry (Figure 1.9) [76]. Honeycomb was chosen due to its high strength-to-weight ratio, beneficial for safety and comfort to the wearer [76]. HEXR helmets omit the EPS foam component altogether and have been specifically designed for the mitigation of linear and rotational kinematics by permitting axial and shear deformation, respectively [76]. Impact testing performed by the company suggests that

HEXR helmets reduce linear acceleration, rotational acceleration, and rotational velocity on average by 26% compared to EPS foam helmets [76].
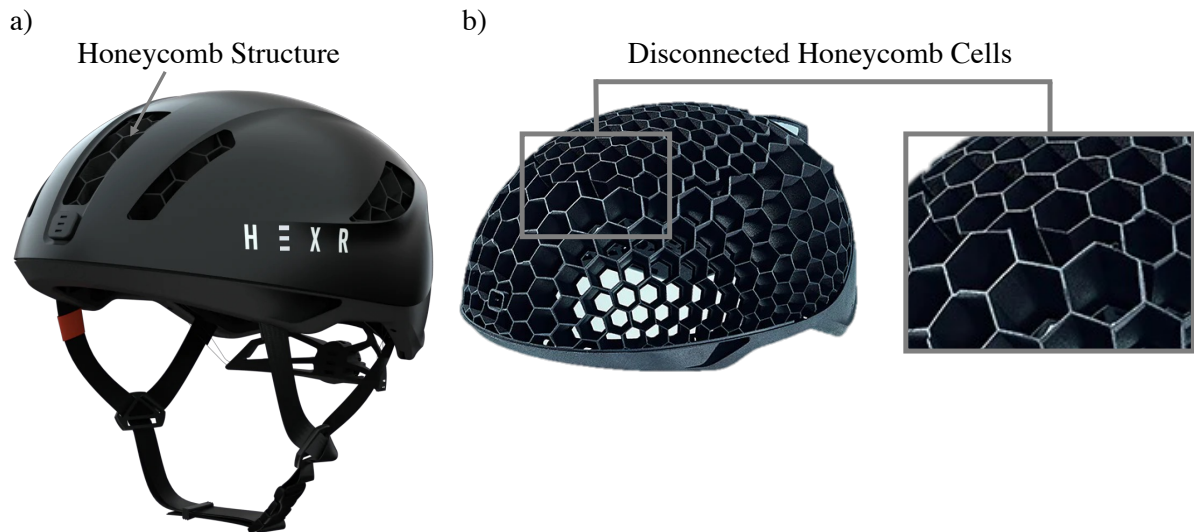
Figure 1.9: HEXR Bicycle Helmet
The HEXR helmet is made of a polyamide-11 3D-printed honeycomb-like structure. a) Shows a full helmet, b) shows the isolated honeycomb structure and highlights disconnected honeycomb cells (images adapted from [76]).

Although MIPS, WaveCel, and HEXR all improve upon EPS foam helmets in terms of mitigation of rotational kinematics, the risk of injury could be further reduced with future helmet technologies. Due to the limitations of EPS foam, it is hypothesized that a design with an alternate material than EPS foam altogether, like the HEXR helmet, would be beneficial. It has been observed that the HEXR's honeycomb structure is made of arrays of hexagons with disconnected cells, which may affect the impact attenuation capability in these areas (Figure 1.9b). As well, the above helmets absorb impact energy through plastic deformation, making them 'single-use' but despite this, people rarely discard their equipment after an impact. A helmet design capable of

providing protection for multiple impact events would therefore reduce the frequency of head injuries.

1.6   Helmet Testing Standards

Helmets sold in Canada must be certified by one of the following: Canadian Standards Association, Consumer Product Safety Commission (CPSC), Snell, or American Society for Testing and Materials (ASTM). All standards are similar and therefore the CPSC standard for bicycle helmets will be outlined here [77]. The standard includes requirements for peripheral vision range, positional stability, retention system strength, and impact attenuation. The impact attenuation test is the primary focus as it is most relevant to the protective characteristics of helmets.

1.6.1   Head and Neck

CPSC standards require the use of an International Organization for Standardization (ISO) headform for the impact attenuation tests (Figure 1.10a). The ISO headform is a rigid, solid model made of low-resonance K-1A magnesium alloy, in the shape of a human head. It is available in six different sizes (named A, C, E, J, M, and O) that represent different population anthropometrics. The headform size used during impact testing (per CPSC standard) is the smallest headform appropriate for the particular helmet, where the pads inside the helmet should be 'partially compressed'.
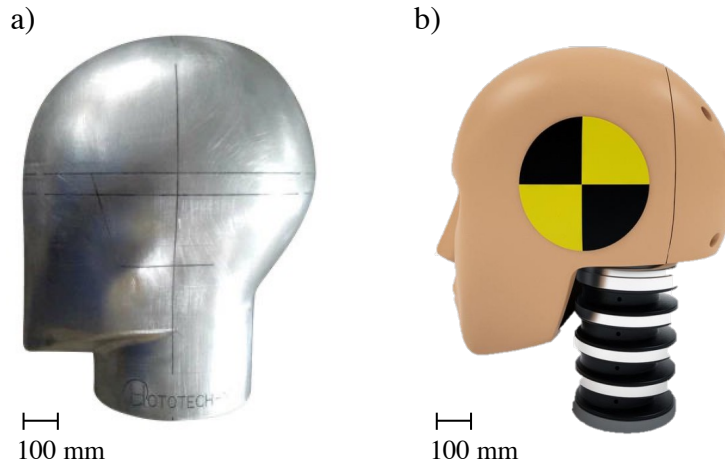
Figure 1.10: Headforms Used for Helmet Testing
a) The ISO headform is used for standard bicycle helmet impact attenuation testing (image adapted from [78]). b) The Hybrid III headform and neck are often used in advanced helmet testing involving oblique impacts (image adapted from [79]).

There are some limitations in using the ISO headform as a head surrogate. These limitations include an unrealistic head mass, unrealistic head inertia, and non-deformable skin [80]. Other surrogate headforms could be considered for helmet testing, such as the Hybrid III (Humanetics, Farmington Hills, Michigan, USA) ATD head (Figure 1.10b). Although the Hybrid III head was designed for safety testing in frontal automotive collisions, it has also been used extensively in oblique bicycle helmet testing [60, 69, 73]. Among ATD heads available, the Hybrid III has the most realistic head mass (4.5 kg), skin, and head inertia [80]. As well, the CPSC bicycle helmet test standard does not include the use of a surrogate neck. However, it has been hypothesized that the use of the Hybrid III neck (Figure 1.10b) leads to more realistic rotational head kinematics [80] and therefore has been used with the Hybrid III head in oblique bicycle helmet testing [60, 69, 73]. The Hybrid III ATD neck is made of a combination of rubber and aluminum discs to represent the vertebrae. However, its use is controversial since it is substantially stiffer than the human neck in

all directions of rotation [80–82]. As well, the Hybrid III neck was designed for use in automotive

frontal impact tests, to mimic flexion and extension in the sagittal plane only [84].

1.6.2   Impact Testing Setup

Two impact attenuation test apparatuses are shown in Figure 1.11, which are both

acceptable according to the CPSC standard.
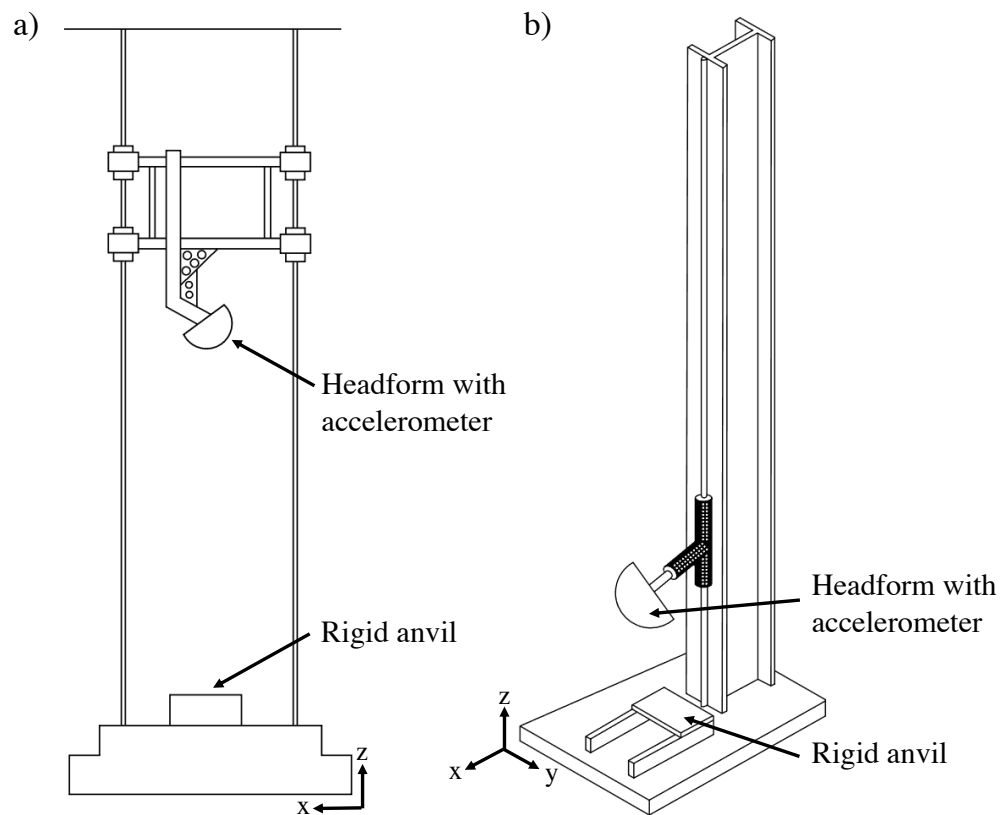
Figure 1.11: Standard Impact Attenuation Apparatuses
Two impact attenuation test apparatuses are acceptable according to the CPSC standard. a)
Shows a guidewire apparatus, and b) shows a monorail apparatus (images adapted from [77]).

In both test setups, the helmeted headform is rigidly attached and dropped in a guided free

fall onto a rigid anvil. Impacts are performed on three different solid steel anvils: flat,

hemispherical, and curbstone (Figure 1.12). The mass of the drop assembly should be 5.0 ± 0.1 kg

including the mass of the drop carriage and test headform. For impacts onto flat anvils, an impact

speed of 6.2 m/s is targeted. For impacts onto curbstone and hemispherical anvils, an impact speed

of 4.8 m/s is targeted.
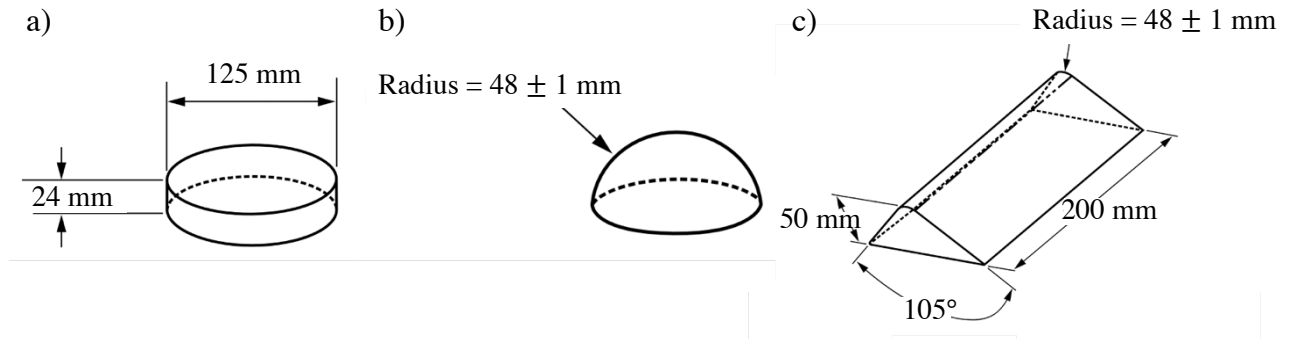
Figure 1.12: Geometry of Test Anvils
Standard impact attenuation testing involves impacts onto three impact surfaces including a) a
flat anvil, b) a hemispherical anvil, and c) a curbstone anvil. All dimensions are in millimetres
(image adapted from [77]).

This setup is for linear impacts, where only radial forces are transmitted to the head to

cause linear motion following impact (Figure 1.13a). As such, oblique testing methods are required

that induce both radial and tangential forces to the head upon impact, to assess the performance of

helmets in mitigating both linear and rotational head motion (Figure 1.13b).
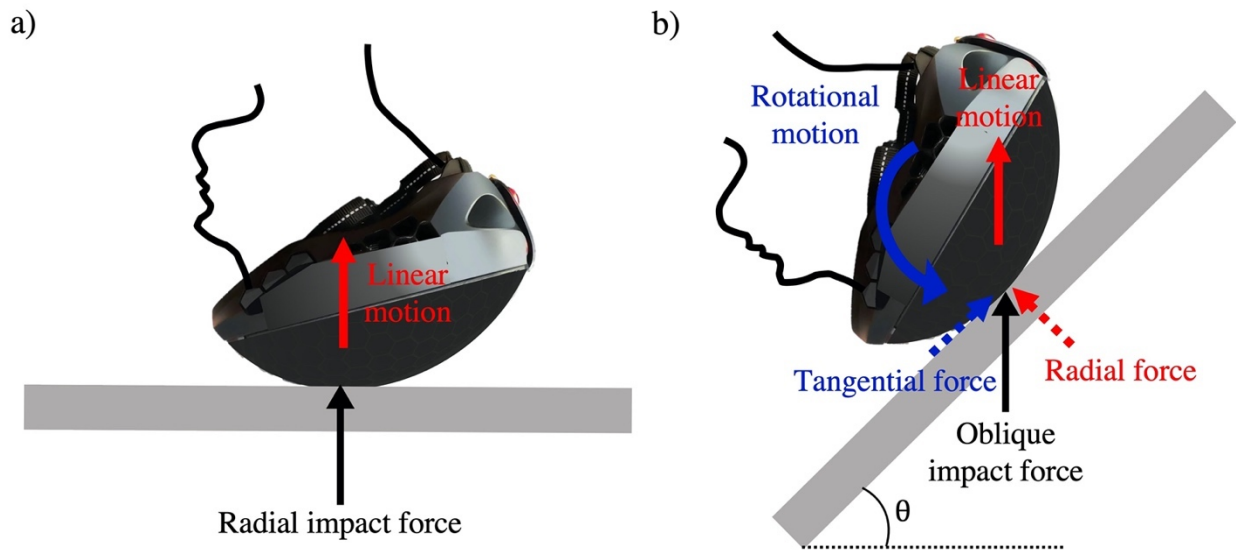
Figure 1.13: Loads and Head Motion in Radial and Oblique Impact Tests
a) Purely radial impact tests cause linear motion of the head. b) Oblique impact tests cause linear and rotational motion of the head.

1.6.3   Measurements

The impact mitigation capability of a helmet is determined according to the peak linear acceleration of the test headform during impact testing. To pass the standard test and achieve certification, a helmet must reduce the linear acceleration of the headform below a certain threshold. A uniaxial accelerometer is mounted at the centre of gravity of the test headform. To pass the impact attenuation test, the maximum linear acceleration of the test headform must not exceed 250 G. According to the Wayne State University tolerance curve, this corresponds to a 40% risk of skull fracture [85], and does not include the risk of any other head injury types. This testing standard does not consider the risk of sustaining TBI, which would require measurement of rotational head acceleration and velocity.

1.7   Honeycomb Structures

The limitations of EPS foam to absorb energy in oblique impacts suggest the need for an alternate energy-absorbing structure. Honeycomb, which is an array of adjoining cavities called cells, has many features that could make it suitable for this purpose and provide improved protection to the head during bicycle accidents. EPS foam is an isotropic material, whereas honeycomb is anisotropic – meaning its mechanical behaviours vary depending on loading direction and the strength is higher under out-of-plane compression compared to out-of-plane shear loading [61]. This suggests honeycomb could provide sufficient deformation under shear loading from the tangential component of an impact force to reduce the rotational motion of the head and provide protection against diffuse TBI.

Hexagonal honeycomb panels, which are made up of an array of identical six-sided cells (Figure 1.14), have been extensively used as the core in sandwich panels in applications such as vehicle crash test barriers, aeronautics, and space structures [88, 89].
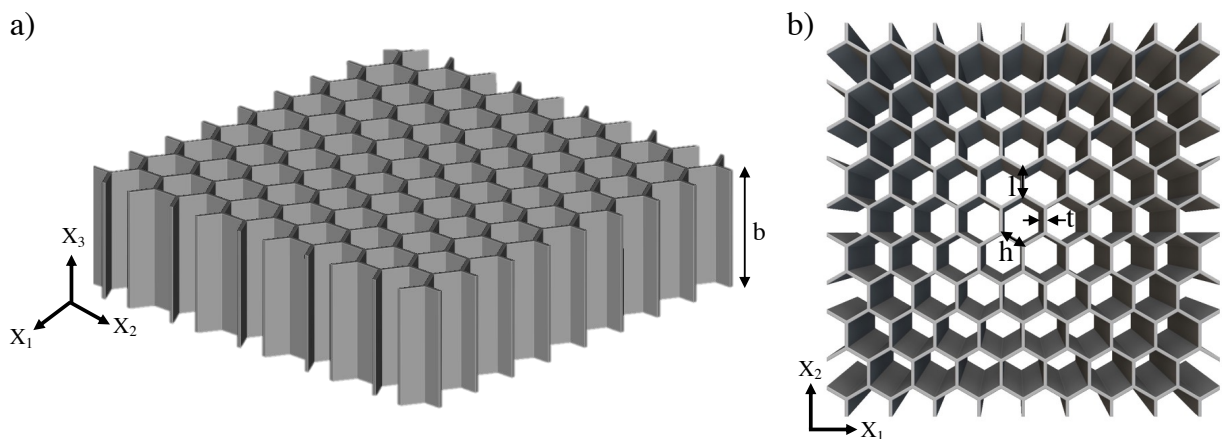
Figure 1.14: Hexagonal Honeycomb Structure
Honeycomb structures are made of columnar, hexagonal cells and defined by their cell size (given by *h* and *l*), cell wall thickness (*t*), and depth (*b*). a) Shows an isometric view, and b) shows a top view.

Hexagonal honeycomb has been shown to have superior compressive energy absorbing capabilities to many other honeycomb geometries [88]. However, pure hexagonal honeycomb panels cannot be wrapped into an elliptical dome shape like that of the human head. Beeswax honeycomb often has complex external geometry involving curvature and these natural structures frequently contain pentagons and heptagons within the array of hexagons (known as '5-7 defects') (Figure 1.15) [89].

Figure 1.15: Beeswax Honeycomb
Beeswax honeycomb contains pentagons (yellow) and heptagons (green) (5-7 defects) in areas with curvature (image adapted from [90]).

Inspiration can be taken from these natural structures to introduce strategic alterations in geometry that promote curvature in hexagonal honeycomb [88, 90, 91]. Specifically, 5-7 defects can be intentionally included in engineered honeycomb in two types of arrangements: clustered to form 'inclusions' and aligned to form 'boundaries'. These two 5-7 defect arrangement types have been shown to promote different collapse mechanisms in the neighboring cells and proximity of the 5-7 defects to each other has been shown to affect the strength of the structure, where a maximum strength improvement of 25-30% was achieved [92].

A hexagonal honeycomb structure is defined by its cell size given by 'h' and 'l', cell wall thickness given by 't', and depth given by 'b' (Figure 1.14). It is termed 'regular' hexagonal honeycomb when $h/l = 1$. The properties of a honeycomb structure depend on its relative density

$(\bar{\rho})$ – the amount of solid within the structure. For regular hexagonal honeycomb, relative density is given by Equation 1.1.

$$\bar{\rho} = \frac{\rho^*}{\rho_s} = \frac{2}{\sqrt{3}}\frac{t}{l}\left(1 - \frac{1}{2\sqrt{3}}\frac{t}{l}\right)$$
                                                                                       Equation 1.1

where ρ^* is the density of the honeycomb, ρ_s is the density of the solid it is made from, t is the honeycomb cell wall thickness, and l is the cell wall length [61].

1.7.1   Deformation Patterns

In-plane compression refers to loading in the plane of the hexagonal cells (X_1 and X_2 directions) (Figure 1.16a), out-of-plane compression refers to loading in line with the long axis of the cell walls (X_3 direction) (Figure 1.16b), and out-of-plane shear refers to loading in the X_1-X_3 and X_2-X_3 planes (Figure 1.16c) [61].
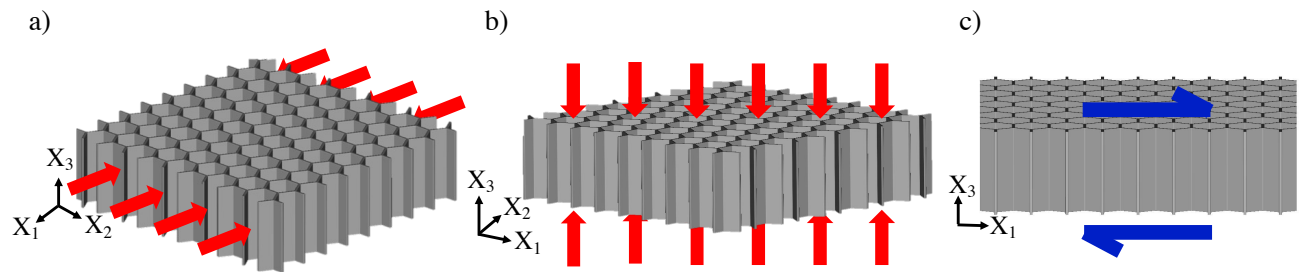
Figure 1.16: Loading Conditions on Honeycomb
a) Shows in-plane compression, b) shows out-of-plane compression, and c) shows out-of-plane shear.

When honeycomb structures undergo compression in either the in-plane or out-of-plane orientation, the deformation behaviour can be described in three regimes: linear elastic (where the slope defines the elastic modulus of the structure), stress plateau, and densification (Figure 1.17) [61].
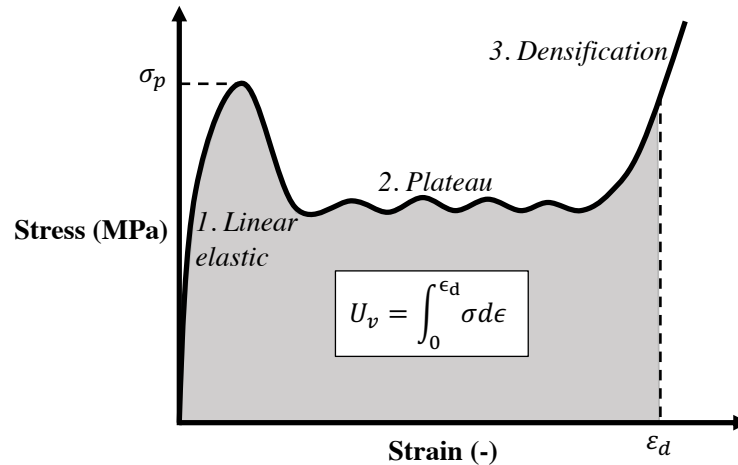
Figure 1.17: Honeycomb Stress-Strain Curve
The stress-strain relationship for honeycomb under in-plane or out-of-plane compressive loading is expected to have three regimes: linear-elastic, plateau, and densification.

For out-of-plane compression, in the linear-elastic regime the cell walls are axially compressed and in the stress plateau regime, the cell walls buckle [61]. For elastomeric honeycomb, this is observed as curves in the cell walls (Figure 1.18) [61].
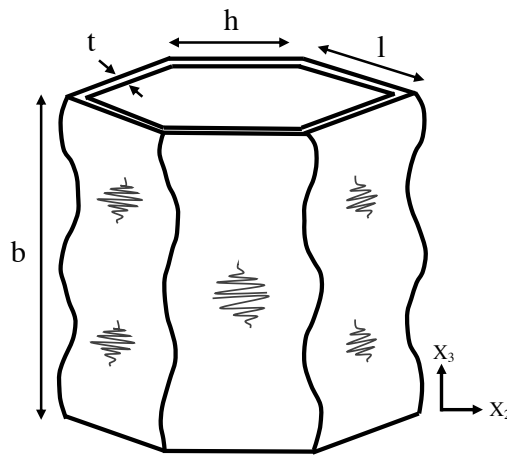
Figure 1.18: Elastomeric Honeycomb Under Out-of-Plane Compression
The typical behaviour of elastomeric honeycomb under compression the X_3 direction involves elastic buckling of the cell walls.

The densification regime begins when the cell walls touch (in-plane) or are fully compressed (out-of-plane), and the slope of the stress-strain curve tends toward the elastic modulus of the fully-dense solid from which the honeycomb structure was made [61]. The energy absorption capability of the honeycomb is the area under the stress-strain curve before densification, given by Equation 1.2.

$$U_v = \int_0^{\varepsilon_d} \sigma d\varepsilon \qquad\qquad \textbf{Equation 1.2}$$

where U_v is energy absorption per unit volume, σ is compressive stress, ε is compressive strain, and ε_d is densification strain [61].

The expected stress-strain relationship for plastic or brittle honeycombs under out-of-plane shear loading can be described similarly to compressive loading by three regimes: linear elastic, stress plateau, and densification [93]. The out-of-plane shear stress-strain relationship for elastomeric honeycomb is unclear; however, it is expected that the honeycomb would experience an initial linear elastic behaviour where the slope of the stress-strain curve represents the shear modulus, followed by cell wall buckling and bulging [93].

Deformation of an elastomeric honeycomb has the potential to be recoverable, meaning following the collapse of the structure it can return to its original shape [61]. This is extremely beneficial in applications where the structure could experience repeated impacts without requiring replacement. A challenge in using an elastomeric material is the reduced stiffness that could result in the structure reaching densification under excessive compressive loading [61].

1.8   Study Objectives

The goal of this study was to design a helmet made of honeycomb that improves upon the protective capabilities of EPS foam helmets and effectively reduces the risk of both skull fracture

and TBI. The design involves hexagonal honeycomb (where the cell walls are perpendicular to the surface of the human head) with 5-7 defects to accommodate the curvature of the human head, where the cell walls are made of thermoplastic polyurethane (TPU) (Figure 1.19).
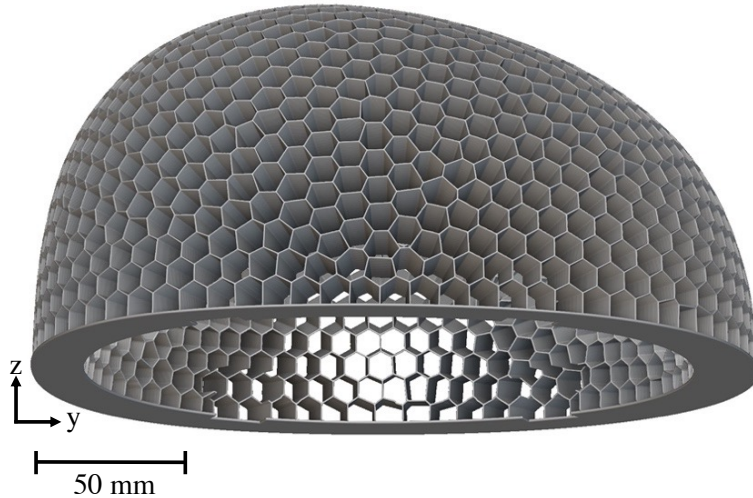
Figure 1.19: Honeycomb Helmet
The proposed bicycle helmet design involves hexagonal honeycomb with 5-7 defects.

The specific objectives of this study were:

1. To determine a TPU honeycomb design most suitable for dissipating energy in both compressive and shear loading for protection against skull fracture and TBI under quasi-static loading conditions;

2. To explore the effectiveness of the TPU honeycomb design in comparison to EPS foam, under dynamic combined (compression and shear) loading;

3. To determine a TPU honeycomb design most suitable for impact attenuation in both compressive and shear loading for protection against skull fracture and TBI under dynamic combined loading; and

4. To design and prototype a full-scale honeycomb helmet made of TPU.

The corresponding hypotheses were:

1. It is possible to achieve a honeycomb design made of TPU that effectively dissipates energy in both compressive and shear loading by varying the morphometry of the honeycomb structure, including relative density and 5-7 defect arrangement.

2. The proposed honeycomb helmet design made using TPU will perform better than EPS foam for impact attenuation under both compressive and shear loading, suitable for protection against skull fracture and TBI, while also being reusable for multiple impacts.

To address these objectives, Chapter 2 explored the quasi-static compressive and shear properties of flat honeycomb samples, which were 3D-printed for rapid prototyping. Two arrangements of 5-7 defects were tested, along with regular honeycomb with varying relative density.

In Chapter 3, dynamic drop tower impact tests were performed on the chosen honeycomb design in impact conditions more representative of real-world accidents to determine the effectiveness and reusability of the design.

In Chapter 4, the results of quasi-static and dynamic testing were used to determine the most suitable honeycomb design for dynamic impact conditions, the design was incorporated into the form of a full-scale helmet, and helmet prototypes were 3D-printed.

Chapter 2 – Quasi-Static Testing

Overview: This chapter outlines the objectives for the design of a honeycomb structure for head protection, where the injury mechanisms of skull fracture and traumatic brain injury were directly related to the mechanical properties of the honeycomb. A novel approach to honeycomb bicycle helmet design is introduced to accommodate curvature - the inclusion of 5-7 defects. Quasi-static compression and shear testing were performed on small, flat, 3D-printed honeycomb samples to explore the effects of including 5-7 defects and changing relative density. A honeycomb design most suitable for dissipating energy to protect against skull fracture and traumatic brain injury protection was determined according to these results.

2.1   Introduction

Head impacts in real-world bicycle accidents typically occur at an angle of 30° to 60° with respect to the horizontal impact surface [22, 23]. These 'oblique' impacts transmit both radial and tangential forces to the head, which cause linear and rotational head kinematics, respectively [13]. Research has shown that skull fracture and some severe brain injuries are caused by normal forces to the head, whereas the primary mechanism of diffuse brain injuries, such as diffuse axonal injury (DAI) or concussion, is rotational head kinematics (Section 1.3). Studies have also shown that wearing an expanded polystyrene (EPS) foam helmet does reduce the risk of skull fracture but does not effectively reduce the risk of sustaining most traumatic brain injuries (TBIs) (Section

1.3). The limitations of traditional helmets to protect the head during an oblique impact are attributed to the mechanical response of EPS foam, where EPS foam does not sufficiently deform under shear loading to address rotational accelerations [60]. As well, EPS foam absorbs impact energy through crack propagation, making it 'single-use'. An improved helmet design would absorb energy from the radial force component, dampen the tangential force component to mitigate rotational kinematics and provide protection for multiple impact events.

Hexagonal honeycomb, a structure found in nature [91, 96] could be a suitable alternative to EPS foam due to its energy-absorbing capabilities. In a honeycomb helmet design, the cell walls would be perpendicular to the surface of the human head and upon impact would primarily carry loads in the planes containing the axis of the hexagonal prisms. Specifically, the radial component of the impact force would induce out-of-plane compression to the honeycomb (Figure 2.1). This loading direction would cause radial stress and linear kinematics of the head and primarily pose a risk of skull fracture and some severe brain injuries. The tangential force component would induce out-of-plane shear loading on the honeycomb (Figure 2.1), which relates to rotational motion of the head, primarily posing a risk of diffuse TBI such as concussion and DAI. Honeycomb is hypothesized to be effective for head protection due to its anisotropy [61], where it is strong under out-of-plane compression to prevent densification during impact but weaker under out-of-plane shear loading to allow sufficient deformation to mitigate rotational kinematics.
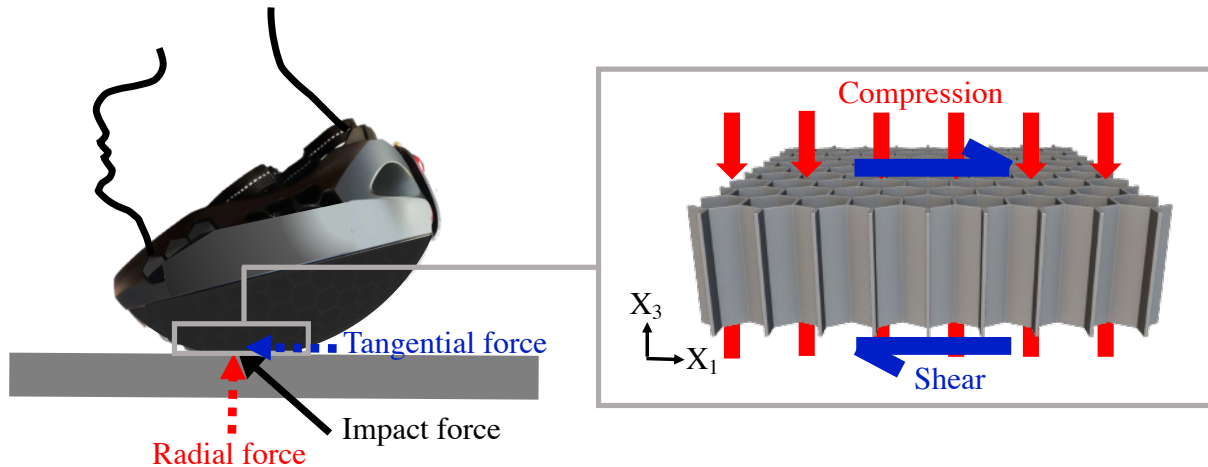
Figure 2.1: Forces in an Oblique Impact and Resulting Loading on Honeycomb
The radial component of the impact force would induce out-of-plane compression on the honeycomb (red), whereas the tangential force component would induce out-of-plane shear loading on the honeycomb (blue).

A challenge in using hexagonal honeycomb in the application of head protection is that it cannot conform to a surface with curvature without modification [61]. Beeswax contains curved honeycomb panels by using '5-7 defects', which are pentagon-heptagon pairs within the array of hexagons (Figure 1.15) [89][95]. These 5-7 defects can be intentionally included in engineered honeycomb in various arrangements for applications involving curvature.

3D-printing can be used to manufacture these complex geometries with a variety of solid materials. This manufacturing method is especially beneficial for rapid prototyping. Current helmets are 'single-use'; however, manufacturing honeycomb with an elastomeric solid such as thermoplastic polyurethane (TPU) means that following the deformation of the structure it could potentially restore its original shape and mechanical properties [61].

Therefore, the proposed helmet design is made of hexagonal honeycomb with 5-7 defects to accommodate the curvature of the human head and 3D-printed with TPU (Figure 1.19). When studying the effectiveness of honeycomb in helmets, out-of-plane compressive and shear

properties must be considered. The deformation behaviour of honeycomb under out-of-plane compressive loading can be described in three regimes: linear-elastic, stress plateau, and densification (Figure 1.20) [61]. The out-of-plane shear stress-strain relationship for elastomeric honeycomb is unclear, however, it is expected that there would be an initial linear-elastic behaviour where the slope of the stress-strain curve represents the shear modulus (G) [93]. The properties of honeycomb primarily depend on relative density ($\bar{\rho}$) [61], and therefore it is hypothesized that this geometric parameter can be altered to determine a design that is most suitable for both skull fracture and TBI protection.

The purpose of this study was to determine a honeycomb design most suitable for head protection. Therefore, the out-of-plane compressive and shear properties (Figure 1.19b-c) of honeycomb and EPS foam were explored using flat samples. The recoverability of the honeycomb helmet design was also explored to determine its potential to protect against repeated impacts without requiring replacement.

2.2 Methods

2.2.1 Design Objectives

To determine a honeycomb design that would be most suitable for providing effective protection in bicycle accidents, three design requirements were determined and are outlined below.

i. Under out-of-plane compression, the honeycomb must absorb the kinetic energy of the head at impact through the potential energy of deformation (strain energy). Energy absorption per unit volume (U_v) is given by the area under the stress-strain curve before densification (Figure 1.20 and Equation 1.2). If the kinetic energy exceeded the energy absorption capacity of the

honeycomb, the structure would 'bottom out', meaning densification would be reached during the impact. The spike in stress that occurs during densification would then be transmitted to the human head and pose a direct risk of injury as it is likely this stress would exceed the strength of the human skull. EPS foam helmets have been shown to be effective in preventing skull fracture and associated injuries (Section 1.3). Therefore, it is inferred that EPS foam provides sufficient energy absorption capability in real-world head impacts and it can be used as a benchmark for new helmet designs.

ii. The normal stress experienced by the head, or the peak compressive stress of the honeycomb (σ_p) must not exceed a specified limit corresponding to the injury threshold for skull fracture (σ_c). A force threshold of 5.05 kN was used here, which corresponds to a 50% risk of skull fracture [96]. The stress threshold for skull fracture (σ_c) was calculated to be 1.46 MPa by dividing the force threshold by the area of the impactor used in the study where the threshold was identified (3,800 mm^2).

iii. The shear modulus (G) of the honeycomb should be minimized to minimize rotational head acceleration (this derivation is given in Appendix B). Shear modulus (G) is given by the slope of the linear-elastic regime of the stress-strain curve.

Volumetric energy absorption (U_v), compressive peak stress (σ_p), and shear modulus (G) are highly influenced by the relative density ($\bar{\rho}$) of the honeycomb [61]. The effects of relative density ($\bar{\rho}$) on these mechanical properties were determined through experimental testing and a relative density ($\bar{\rho}$) value that meets the above objectives was chosen.

2.2.2   Honeycomb Samples

Various honeycomb designs were generated using a parametric CAD software (nTopology, New York, USA). 3D-printing was employed for rapid prototyping of all samples (Appendix C) with TPU filament, Ninjatek Cheetah (Ninjatek, Manheim, Pennsylvania USA), an elastomeric material, which has a density of 1.22 g/cm^3, a tensile strength of 39 MPa, a hardness of 95 Shore A, and an elongation at break of 580%. The area of the samples (in the plane of the honeycomb cells) was 8840 mm^2 to reflect the average contact area in a helmeted bicycle accident [97]. Honeycomb samples with a range of relative densities ($\bar{\rho}$) were generated and 3D-printed to determine its effect on out-of-plane compressive and shear properties (objectives i., ii., and iii.). EPS foam samples with a density of 85 kg/m^3 were obtained (Seven Star Sports, Hamilton, Ontario, Canada) to determine its mechanical response under out-of-plane compressive (objective ii.). To determine the effect of 5-7 defects on out-of-plane compressive properties, regular honeycomb, honeycomb with 'stacked' 5-7 defects, and honeycomb with 'staggered' 5-7 defects were 3D-printed at a constant relative density ($\bar{\rho}$) (Figure 2.2). These two 5-7 defect designs were chosen as potential methods for allowing the honeycomb to conform to the curvature of the human head. Regular honeycomb samples with constant relative density ($\bar{\rho}$) were 3D-printed to determine the effect of strain rate ($\dot{\varepsilon}$) on compressive properties. A digital caliper with an accuracy of $\pm\, 0.02$ mm was used to measure the dimensions of the honeycomb and EPS foam samples. A scale with an accuracy of 0.5 g was used to measure the mass of each sample for determining relative density ($\bar{\rho}$).
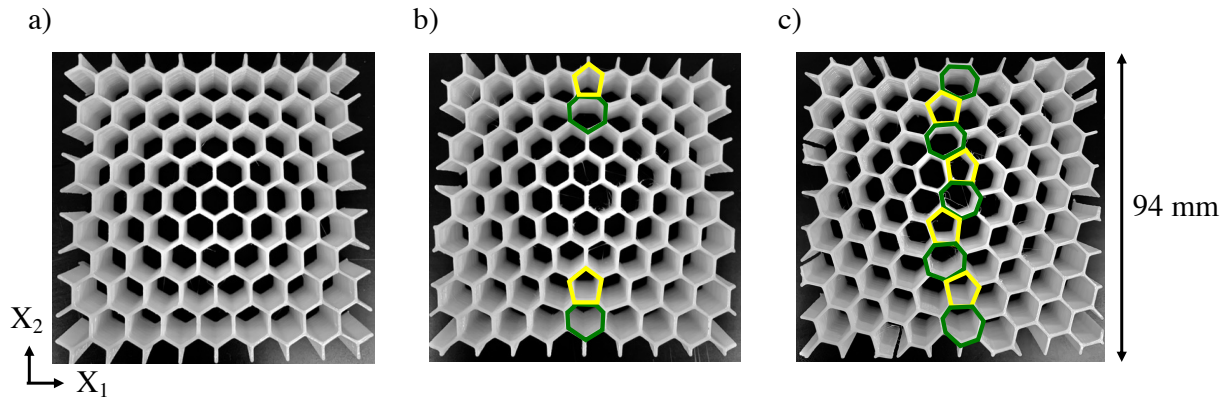
Figure 2.2: 3D-Printed Honeycomb Samples for Compression Tests
Three honeycomb designs were 3D-printed for out-of-plane compression testing including a) regular honeycomb, b) honeycomb with 'stacked' 5-7 defects, and c) honeycomb with 'staggered' 5-7 defects. The pentagons are outlined in yellow, and the heptagons are outlined in green.

2.2.3   Compression Testing

For use in out-of-plane compression tests, honeycomb and EPS foam samples were 94 by 94 by 25 mm. The thickness of the samples (25 mm) was chosen for consistency with typical EPS foam bicycle helmets. Six regular honeycomb designs were 3D-printed with a target relative density ($\bar{\rho}$) range of 15% to 25% to determine the effect on out-of-plane compressive properties (objectives i. and ii.) (sample size (N) = 1-4 (Table 2.1)). Honeycomb with 'stacked' 5-7 defects (Figure 2.2b) (N = 3) and 'staggered' 5-7 defects (Figure 2.2c) (N = 3) were 3D-printed at a constant target relative density ($\bar{\rho}$) of 17% and compared to regular honeycomb with a target relative density ($\bar{\rho}$) of 17% (N = 4). Regular honeycomb (Figure 2.2a) was 3D-printed at a constant target relative density ($\bar{\rho}$) of 16% to explore the effect of strain rate ($\dot{\varepsilon}$) (N = 2 for $\dot{\varepsilon}$ of 3×10^{-2} /s and 6×10^{-2} /s, and N = 4 for $\dot{\varepsilon}$ of 10^{-3} /s). The number of samples per group varied due to inaccuracy between the CAD models and the 3D-printed samples.

Out-of-plane compression tests (Figure 1.19b) were performed using a 30 kN Instron materials testing machine (model 5967, Illinois Tool Works, Norwood, Massachusetts, USA) (Figure 2.3). Circular steel platens, 150 mm in diameter, were mounted to the stationary base and the crosshead, in alignment with the central axis of the machine. Coconut oil was applied to both platens as a lubricant to reduce the effect of friction on the compressive response. The samples were then centred on the stationary platen. To determine the effects of honeycomb relative density ($\bar{\rho}$) and 5-7 defects, and for EPS foam tests, the deformation rate was 2.5×10^{-5} m/s, corresponding to a quasi-static strain rate ($\dot{\varepsilon}$) of 10^{-3} /s. To explore the strain rate dependence of honeycomb, tests were also performed at strain rates ($\dot{\varepsilon}$) of 3×10^{-2} /s and 6×10^{-2} /s. The samples were compressed until after the onset of densification, where the slope of the stress-strain curve approached the elastic modulus of the solid material (Figure 1.20). A preload of 2N was applied before data collection. A Pixelink D755CU-AF16 (Ametek, Berwyn, Pennsylvania, USA) camera was used to capture deformation shapes during the tests, where images were captured in one-second increments.
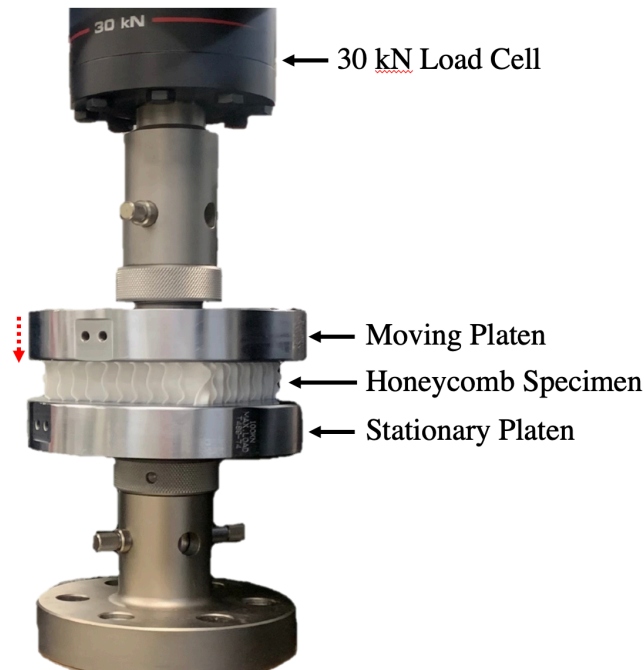
Figure 2.3: Compression Testing Setup
An Intron materials testing machine with a 30 kN load cell was used for out-of-plane
compression testing on honeycomb and EPS foam samples.

From these tests, the following were determined:

- The effects of relative density ($\bar{\rho}$) on volumetric energy absorption (U_v) and peak

  compressive stress (σ_p) (objectives i. and ii.);

- Volumetric energy absorption (U_v) and compressive peak stress (σ_p) for EPS foam

  (objective i.);

- The effects of 5-7 defect arrangement on volumetric energy absorption (U_v) and

  compressive peak stress (σ_p); and

- The effects of strain rate ($\dot{\varepsilon}$) on volumetric energy absorption (U_v) and compressive

  peak stress (σ_p).

Two compression cycles were performed on honeycomb and EPS foam samples at a strain rate ($\dot{\varepsilon}$) of 10^{-3} /s to explore their potential for reusability.

2.2.4   Shear Testing

For out-of-plane shear testing, honeycomb samples were 12.0 by 7.4 by 1.0 cm. The area was chosen to be consistent with compression test samples. The thickness of the samples (1 cm) was chosen according to ASTM standards for determining shear properties of sandwich core materials (ASTM C 273/C 273M – 07a) [98], which indicates that the width and length should be at least 3 and 10 times the thickness of the sample, respectively, to minimize the amount of normal loading. Four regular honeycomb designs were 3D-printed with a target relative density ($\bar{\rho}$) range of 15% to 25% (N = 2-3 (Table 2.2)) to determine the effect on out-of-plane shear properties (objective iii.). Facesheets with a 1 mm thickness that extended 0.5 mm on each side were 3D-printed onto the honeycomb structures with the same TPU material to increase the surface area for adhesion to the testing apparatus (Figure 2.4).

a)   b)
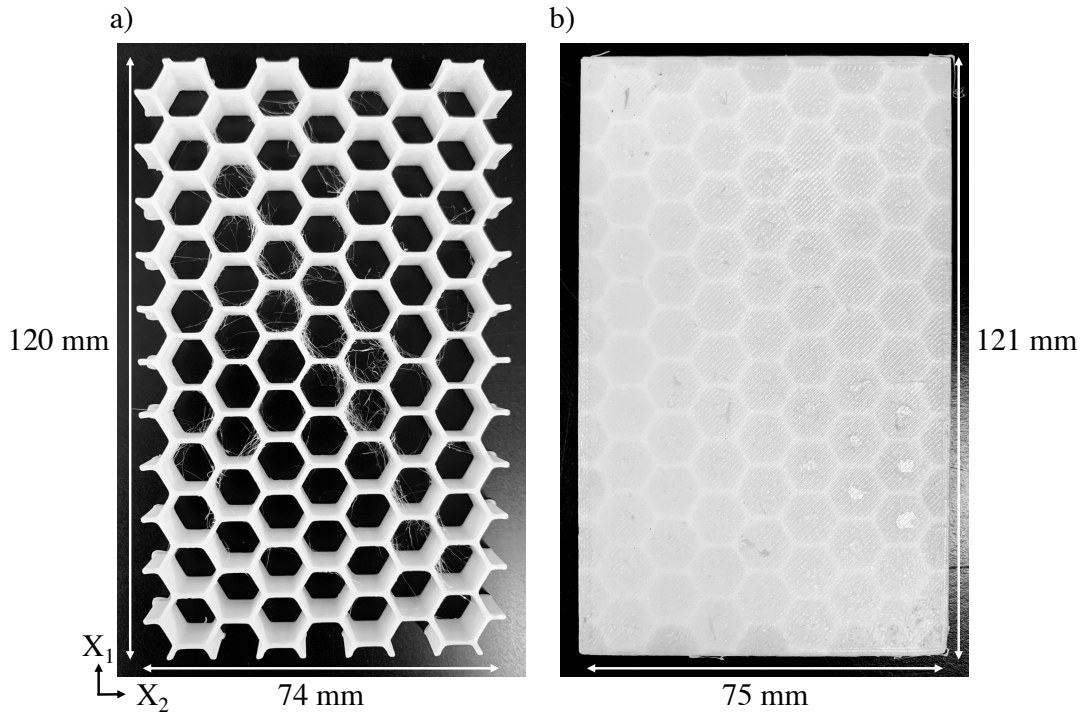
Figure 2.4: 3D-Printed Honeycomb Samples for Shear Testing
Honeycomb samples for out-of-plane shear testing were 3D-printed. a) Shows regular honeycomb without facesheets, and b) shows regular honeycomb with 1 mm-thick facesheets that extend 0.5 mm on each side.

Out-of-plane shear tests (Figure 1.19c) were performed using the same Instron materials testing machine described previously with a custom plate shear test configuration (Figure 2.5) (Appendix D) recommended by the ASTM standard (ASTM C 273/C 273M – 07a) [98]. The custom test apparatus consisted of a lower fitting, hinge, and loading plate connected to the stationary base of the machine; and an upper fitting, hinge, and loading plate connected to the moving crosshead. The two hinge joints allowed the loading plates to be positioned according to the thickness of the honeycomb sample. A tensile load was applied through the central axis of the test machine, connected to the upper edge of one loading plate and lower edge of the other loading

plate. Although this method did not produce pure shear loading, the normal component was assumed to be negligible due to the length-to-thickness ratio of the samples.
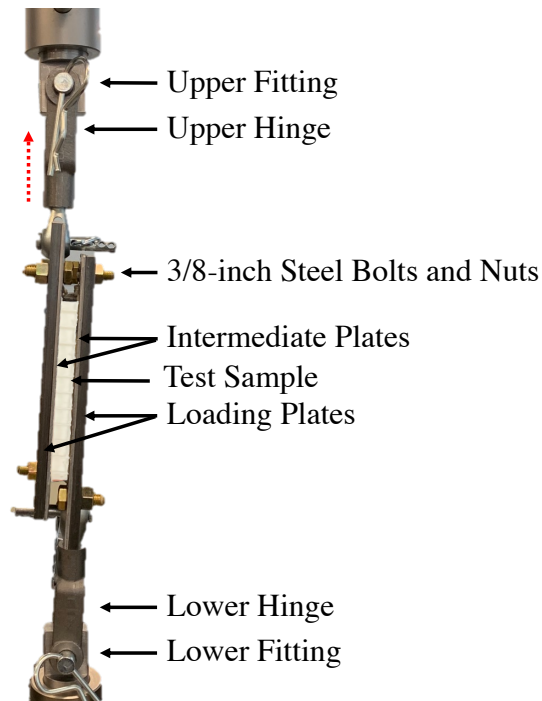
Figure 2.5: Shear Testing Setup
A custom test setup was developed for out-of-plane shear testing, where the lower fitting was connected to the stationary base of the Instron machine, and the upper fitting was connected to the moving crosshead that supports a 30kN load cell.

To facilitate testing of multiple samples without damaging the loading plates, the honeycomb samples were glued to 1/8-inch steel intermediate plates (Figure 2.5) using Loctite 414 cyanoacrylate (Henkel, Düsseldorf, Germany), which has a shear strength of 18-26 N/mm^2. The plates were sandblasted and cleaned, then a thin layer of glue was applied to one honeycomb facesheet and one intermediate steel plate. The honeycomb sample was aligned in the centre of the plate and pressure was applied for 30 seconds. This was left to dry for 30 minutes before performing the same procedure for the other facesheet and intermediate plate. The samples were left to cure for 24 hours to allow the glue to fully cure, as per package instructions.

The sample-intermediate plate configuration was mounted to 3/8-inch steel loading plates using 3/8-inch steel bolts and nuts. The dimensions of the loading plates were 190 by 89 mm to extend past the edges of the honeycomb samples. Load and displacement were zeroed on the Instron, then the shear apparatus with the honeycomb sample was mounted. A preload of 100 N was applied prior to data collection. The upper loading plate moved at a deformation rate of 4.2×10^{-5} m/s, which corresponded to a quasi-static strain rate ($\dot{\delta}$) of 4.2×10^{-3} /s. The samples were sheared until total failure of either the sample itself or of the adhesive at the interface of a facesheet and intermediate steel plate. From these tests, the effect of relative density ($\bar{\rho}$) on shear modulus (G) was determined (objective iii.).

2.2.5   Data Analysis

All data analysis was performed in MATLAB (MathWorks, Natick, Massachusetts, USA) (Appendix E). Experimental relative density ($\bar{\rho}$) was determined by dividing the mass of each sample by the mass of a solid with equal external dimensions. Load-displacement data from the Instron were converted to stress-strain data based on the initial sample dimensions.

For compressive stress-strain results, the maximum slope in the linear-elastic region was determined and data points before this point were removed and replaced with a line of maximum slope. Then the stress-strain data was shifted to the origin. Densification strain (ε_d) was defined as the strain at which the slope of the tangent became equal to or greater than the slope of the elastic regime [99] (Figure 1.20). Volumetric energy absorption (U_v) was determined by computing the approximate integral of stress with respect to strain, before densification strain (ε_d), using the trapezoidal method. Compressive peak stress (σ_p) was determined by finding the maximum value of stress between the first data point and the plateau region. Mean and standard deviation of peak

stress (σ_p) and volumetric energy absorption (U_v) were found for each group. From this, the effect of relative density ($\bar{\rho}$) on volumetric energy absorption (U_v) and peak stress (σ_p) were determined by fitting regression curves to the data (objectives i. and ii.). One-way ANOVAs with post hoc Tukey tests were used to detect significant differences in volumetric energy absorption (U_v) and peak stress (σ_p) among regular honeycomb and honeycomb with 5-7 defects; and among honeycomb at different loading rates, with a level of significance (α) of 0.05.

For compression tests on the EPS foam samples, the same analysis was performed; however, a different method was used to calculate densification strain (ε_d) since the slope of the linear-elastic regime was not reached again in the densification regime. Instead, densification strain (ε_d) was defined as the global maximum of energy absorption efficiency (η) (Equation 2.1) [63].

$$\eta(\varepsilon_R) = \frac{\int_{\varepsilon_0}^{\varepsilon_R} \sigma(\varepsilon)d\varepsilon}{\sigma_c(\varepsilon_R)} \qquad \textbf{Equation 2.1}$$

where $\sigma(\varepsilon)$ is the stress at a strain of ε, ε_0 is the strain of the initial point, ε_R is the strain at a particular point along the curve, and $\sigma_c(\varepsilon_R)$ is the stress value corresponding to ε_R. Then mean and standard deviation of peak stress (σ_p) and volumetric energy absorption (U_v) were determined.

For shear tests on honeycomb samples, data noise due to movement of the test apparatus was removed. A power regression line was fit to the corrected data up until a critical point where the relationship became non-linear, and the slope of this line was taken as shear modulus (G). Mean and standard deviation of shear modulus (G) were found for each design. From this, the effect of relative density ($\bar{\rho}$) on shear modulus (G) was determined by regression analysis (objective iii.).

A minimum relative density requirement ($\bar{\rho}_{lower}$) was determined by evaluating the regression equation for honeycomb volumetric energy absorption (U_v) versus relative density ($\bar{\rho}$) at the value of volumetric energy absorption (U_v) found for EPS foam (objective i.). A maximum allowable relative density ($\bar{\rho}_{upper}$) was determined by evaluating the regression equation for honeycomb compressive peak stress (σ_p) versus relative density ($\bar{\rho}$) at the stress threshold for skull fracture (σ_c) (objective ii.). The most suitable relative density ($\bar{\rho}$) for head protection was determined by finding the relative density ($\bar{\rho}$) that would minimize shear modulus (G) in between the lower and upper relative density limits according to the regression relationship for honeycomb shear modulus (G) versus relative density ($\bar{\rho}$) (objective iii.)

2.3   Results

2.3.1   Compression Testing

The stress-strain relationships for all honeycomb samples could be described in three regimes: linear-elastic, where the cell walls exhibited axial compression (Figure 2.6a); stress plateau, where the cell walls exhibited buckling (Figure 2.6b); and densification (Figure 2.6c).

a)   b)   c)
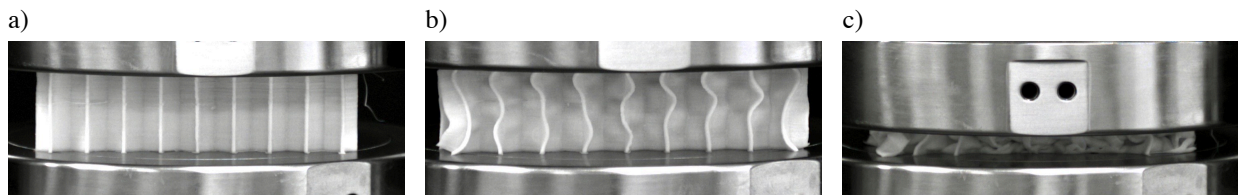
Figure 2.6: Deformation Patterns of Honeycomb Under Compression
a) Shows axial compression of the cell walls, b) shows buckling of the cell walls, and c) shows densification.

To determine the effect of relative density ($\bar{\rho}$) on out-of-plane compressive properties, six regular honeycomb designs were 3D-printed with relative density ($\bar{\rho}$) ranging from 14% to 28% and average out-of-plane compressive stress-strain responses were obtained (Figure 2.7).
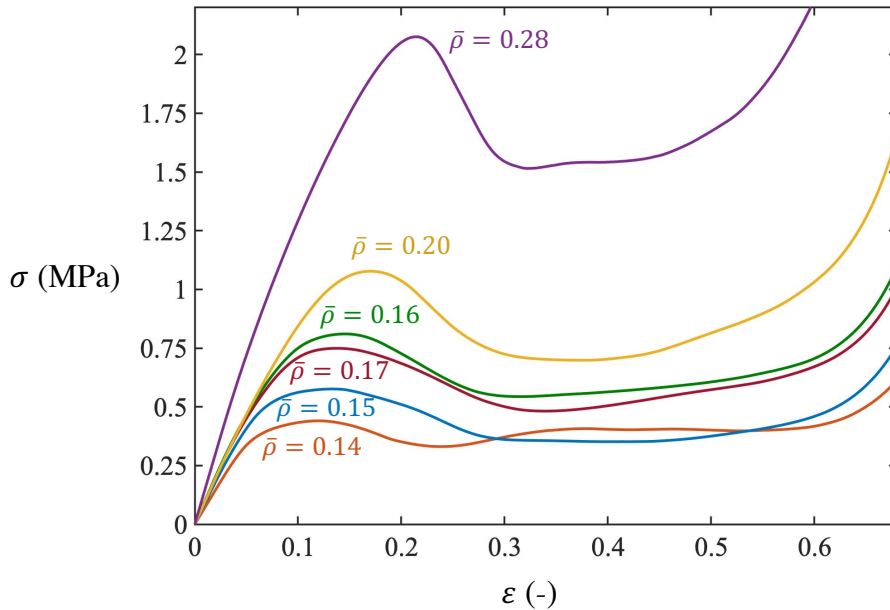
Figure 2.7: Compression Test Results for Regular Honeycomb with Varying $\bar{\rho}$
Average stress-strain curves for out-of-plane compression tests are shown for regular honeycomb with six different $\bar{\rho}$ ranging from 14% to 28%.

Peak stress (σ_p) increased with relative density ($\bar{\rho}$) (Table 2.1), and this effect was represented by a power regression with a coefficient of determination (R^2) of 0.98 (Figure 2.8). According to the regression equation for peak stress (σ_p), where the stress threshold for skull fracture (σ_c) was 1.46 MPa [96], the upper bound on relative density ($\bar{\rho}_{upper}$) was determined to be 22.6%.

Table 2.1: σ_p and U_v Results for Regular Honeycomb with Varying $\bar{\rho}$

Average σ_p and U_v results are given for out-of-plane compression tests on regular honeycomb with six different $\bar{\rho}$ ranging from 14% to 28%. N is the number of samples.

Average $\bar{\rho}$ (%)	N	Average σ_p (MPa)	Average U_v (kJ/mm³)
13.6	1	0.44	0.28
14.8 ± 0.2	3	0.58 ± 0.04	0.30 ± 0.01
16.3 ± 0.1	4	0.75 ± 0.03	0.41 ± 0.01
16.9 ± 0.2	3	0.87 ± 0.06	0.43 ± 0.02
19.8 ± 0.9	3	1.08 ± 0.08	0.55 ± 0.07
27.9	1	2.08	1.05
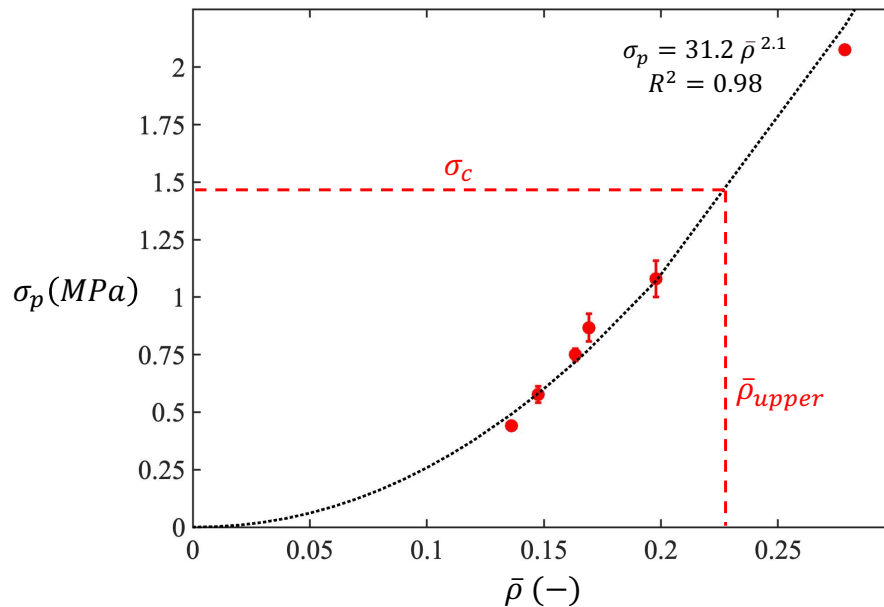
Figure 2.8: σ_p with Respect to $\bar{\rho}$, Fit with a Power Regression

The relationship between σ_p and $\bar{\rho}$ is shown, where the data points represent the average σ_p for each $\bar{\rho}$ with standard deviation error bars. The data were fit with a power regression curve. The red dashed lines represent the skull fracture threshold (σ_c) and the corresponding upper relative density limit ($\bar{\rho}_{upper}$).

Volumetric energy absorption (U_v) also increased with relative density ($\bar{\rho}$) and this effect was represented by a power regression (Figure 2.9), where the coefficient depends on the geometry

of the cellular structure and the exponent depends on the deformation mechanism [92]. The coefficient of determination (R^2) was 0.99.
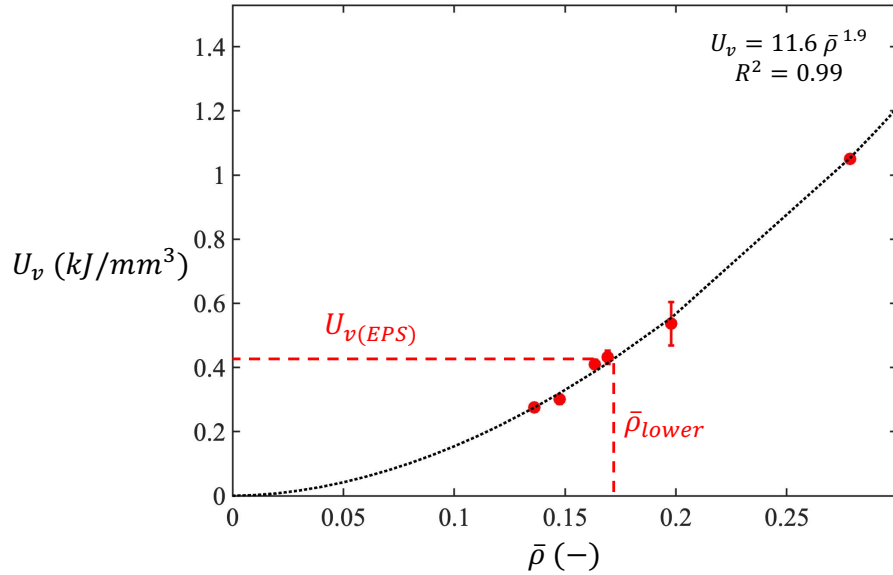
Figure 2.9: U_v with Respect to $\bar{\rho}$, Fit with a Power Regression
The relationship between U_v and $\bar{\rho}$ is shown, where the data points represent the average U_v for each $\bar{\rho}$ with standard deviation error bars. The data were fit with a power regression curve. The red dashed lines represent U_v for EPS foam and the corresponding lower relative density limit ($\bar{\rho}_{lower}$).

To obtain a benchmark for the bicycle helmet design, stress-strain results were obtained for EPS foam under out-of-plane compressive loading (Figure 2.10). The average peak stress (σ_p) was 1.02 ± 0.05 MPa and the average volumetric energy absorption (U_v) was 0.44 ± 0.01 kJ/mm³. Assuming the honeycomb must have at least the energy absorption capacity of EPS foam of 0.435 ± 0.011 kJ/mm³, a lower bound on relative density ($\bar{\rho}_{lower}$) of 17% was predicted by the power regression for honeycomb volumetric energy absorption (U_v) (Figure 2.9).
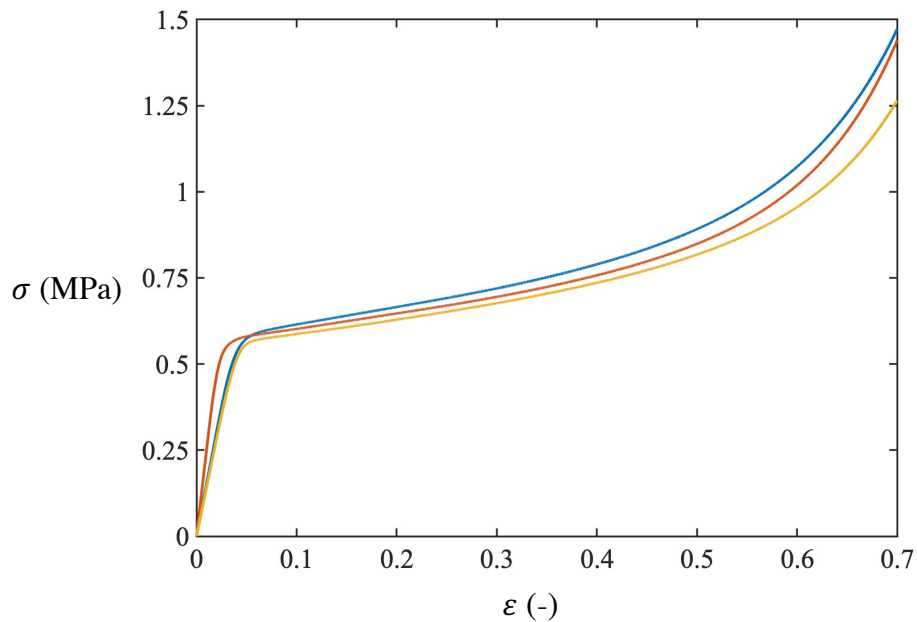
Figure 2.10: Compression Test Results for EPS Foam
Stress-strain curves are shown for out-of-plane compression tests on three EPS foam samples.

To determine the effect of 5-7 defects on out-of-plane compressive properties, three designs were 3D printed with an average relative density ($\bar{\rho}$) of $17.0 \pm 0.25\%$: regular honeycomb, honeycomb with stacked 5-7 defects, and honeycomb with staggered 5-7 defects. There were no statistical differences in relative density ($\bar{\rho}$) between designs. The three designs exhibited similar average stress-strain curve shapes (Figure 2.11). Peak stress (σ_p) was 12% lower for honeycomb with stacked 5-7 defects ($p = 0.20$) and 16% lower for honeycomb with staggered 5-7 defects ($p = 0.08$) compared to regular honeycomb; however, these differences were not statistically significant (Figure **2.12**a). Volumetric energy absorption (U_v) was 13% ($p = 0.28$) and 16% ($p = 0.17$) lower for stacked and staggered 5-7 defect designs, respectively, compared to regular honeycomb; however, these differences were not statistically significant (Figure **2.12**b).
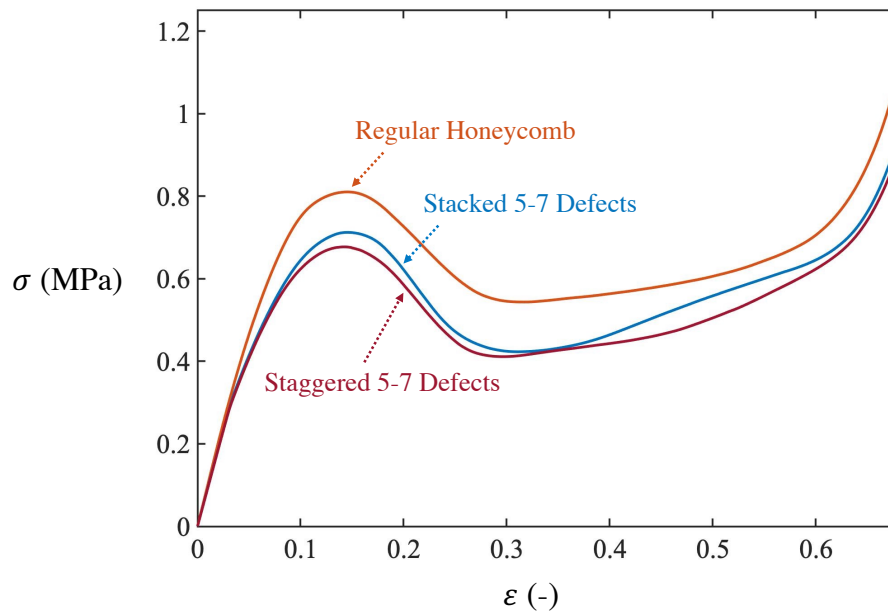
Figure 2.11: Compression Test Results for Honeycomb with and without 5-7 Defects
Average stress-strain curves are shown for out-of-plane compression tests on regular honeycomb, honeycomb with stacked 5-7 defects and honeycomb with staggered 5-7 defects.
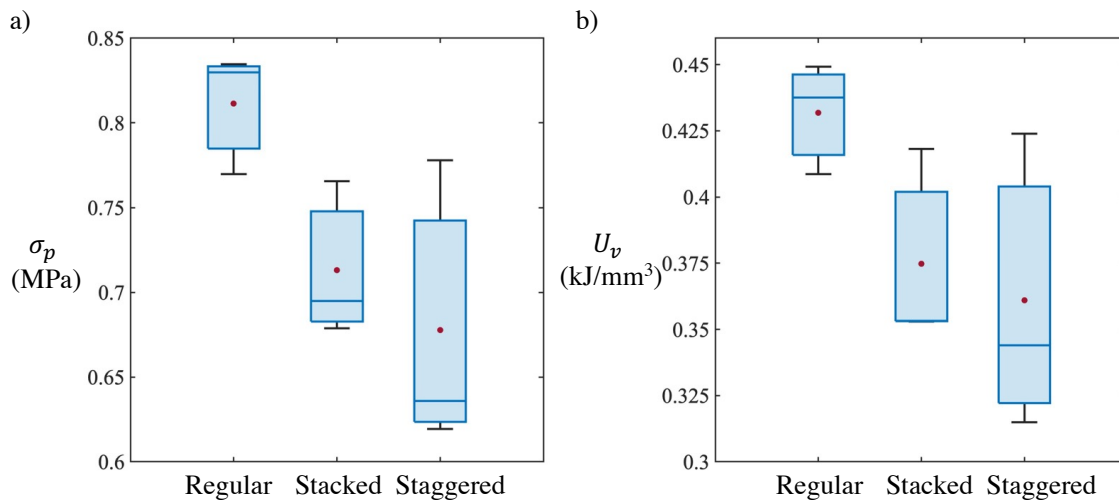
Figure 2.12: σ_p and U_v Results for Honeycomb with and without 5-7 Defects
Average σ_p and U_v results are shown for out-of-plane compression tests on regular honeycomb, honeycomb with stacked 5-7 defects and honeycomb with staggered 5-7 defects. The median is given by the line inside each box, the edges of the box are the lower and upper quartiles, the whiskers represent the lowest and highest values, and the red dot is the mean.

To determine the effect of strain rate ($\dot{\varepsilon}$) on out-of-plane compressive properties, regular honeycomb samples were 3D-printed with an average relative density ($\bar{\rho}$) of 16.3 ± 0.2%. There were no significant differences in relative density ($\bar{\rho}$) between groups. The stress-strain curve shapes were similar among the three loading conditions (examples are given in Figure 2.13). Peak stress (σ_p) increased significantly from the 0.001 /s condition by 17% (p = 0.006) and 23% (p = 0.002) for the 0.03 /s and 0.06 /s conditions, respectively (Figure 2.14a). Volumetric energy absorption (U_v) increased by 9% from the 0.001 /s condition to the 0.03 /s condition, but this difference was not statistically significant (p = 0.11) (Figure 2.14b). Volumetric energy absorption (U_v) increased significantly from the 0.001 /s condition to the 0.06 /s condition by 22% (p = 0.003) (Figure 2.14b).
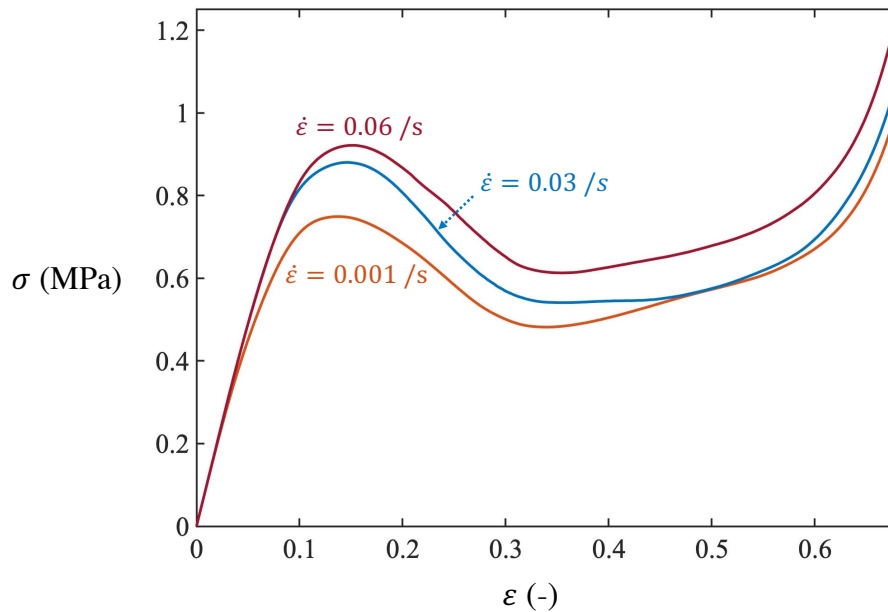
Figure 2.13: Compression Test Results for Honeycomb Under Different Loading Rates
Average stress-strain curves are shown for out-of-plane compression tests on regular honeycomb with three different $\dot{\varepsilon}$, including 0.001 /s, 0.03 /s, and 0.06 /s.
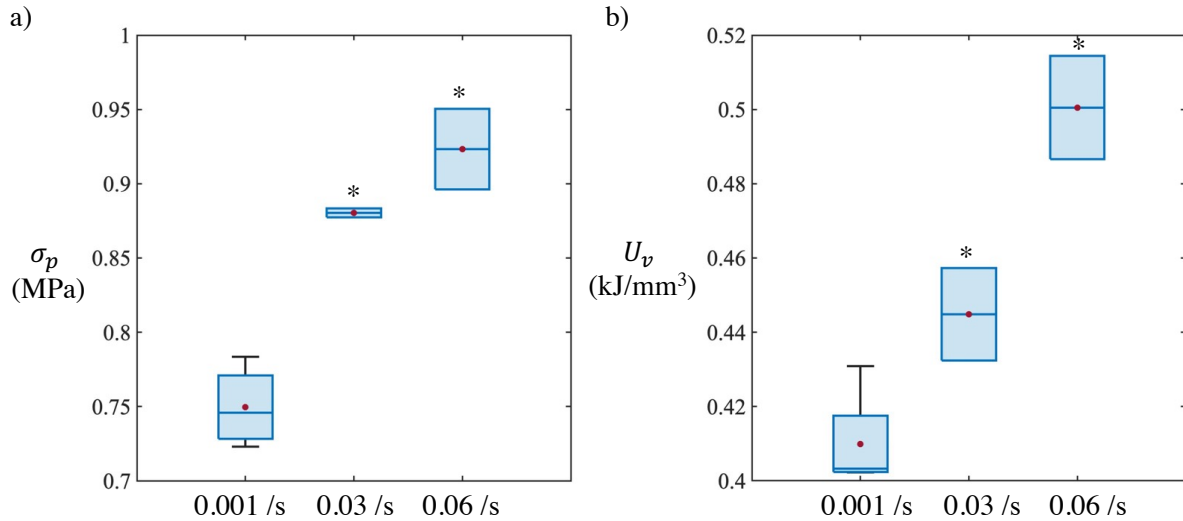
Figure 2.14: σ_p and U_v Results for Honeycomb Under Varying $\dot{\varepsilon}$
Average σ_p and U_v results are shown for out-of-plane compression tests on regular honeycomb with three different $\dot{\varepsilon}$, including 0.001 /s, 0.03 /s, and 0.06 /s. The median is given by the line inside each box, the edges of the box are the lower and upper quartiles, the whiskers represent the lowest and highest values, and the red dot is the mean. An asterisk (*) shows a significant difference from the 0.001 /s loading condition (p < 0.05).

In testing the effect of multiple out-of-plane compression cycles on the properties of honeycomb, the stress-strain curves exhibited similar shapes (an example is given in Figure 2.15). However, peak stress (σ_p) and volumetric energy absorption (U_v) decreased significantly by 51% and 49%, respectively. As well, residual cell wall bending was observed after the first compression (Figure 2.16).
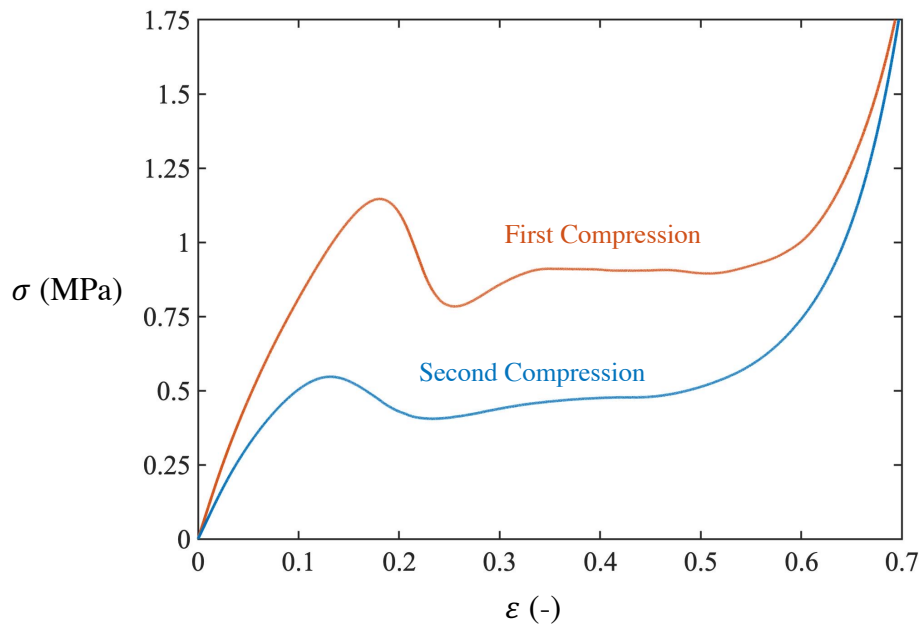
Figure 2.15: Results for Repeated Compression Tests on Honeycomb
Stress-strain curves are shown for regular honeycomb under two rounds of out-of-plane compressive loading to test the reusability of the design, where there was a decrease in σ_p and U_v.
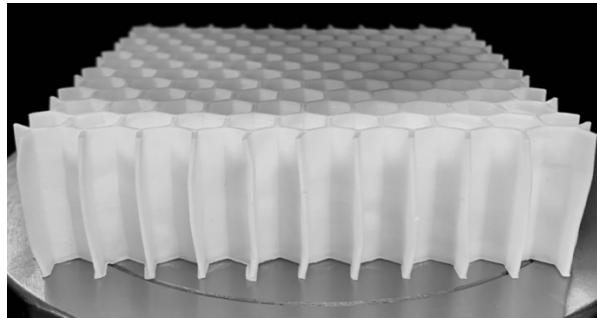
Figure 2.16: Honeycomb Sample After First Compression Test
Permanent cell wall bending was observed in honeycomb samples after the first compression test.

In testing the effect of multiple out-of-plane compression cycles on the properties of EPS foam, volumetric energy absorption (U_v) decreased by 99.9% from the first to the second compression (an example is given in Figure 2.17).
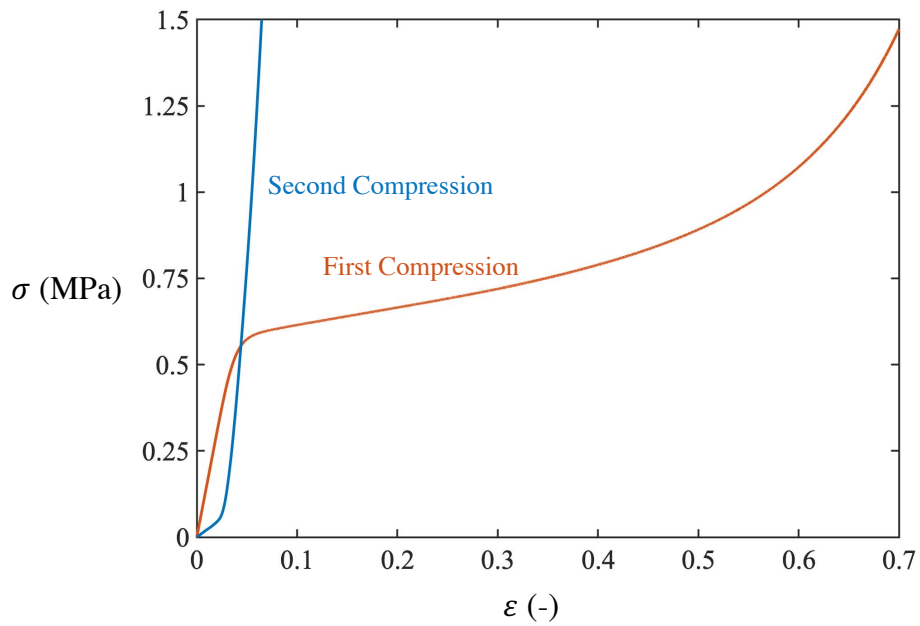
Figure 2.17: Results for Repeated Compression Tests on EPS
Stress-strain curves are shown for EPS foam under two rounds of out-of-plane compressive loading.

2.3.2   Shear Testing

Shear deformation of the honeycomb samples was seen as cell wall tilting in the linear-elastic region (Figure 2.18a), followed by cell wall buckling and bulging (Figure 2.18b).

a)   b)

Figure 2.18: Deformation Patterns of Honeycomb Under Shear Loading
a) Deformation in the linear-elastic region was followed by b) cell wall buckling and bulging.

To determine the effect of relative density ($\bar{\rho}$) on out-of-plane shear properties, four regular honeycomb designs were 3D-printed with relative density ($\bar{\rho}$) ranging from 15% to 27% and average stress-strain responses were obtained (Figure 2.19a), where the portion of the curve prior to yielding is the area of interest (Figure 2.19b). It is important to note that delamination occurred due to adhesive failure prior to honeycomb failure for some samples, and in these cases, the maximum stress on the stress-strain curve is not representative of the shear strength of the structure.

a)

b)
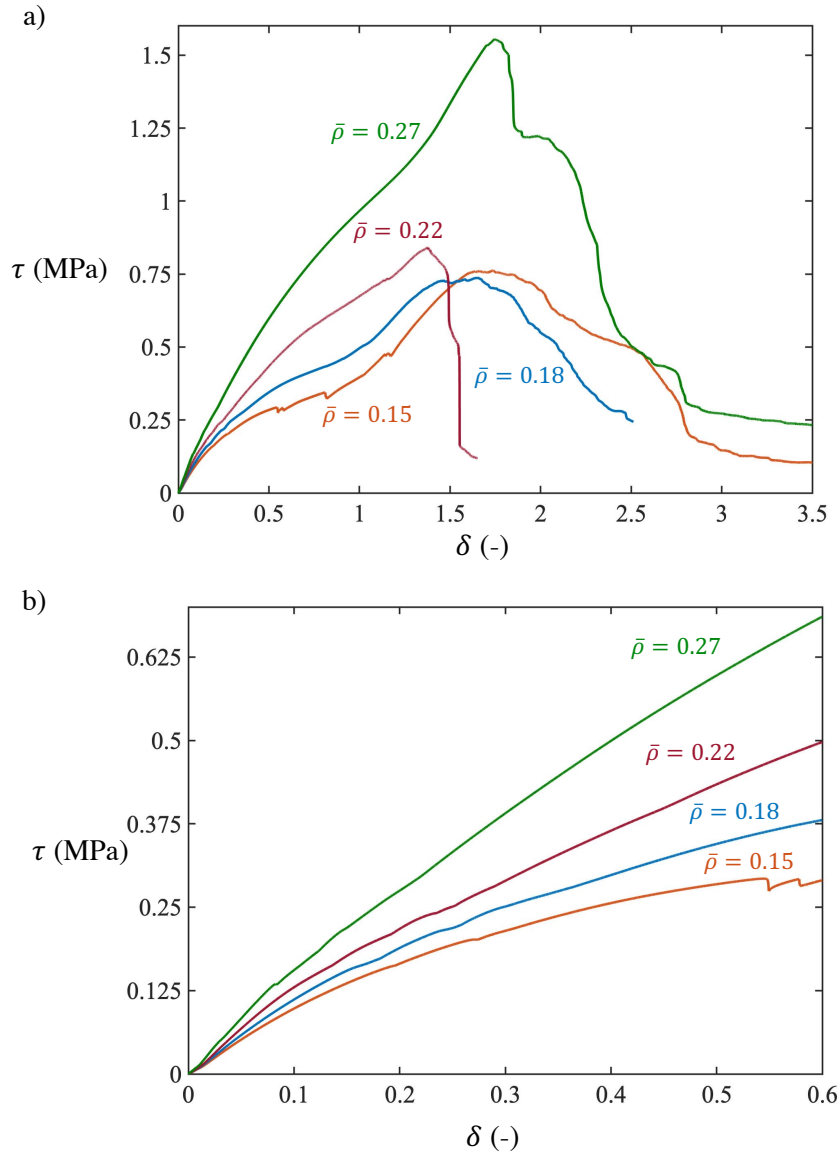
Figure 2.19: Shear Test Results for Regular Honeycomb with Varying $\bar{\rho}$
Average stress-strain relationships are shown for out-of-plane shear tests on regular honeycomb with four different $\bar{\rho}$ ranging from 15% to 27%. a) Shows the entire stress-strain curves, and b) shows a portion of the stress-strain curves in the linear-elastic regime only.

Shear modulus (G) increased with relative density ($\bar{\rho}$) (Table 2.2), and this effect was represented by a power regression with a coefficient of determination (R^2) of 0.90 (Figure 2.20).

Table 2.2: Average G for Regular Honeycomb with Varying $\bar{\rho}$
Average G results are given for out-of-plane shear tests on regular honeycomb with four different $\bar{\rho}$ ranging from 15% to 27%. N is the number of samples.

Average $\bar{\rho}$ (%)	N	Average G (MPa)
14.7 ± 0.1	3	0.83 ± 0.07
17.5 ± 0.3	3	0.91 ± 0.09
22.3 ± 0.1	3	0.98 ± 0.21
27.4 ± 0.2	2	1.28 ± 0.20
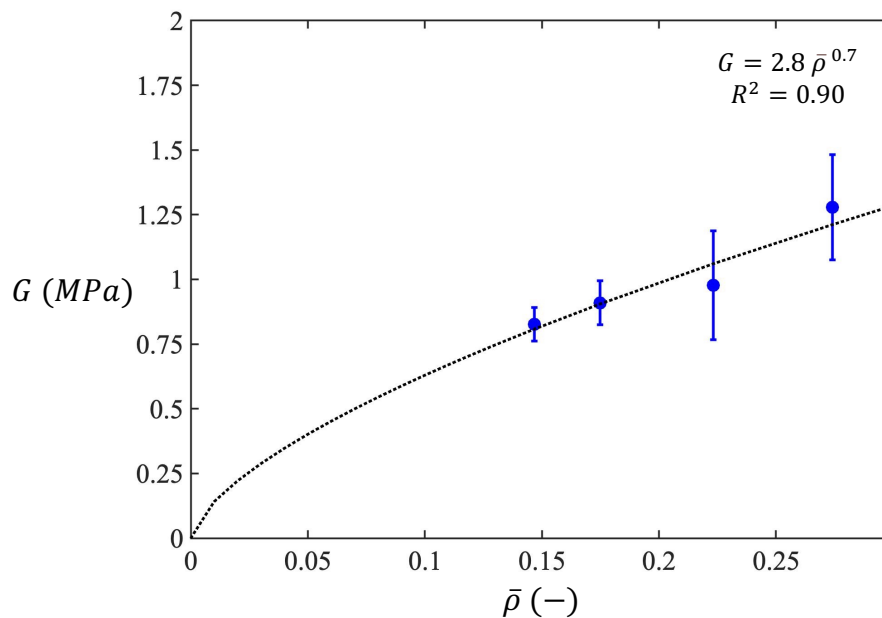
Figure 2.20: G with Respect to $\bar{\rho}$, Fit with a Power Regression
The relationship between G and $\bar{\rho}$ is shown, where the data points represent the average G for each $\bar{\rho}$ with standard deviation error bars. The data were fit with a power regression curve.

2.3.3   Determining the Most Suitable Honeycomb Relative Density

To determine the most suitable honeycomb design for head protection, a lower bound on relative density ($\bar{\rho}_{lower}$) of 17% was predicted by the power regression for honeycomb volumetric energy absorption (U_v) according to the properties of EPS foam (objective i.), and an upper bound on relative density ($\bar{\rho}_{upper}$) of 22.6% was predicted by the power regression for honeycomb

compressive peak stress (σ_p) according to the stress threshold for skull fracture (σ_c) (objective ii.).

The relative density ($\bar{\rho}$) that minimized shear modulus (G) was then determined using the regression relationship between these lower and upper limits (objective iii.). Based on these objectives the interception of shear modulus (G) and the lower limit gave the most suitable honeycomb relative density ($\bar{\rho}$) of 17% (Figure 2.21).
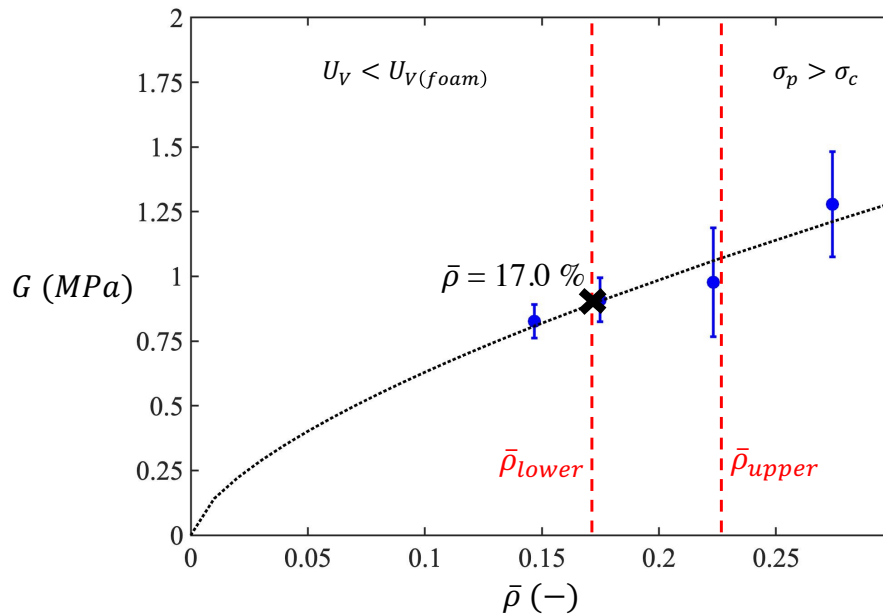
Figure 2.21: Determining the Most Suitable Honeycomb $\bar{\rho}$
The power regression for G with respect to $\bar{\rho}$ is shown, along with the lower and upper limits given by the results for objectives i. and ii. A relative density of 17% was determined to be most suitable for head protection.

2.4   Discussion

A bicycle helmet design was proposed using hexagonal honeycomb with pentagon-heptagon (5-7) defects. Out-of-plane compression and shear tests were performed, where it is critical for a helmet to absorb energy in these loading directions to prevent skull fracture and

diffuse TBI. The use of 3D-printing was beneficial in facilitating rapid prototyping of specific designs with varying geometries. The test samples were highly consistent in size and $\bar{\rho}$; and the size of the samples was representative of the structure that would attenuate energy during a helmeted collision. It is important to note that the samples were flat, not curved like in a full-scale bicycle helmet and this may have affected the results. However, this allowed results to be obtained on the material level and was an important simplification to make for ease of 3D-printing.

TPU was selected as the solid material with which the honeycomb samples were made since it is an elastomer, meaning that following the deformation of the structure, it could potentially restore its original shape and mechanical properties and allow reusability of the helmet for multiple impacts [61]. NinjaTek Cheetah was specifically chosen for its relatively high strength compared to other elastomeric materials to provide sufficient volumetric energy absorption (U_v) without densification occurring during an impact.

The properties of honeycomb were highly affected by relative density ($\bar{\rho}$), as expected [61]. This geometric parameter was altered to determine a design most suitable for both skull fracture and TBI protection. The design objectives were defined by relating head injury mechanisms to the mechanical properties of honeycomb including volumetric energy absorption (U_v), a measure of how much kinetic energy of the impact can be absorbed by the structure (objective i.); compressive peak stress (σ_p), which corresponds to the stress directly transmitted to the head upon impact (objective ii.); and shear modulus (G), which is related to the level of rotational head motion caused by an impact (objective iii.). The chosen design was based only on these properties and no consideration was made to the resulting weight of the helmet, which is important for its practical use and also may affect the inertia of the head upon impact.

Volumetric energy absorption (U_v) increased in relation to relative density ($\bar{\rho}$) in the tested range; however, for higher relative densities ($\bar{\rho}$), volumetric energy absorption (U_v) would be expected to reach a maximum and then decrease to approach the volumetric energy absorption (U_v) of the solid material. The energy absorption capacity of the EPS foam samples provided a benchmark for the minimum value of volumetric energy absorption (U_v) required (objective i.). This was used to determine a lower bound on honeycomb relative density ($\bar{\rho}$) to ensure the honeycomb helmet would meet testing standards and not reach densification during impact. Future design iterations could instead consider a design objective of maximizing volumetric energy absorption (U_v) while minimizing the weight of the helmet.

Compressive peak stress (σ_p) increased in relation to relative density ($\bar{\rho}$) and this relationship allowed an upper bound on relative density ($\bar{\rho}_{upper}$) to be determined according to the stress threshold for skull fracture (σ_c) (objective ii.). It is important to note that the threshold for skull fracture (σ_c) of 1.46 MPa used in this study does not represent the entire population, since injury thresholds vary with factors such as age and sex. However, this is aligned with industry standards where testing for protective equipment frequently uses thresholds based on average population response. Future honeycomb helmet designs could be tuned to best protect different populations.

Honeycomb designs with stacked and staggered 5-7 defects were tested because previous work showed that these arrangements promoted different collapse mechanisms and can strengthen or weaken the structure [92], consistent with the findings of the current study where the inclusion of 5-7 defects decreased the peak stress. 5-7 defects must be included to accommodate the curvature of the head; however, design choices were based on the properties of regular honeycomb, and therefore is an area for further investigation.

The honeycomb samples did not maintain their strength or energy absorption capability after they were compressed, which in high severity impacts (that can cause skull fracture) may be beneficial; however, it would be desirable to achieve elastic deformation under combined dynamic loading to reduce the need for helmet replacement – this is explored in Chapter 3. The honeycomb samples still showed potential for energy absorption in repeated impacts, especially compared to EPS foam. It is important to note that the honeycomb samples were compressed until after the onset of densification – under realistic impact conditions, densification would not likely occur, and as such the honeycomb may be more recoverable. As well, the 3D-printing process could have contributed to the plastic deformation of the cell walls and the design may be more recoverable with a different manufacturing process.

In out-of-plane shear tests, honeycomb samples exhibited linear-elastic behaviour followed by buckling and bulging of the cell walls, consistent with previous scientific research [61]. It is important to note that the test setup did not induce pure shear loading; however, due to the chosen dimensions of the samples, the normal force component was assumed to be negligible [98]. A relationship was obtained for shear modulus (G) with respect to relative density ($\bar{\rho}$) in the form of a power regression, and the most suitable design was chosen based on minimizing this parameter (objective iii.) in the corridor defined from objectives i. and ii. The primary outcome was shear modulus (G) due to its relationship to the rotational acceleration of the head following impact (Appendix B). With the design objective of minimizing shear modulus (G), an assumption was made that the shear deformation experienced in an impact would not exceed the linear-elastic region and this should be tested in future work. The ratio of yield stress to compressive stress as a measure of the anisotropy of the structure could also be considered, where greater anisotropy would be beneficial for simultaneous protection against skull fracture and diffuse TBI.

A limitation of the current study is that mechanical testing was primarily performed at a quasi-static strain rate ($\dot{\varepsilon}$), which is not representative of a realistic head impact in a bicycle accident. Therefore, the rate dependence of honeycomb was explored using strain rates ($\dot{\varepsilon}$) up to 6×10^{-2} /s, which was limited by the capability of the Instron materials testing machine. The results showed that peak stress (σ_p) and volumetric energy absorption (U_v) increased with strain rate ($\dot{\varepsilon}$) and therefore this factor should be considered when determining the most suitable honeycomb design for head protection (Chapter 3). Strain rates ($\dot{\varepsilon}$) representative of a real-world head impact should be explored.

The findings of this study suggest that honeycomb geometry can be modified to develop a design suitable for head protection. The honeycomb helmet design demonstrated potential to effectively protect against both skull fracture and TBI, by mitigating the radial and tangential force components.

Chapter 3 – Dynamic Impact Testing

Overview: Since real-world accidents typically occur at high velocities, dynamic impact testing was performed to explore the effectiveness of the honeycomb design in comparison to EPS foam. A twin wire drop tower setup was used to induce both radial (pure compression) and oblique (combined compression and shear) loading on the samples. The anisotropy of the honeycomb design compared to EPS foam was highlighted, which is beneficial for traumatic brain injury protection. The design also showed potential to be reusable for multiple impacts. Finally, strain rate sensitivity of the honeycomb design was highlighted, indicating the need to scale the design for protection in dynamic impacts.

3.1   Introduction

Head impacts in real-world bicycle accidents are typically oblique with respect to the impact surface and transmit both radial and tangential forces to the head, which cause linear and rotational head kinematics, respectively (Figure 1.4). The ability of a helmet to mitigate these head kinematics is directly related to the mechanical properties of the structure in compressive and shear loading (Figure 2.1).

Expanded polystyrene (EPS) foam, which is the most commonly used bicycle helmet material, sufficiently mitigates radial forces and linear head kinematics and therefore has been shown to be effective in preventing skull fracture and some traumatic brain injuries (TBIs) [12, 13]. However, EPS foam does not adequately mitigate tangential forces and rotational head

kinematics and therefore is not effective in preventing many types of TBI such as concussion and diffuse axonal injury (DAI) [64]. The limitations of EPS foam helmets are highly attributed to the insufficient deformation that is achievable under shear loading [61, 66]. Hexagonal honeycomb has many features that could make it suitable for head protection, especially its anisotropy, where the shear strength (τ_p) is lower than the compressive strength (σ_p) [61, 93] to allow sufficient deformation for mitigation of rotational head kinematics. As well, honeycomb can be made from elastomeric materials with the potential to be recoverable and therefore effective for repeated impacts without requiring replacement.

A drop tower test setup is commonly used for standardized helmet testing (Figure 1.11) [77] and advanced helmet testing involving an oblique impact surface [60, 71, 75]. In oblique tests, helmets are evaluated based on the linear and rotational kinematics of an anthropomorphic test device (ATD) headform following impact. For drop tower tests that involve an ATD head only (no neck), the mass of the drop assembly is typically 5.0 ± 0.1 kg [77]. Impact velocities of 4.8 m/s and 6.2 m/s have been targeted with platen angles (θ) of 30°, 45°, and 60° from the horizontal to represent real-world accidents [60, 71, 75]. Oblique drop tower testing would be considered a combined loading scenario, transmitting both compressive and shear forces to the helmet. In the process of designing a helmet for skull fracture and TBI protection, it would be beneficial to replicate these drop tower impacts but on a smaller scale, before developing full-scale helmet prototypes.

In Chapter 2 the compressive and shear properties of various honeycomb designs were explored independently, under quasi-static conditions. From these results, one honeycomb design was chosen as the most suitable for skull fracture and TBI protection. Here, the effectiveness of the chosen design was explored through dynamic drop tower impact tests on small, flat honeycomb

and EPS foam samples, where combined compressive and shear loading was produced at impact velocities and energies seen in real-world bicycle accidents. The goals of the study were to determine the effect of impact velocity (v_i) and the effect of an angled compared to flat impact (combined loading versus pure compressive loading) on the honeycomb peak compressive stress (σ_p), peak shear stress (τ_p), and energy absorption per unit volume (U_v). As well, the reusability of the honeycomb design was explored and comparisons to EPS foam were made.

3.2   Methods

3.2.1   Test Setup

Honeycomb samples with a target relative density ($\bar{\rho}$) of 17% were generated in nTopology (New York, USA), and 3D-printed (Appendix C) with thermoplastic polyurethane (TPU) filament, Ninjatek Cheetah (Ninjatek, Manheim, USA), an elastomeric material, which has a density of 1.22 g/cm^3, a tensile strength of 39 MPa, a hardness of 95 Shore A, and an elongation at break of 580%. The area of the samples was 8840 mm^2, which was consistent with compression testing samples in Chapter 2 and with the average contact area in a helmeted bicycle accident [97]. The thickness of the samples (25 mm) was chosen for consistency with typical EPS foam bicycle helmets and samples in Chapter 2. Facesheets with a 1 mm thickness that extended 0.5 mm on each side were 3D-printed onto the bottom surface of the honeycomb structures with the same TPU material to increase the surface area for adhesion to the testing apparatus (Figure 3.2b). EPS foam samples with identical dimensions and a density of 85 kg/m^3 were obtained (Seven Star Sports, Hamilton, Ontario, Canada). Custom test setups were designed for dynamic impacts to these flat honeycomb and EPS foam samples on flat and angled platens (Appendix D).

The test setup (Figure 3.1) consisted of a flat steel impactor mounted to a National Operating Committee on Standards for Athletic Equipment (NOCSAE) carriage. The carriage together with the impactor weighed 3.9 kg. Weights were added to the impactor to reach a total of 5.0 kg. This weight was selected to mimic the mass of the human head and to match Consumer Product Safety Commission (CPSC) standards [77]. The carriage was guided by two vertical wires and dropped onto the test sample, sitting on a steel platen.
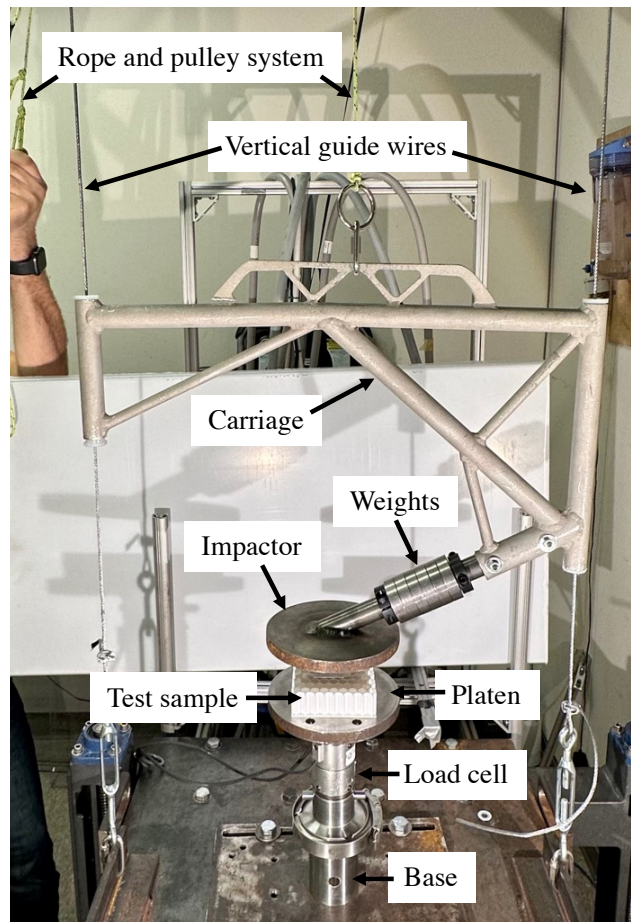
Figure 3.1: Impact Testing Setup
The dynamic test setup consisted of a flat steel impactor mounted to a NOCSAE carriage, which was guided by two vertical wires and dropped onto the test sample, sitting on a platen and load cell.

Three different impact scenarios were tested:

i.   Slow, flat platen: target impact velocity (v_i) of 4.8 m/s with a horizontal platen and impactor (Figure 3.2a)

ii.   Fast, flat platen: target impact velocity (v_i) of 6 m/s with a horizontal platen and impactor (Figure 3.2a)

iii.   Slow, angled platen: target impact velocity (v_i) of 4.8 m/s with the platen and impactor angled at 45° from the horizontal (Figure 3.2b)

For impact scenarios i. and iii., tests were performed on both honeycomb and EPS foam samples to determine the effect of impact angle (θ) and identify any differences in behaviour between the two cellular structures. For impact scenario ii., tests were performed on honeycomb samples only to determine the effect of impact velocity (v_i) on honeycomb behaviour. Three samples (N = 3) were tested for each group. For all impact scenarios, three tests were performed consecutively on each sample to explore the potential for reusability of honeycomb and EPS foam.

A 6-axis load cell was mounted between the platen and the base. The output signals from the load cell were collected using a data acquisition system (PXIe-1082, National Instruments, Austin, Texas, USA) and custom-written LabVIEW® (National Instruments, Austin, TX, USA) program (Appendix F) at a sampling rate of 50 kHz. The load cell was zeroed prior to performing tests for each impact scenario. For flat platen tests, force was recorded in the z-direction only (Figure 3.2a); and for angled platen tests, force was additionally measured in the x-direction (Figure 3.2b).

A MEMRECAM HX-3 (nac Image Technology, Tokyo, Japan) high-speed camera was placed in line with the test sample to capture a series of images for all impacts. The camera provided 1024 × 520 pixel resolution and recorded footage at 7,500 frames per second. Two

spotlights were directed toward the impact area from behind the high-speed camera to offer a clear view of the impact.

a)

b)
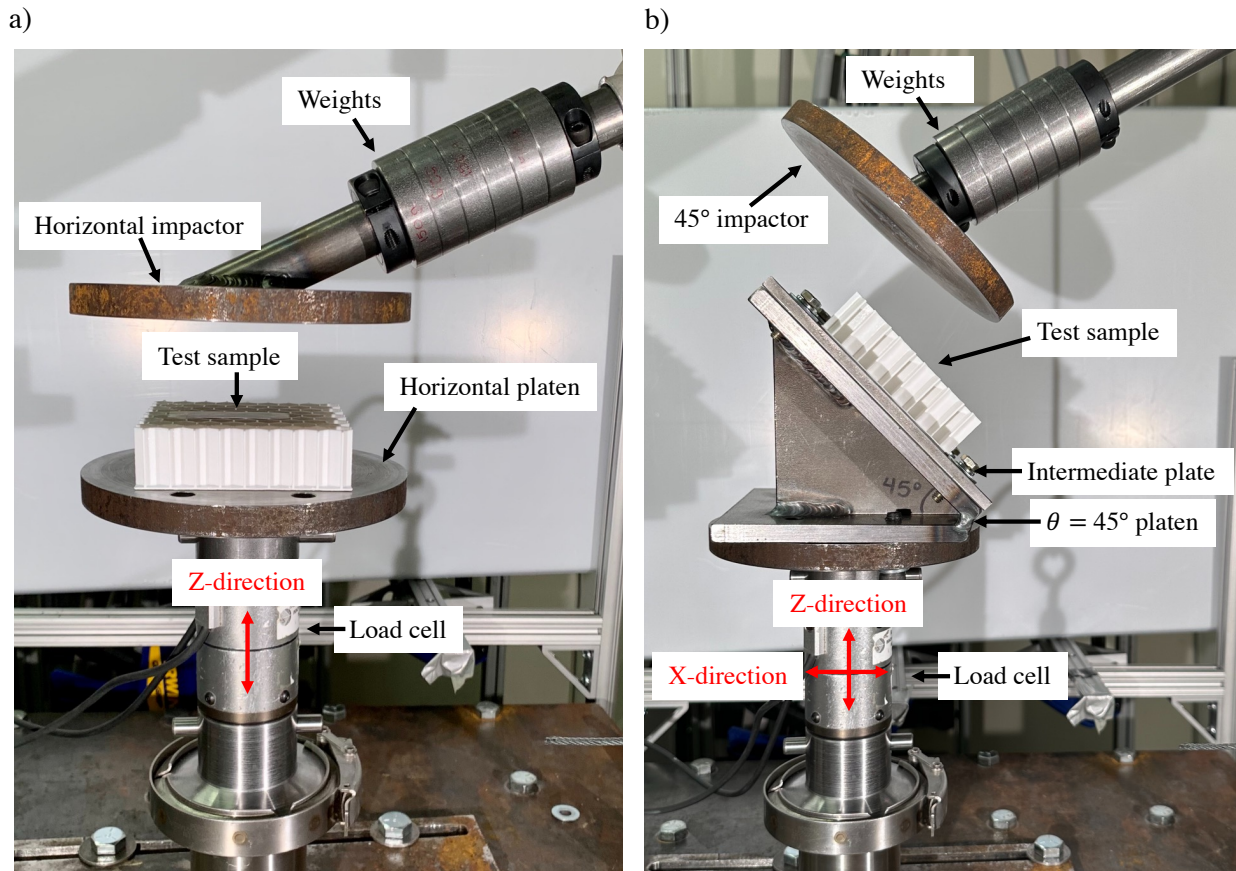
Figure 3.2: Impact Testing Scenarios
a) Shows the flat impact scenario with a horizontal platen and impactor, where load was measured in the Z-direction; and b) shows the angled impact scenario with a platen and impactor angled at $\theta = 45°$ with respect to the horizontal, where load was measured in the Z-direction and X-direction.

For the oblique tests, the honeycomb samples were glued on one side to steel plates using Loctite 414 cyanoacrylate (Henkel, Düsseldorf, Germany), which has a shear strength of 18-26 N/mm^2. A thin layer of the adhesive was applied to both the honeycomb facesheet and the steel plate, then the honeycomb sample was aligned in the centre of the plate and pressure was applied for 30 seconds. The samples were left to cure for 24 hours to allow the glue to fully cure, as per

package instructions. The identical procedure was followed for adhering EPS foam samples to steel plates; however, to avoid dissolving the foam, LePage epoxy (Henkel, Düsseldorf, Germany) was used, which has a shear strength of 24.8 ± 0.49 N/mm².

3.2.2   Data Analysis

Impact velocity (v_i) for each test was determined by the position of the impactor in the high-speed camera footage. Deformation was also determined from high-speed camera footage where the position of the front, bottom edge of the impactor was recorded in each frame from the first observable contact on the sample (Figure 3.7 a, c, and e; and Figure 3.14 a and c), to the point of maximum deformation (Figure 3.7 b, d, and f; and Figure 3.14 b and d) using ImageJ (NIH, Bethesda, Maryland, USA) with the MTrackJ plugin. Load-deformation data were converted to stress-strain data based on initial sample dimensions.

The following data analysis was performed in MATLAB (MathWorks, Natick, Massachusetts, USA) (Appendix E). For angled platen impact tests, compressive and shear forces were calculated from the load cell data in two axes using a rotation matrix. The primary outcomes were peak compressive stress (σ_p), energy absorption per unit volume (U_v), and peak shear stress (τ_p). Volumetric energy absorption (U_v) was calculated as the integral of the stress-strain curve until the point of maximum deformation.

Unpaired t-tests assuming equal variances were performed to detect differences between initial slow and fast impacts, and slow impacts on honeycomb versus EPS foam. To give adequate power, a two-way ANOVA was performed to detect any differences in average compressive peak stress (σ_p) or volumetric energy absorption (U_v) between slow and fast impacts, pooling the results for initial and repeated impacts. A two-way ANOVA was performed to detect differences between

the first, second, and third impacts on honeycomb, pooling the slow and fast impacts. A one-way ANOVA was performed to detect differences between the first, second, and third impacts on EPS foam in the slow impact scenario. For angled platen tests, t-tests were performed to detect any difference between compression and shear, and between honeycomb and EPS. T-tests were also performed to detect differences in compressive peak stress (σ_p) between flat and angled impacts. One-way ANOVAs were performed to detect differences between the first, second, and third impacts on each structure and in each loading direction. A level of significance (α) of 0.05 was used in all statistical tests and post hoc Tukey tests were performed following all ANOVAs.

3.3 Results

Regular honeycomb samples were 3D-printed with an average relative density ($\bar{\rho}$) of 16.2 ± 1.1%. The average impact velocities (v_i) were 4.85 ± 0.09 m/s and 5.76 ± 0.04 m/s for slow and fast impact scenarios, respectively. Honeycomb stress-strain responses were compared between slow and fast impact velocities on the flat platen (Figure 3.3a and Figure 3.3b).
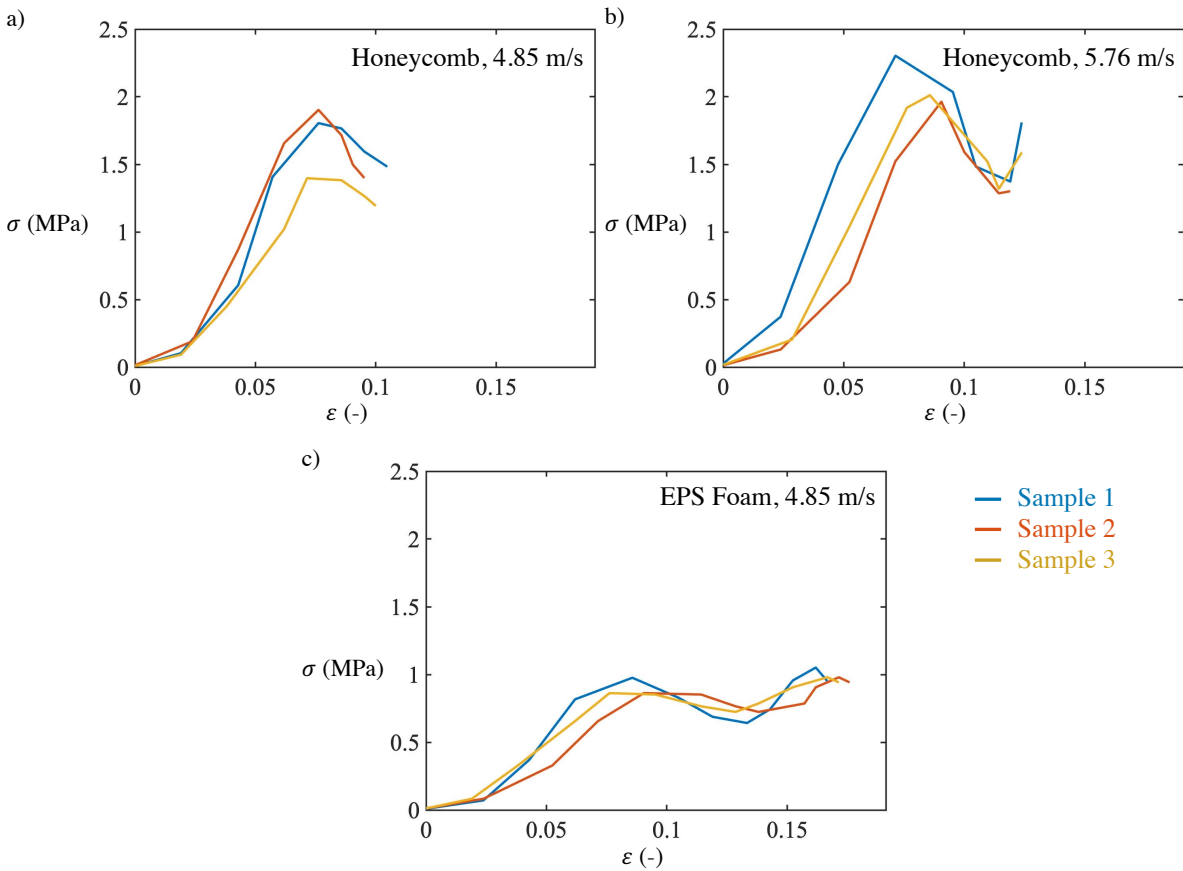
Figure 3.3: Stress-Strain Results for Flat Platen Impact Tests
Stress-strain curves for flat platen impact tests are shown for a) honeycomb under the slow impact condition (4.85 m/s), b) honeycomb under the fast impact condition (5.76 m/s), and c) EPS foam under slow impact condition (4.85 m/s).

Considering the initial impacts only, average compressive peak stress (σ_p) increased by 23% (p = 0.09) and volumetric energy absorption (U_v) increased by 41% (p = 0.17), in the fast compared to slow impacts; however, these differences were not statistically significant (Figure 3.4).
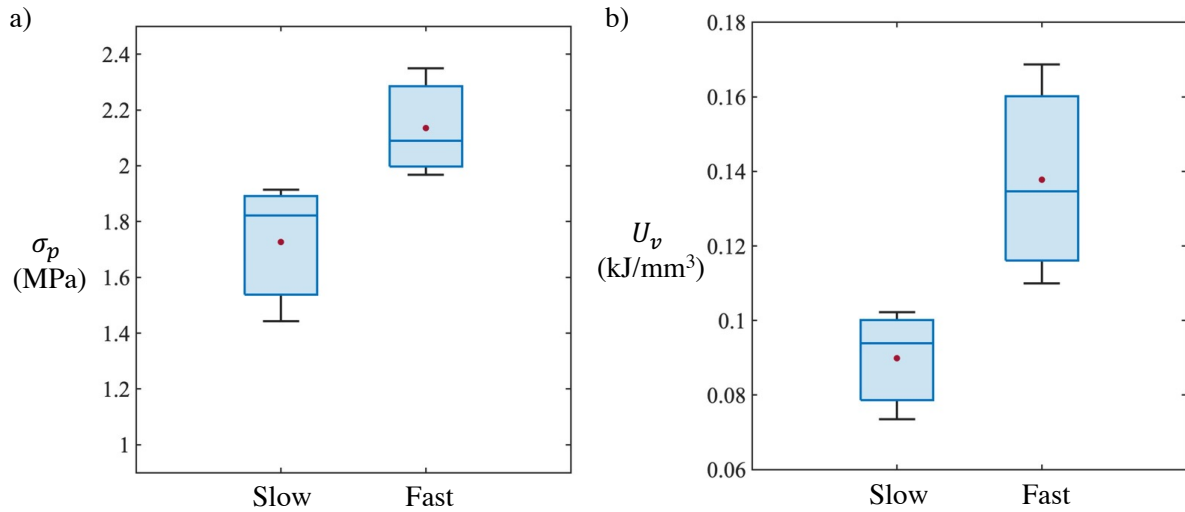
Figure 3.4: σ_p and U_v Results for Initial Slow and Fast Impacts
Average σ_p and U_v results are shown for flat impact tests (initial impacts only) under slow and fast impact conditions. The median is given by the line inside each box, the edges of the box are the lower and upper quartiles, the whiskers represent the lowest and highest values, and the red dot is the mean.

In pooling means for all initial and repeated impacts, average compressive peak stress (σ_p) and volumetric energy absorption (U_v) significantly increased by 17% (p = 0.023) and 45% (p = 0.0005), respectively, in the fast compared to slow impacts (Figure 3.5).

a)

b)
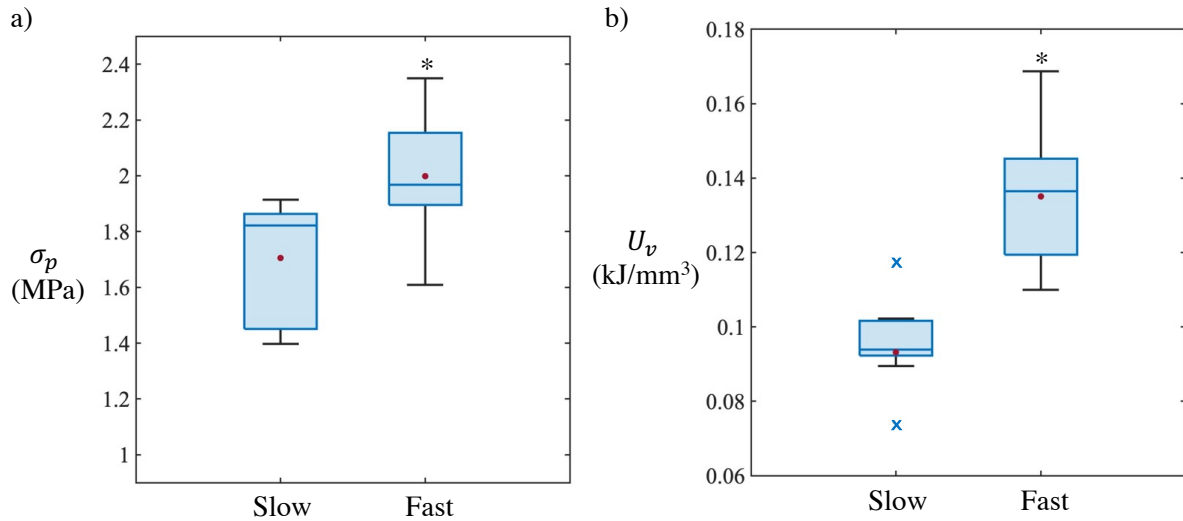
Figure 3.5: σ_p and U_v Results for Slow and Fast Impacts

Average σ_p and U_v results are shown for flat impact tests (pooled results) under slow and fast impact conditions. The median is given by the line inside each box, the edges of the box are the lower and upper quartiles, the whiskers represent the lowest and highest values, the red dot is the mean, and the blue x's are outliers. An asterisk (*) shows a significant difference from the slow impact condition (p < 0.05).

For the slow, flat platen impact scenarios, stress-strain responses were compared between honeycomb and EPS foam (Figure 3.3a and Figure 3.3c). Average compressive peak stress (σ_p) was 39% lower for EPS foam compared to honeycomb (p = 0.01) (Figure 3.6a). Average volumetric energy absorption (U_v) was 22% higher for EPS foam compared to honeycomb; however, this difference was not statistically significant (p = 0.16) (Figure 3.6b).
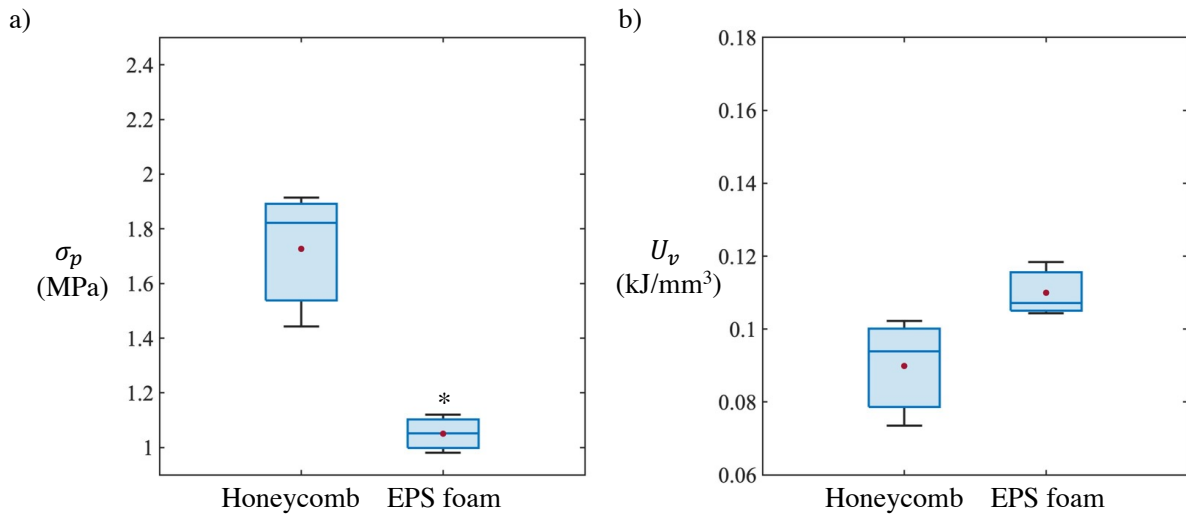
a)

b)

Figure 3.6: σ_p and U_v Results for Honeycomb and EPS Foam
Average σ_p and U_v results are shown for flat impact tests (initial impacts only) on honeycomb and EPS foam. The median is given by the line inside each box, the edges of the box are the lower and upper quartiles, the whiskers represent the lowest and highest values, and the red dot is the mean. An asterisk (*) shows a significant difference from the slow impact condition ($p < 0.05$).

For flat platen impacts, honeycomb samples experienced some buckling of the cell walls at the point of maximum deformation (Figure 3.7b). A greater degree of cell wall buckling was observed in high-speed camera footage for the fast compared to the slow impact scenario (Figure 3.7d). All honeycomb samples returned to their original dimensions according to measurements taken in from camera footage following each impact. In comparison, EPS foam samples experienced deformation in the form of crack propagation (Figure 3.7f), and their thickness was permanently reduced following each impact by an average of 2.75 mm.
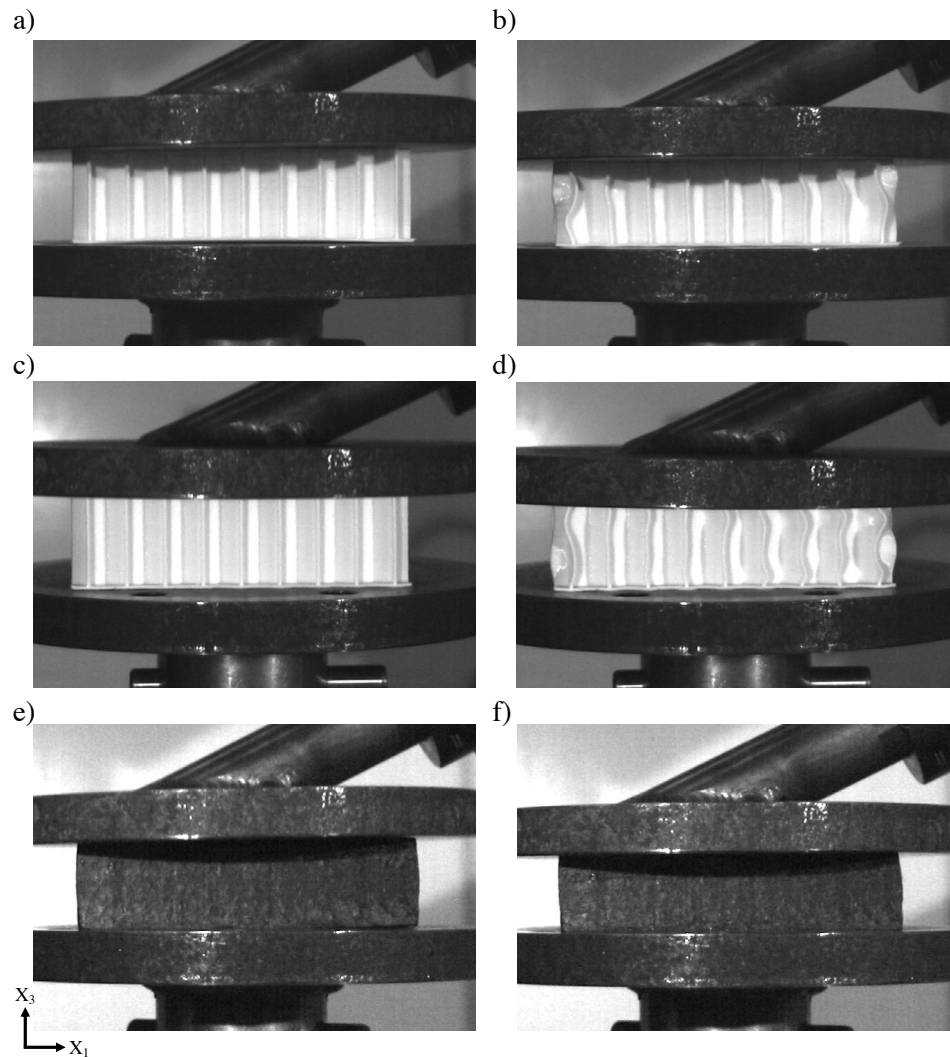
Figure 3.7: Deformation Patterns for Flat Platen Impacts
Photographs of honeycomb and EPS foam samples are shown at the point of first contact (a, c, and e) and the point of maximum deformation (b, d, and f). a) and b) show honeycomb in the slow impact scenario. c) and d) show honeycomb in the fast impact scenario. e) and f) show EPS foam in the slow impact scenario.

Honeycomb stress-strain responses were compared among initial and repeated impacts – an example for the slow impact condition is given in Figure 3.8a and an example for the fast impact condition is given in Figure 3.8b.
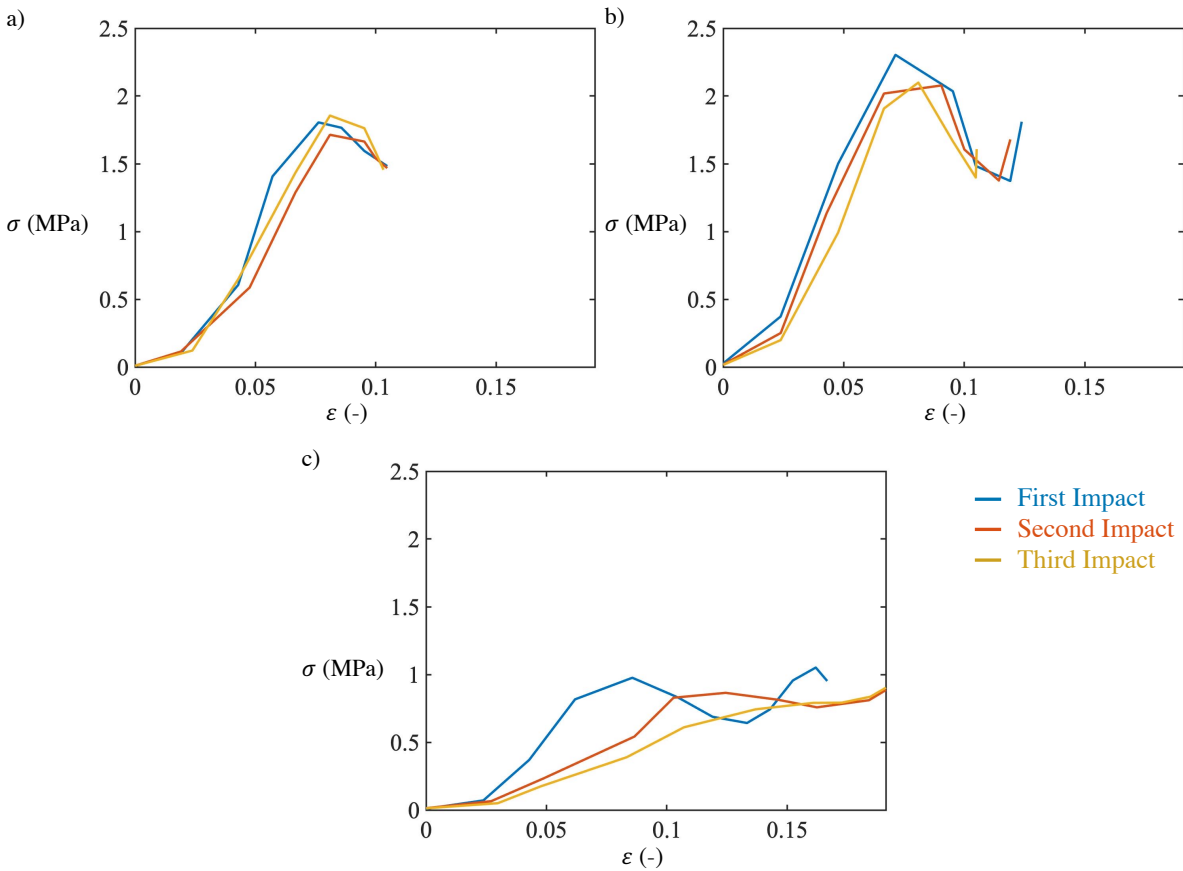
Figure 3.8: Example Stress-Strain Results for Repeated Flat Platen Impact Tests
Example stress-strain curves are for repeated flat platen impact tests are shown for a) honeycomb under the slow impact condition, b) honeycomb under the fast impact condition, and c) EPS foam under the slow impact condition. Blue is the first (initial) impact, orange is the second impact, and yellow is the third impact.

There were no significant differences in average compressive peak stress (σ_p) or volumetric energy absorption (U_v) among the initial impact and the repeated impacts when results for slow and fast impact scenarios were pooled (Figure 3.9).

a)

b)
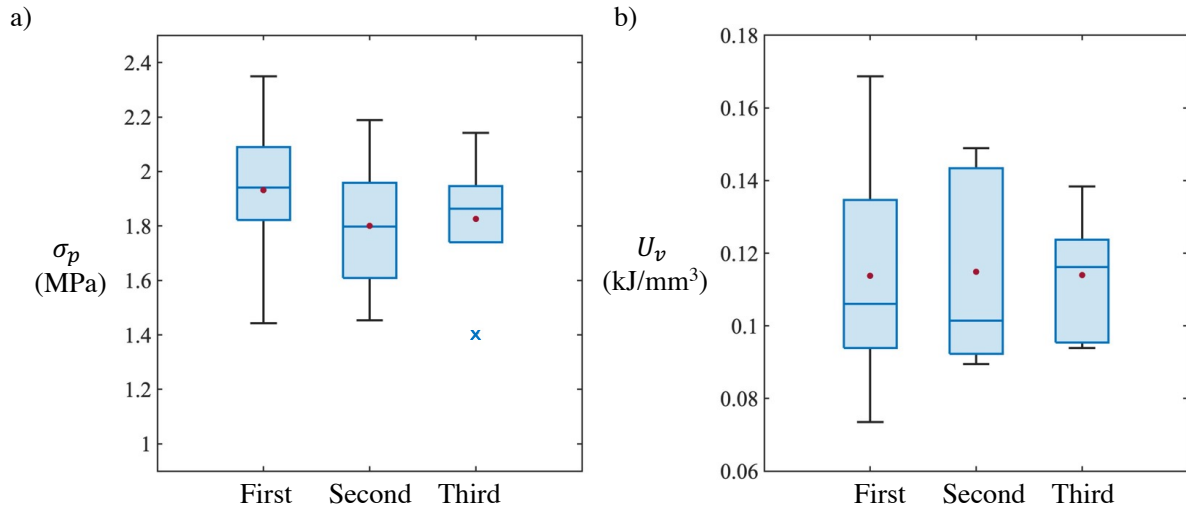
Figure 3.9: σ_p and U_v Results for Initial and Repeated Impacts on Honeycomb
Average σ_p and U_v results are shown for the first, second, and third flat platen impact tests on honeycomb. The median is given by the line inside each box, the edges of the box are the lower and upper quartiles, the whiskers represent the lowest and highest values, the red dot is the mean, and the blue x's are outliers.

EPS foam stress-strain responses were compared between initial and repeated impacts – an example is given in Figure 3.8c. There were no significant differences in compressive peak stress (σ_p) or volumetric energy absorption (U_v) among the first, second, and third impacts (Figure 3.10).

76

a)

b)
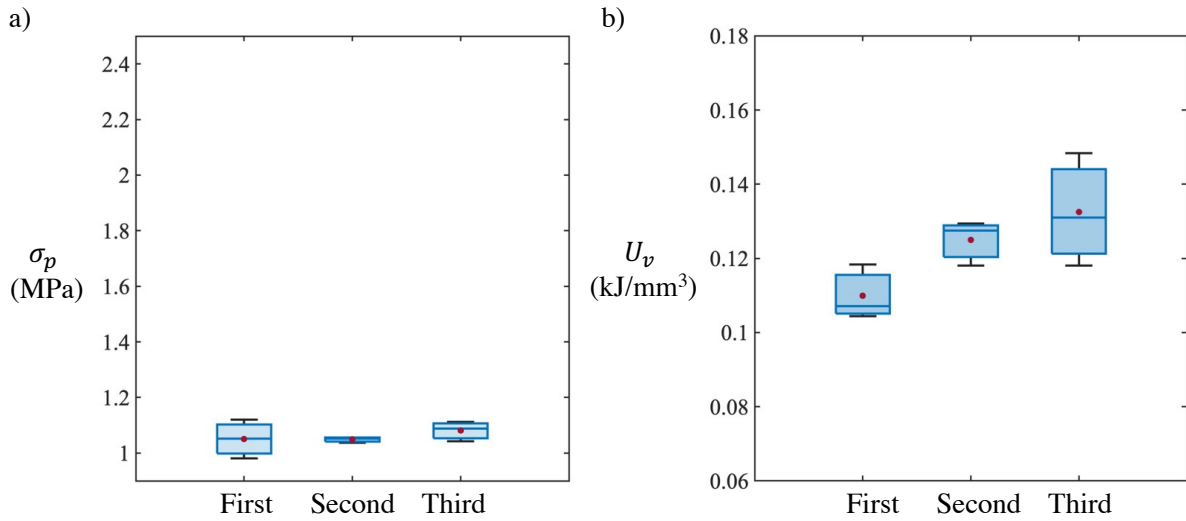
Figure 3.10: σ_p and U_v Results for Initial and Repeated Impacts on EPS Foam
Average σ_p and U_v results are shown for the first, second, and third flat platen initial impacts on EPS foam. The median is given by the line inside each box, the edges of the box are the lower and upper quartiles, the whiskers represent the lowest and highest values, and the red dot is the mean.

Compressive and shear stress (σ and τ) responses were compared for honeycomb and EPS foam samples – examples are given in Figure 3.11.
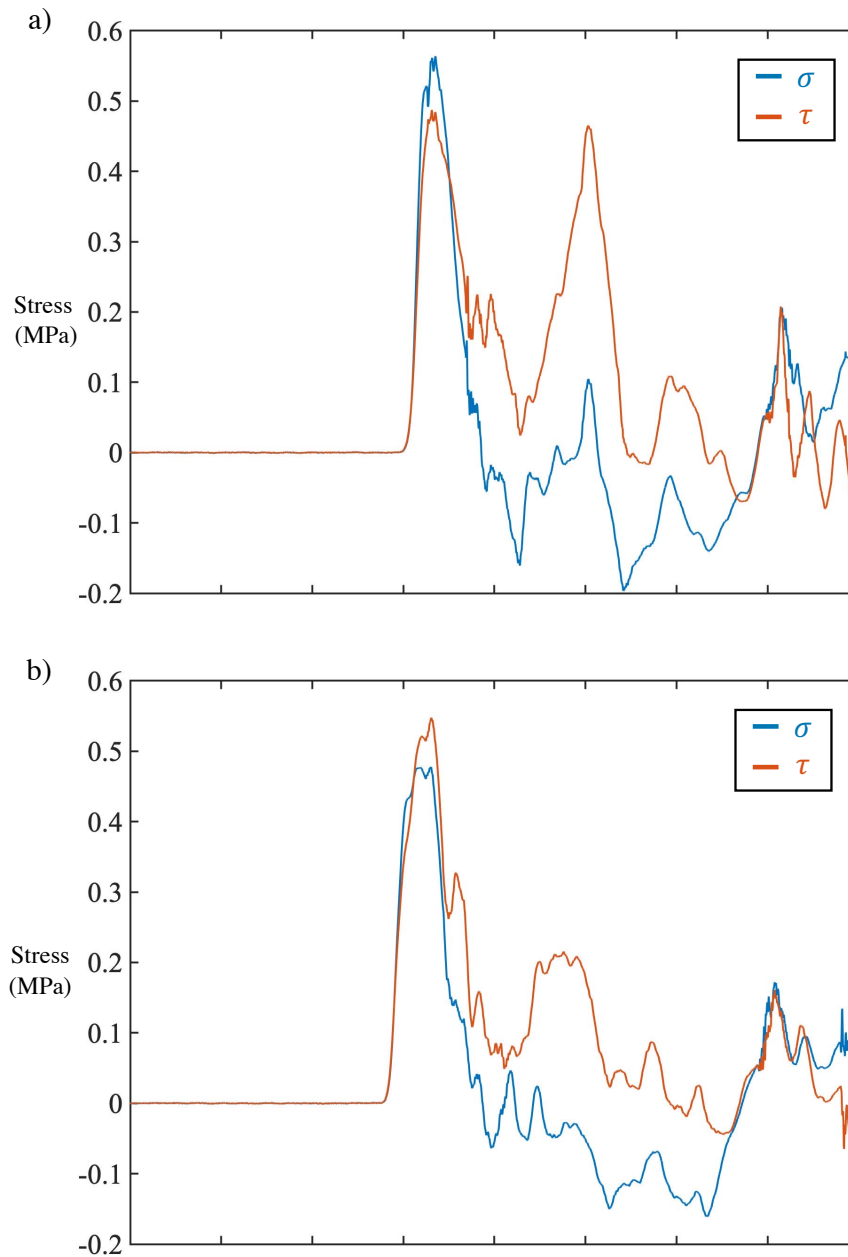
Figure 3.11: Example σ and τ Results for Angled Platen Impact Tests
Example stress-time curves are shown for angled platen impact tests. a) Shows results for honeycomb and b) shows results for EPS foam. Blue is σ and orange is τ.

In terms of anisotropy, there were significant differences in mechanical response between

compressive and shear loading directions. For honeycomb samples, average shear peak stress (τ_p)

78

was 10% lower than compressive peak stress (σ_p) (Figure 3.12a). In comparison, for EPS foam

samples shear peak stress (τ_p) was 15% higher than compressive peak stress (σ_p) (Figure 3.12b).
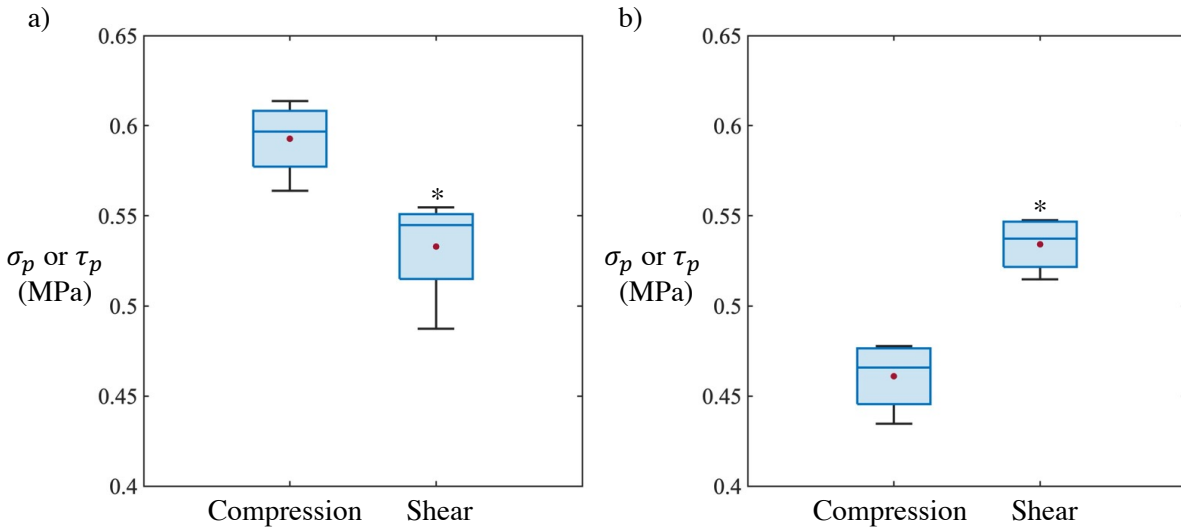
Figure 3.12: Peak Stress Results for Compressive and Shear Loading
Average stress results are shown for σ_p and τ_p for angled platen impact tests. a) Shows results
for honeycomb and b) shows results for EPS foam. The median is given by the line inside each
box, the edges of the box are the lower and upper quartiles, the whiskers represent the lowest and
highest values, and the red dot is the mean. An asterisk (*) shows a significant difference from
compressive stress (p < 0.05).

The average compressive peak stress (σ_p) was 22% higher for honeycomb compared to

EPS foam (Figure 3.13a); however, shear peak stress (τ_p) results were not different (Figure 3.13b).

a)

b)
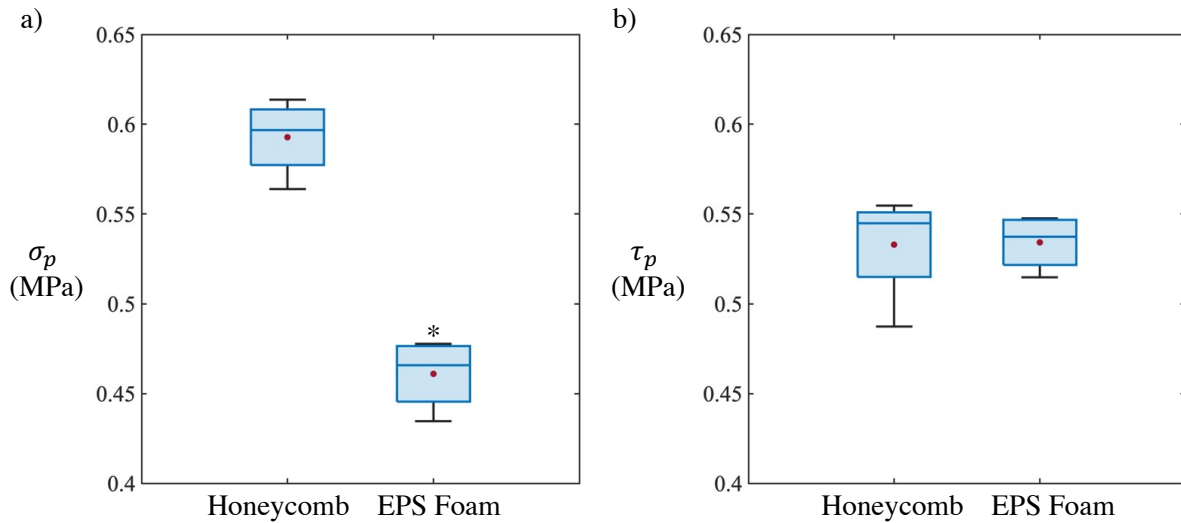
Figure 3.13: σ_p and τ_p Results for Honeycomb and EPS Foam
Average σ_p and τ_p results are shown for initial angled impact tests on honeycomb and EPS
foam. The median is given by the line inside each box, the edges of the box are the lower and
upper quartiles, the whiskers represent the lowest and highest values, and the red dot is the mean.
An asterisk (*) shows a significant difference from honeycomb ($p < 0.05$).

For angled platen impacts, honeycomb samples experienced combined buckling and shear
tilting of the cell walls at the point of maximum deformation (Figure 3.14b) and returned to their
original shape following impact. A lesser degree of cell wall buckling was observed compared to
in flat platen impacts. In comparison, EPS foam samples experienced combined compressive and
shear deformation in the form of crack propagation, and their shape was permanently altered as a
result of each impact (Figure 3.14d). The platen and impactor were not exactly parallel, as
observed by analyzing high camera footage video after testing. Therefore, the degree of
deformation was inconsistent on different parts of the samples, a uniform strain could not be
measured, and volumetric energy absorption (U_v) was not presented.
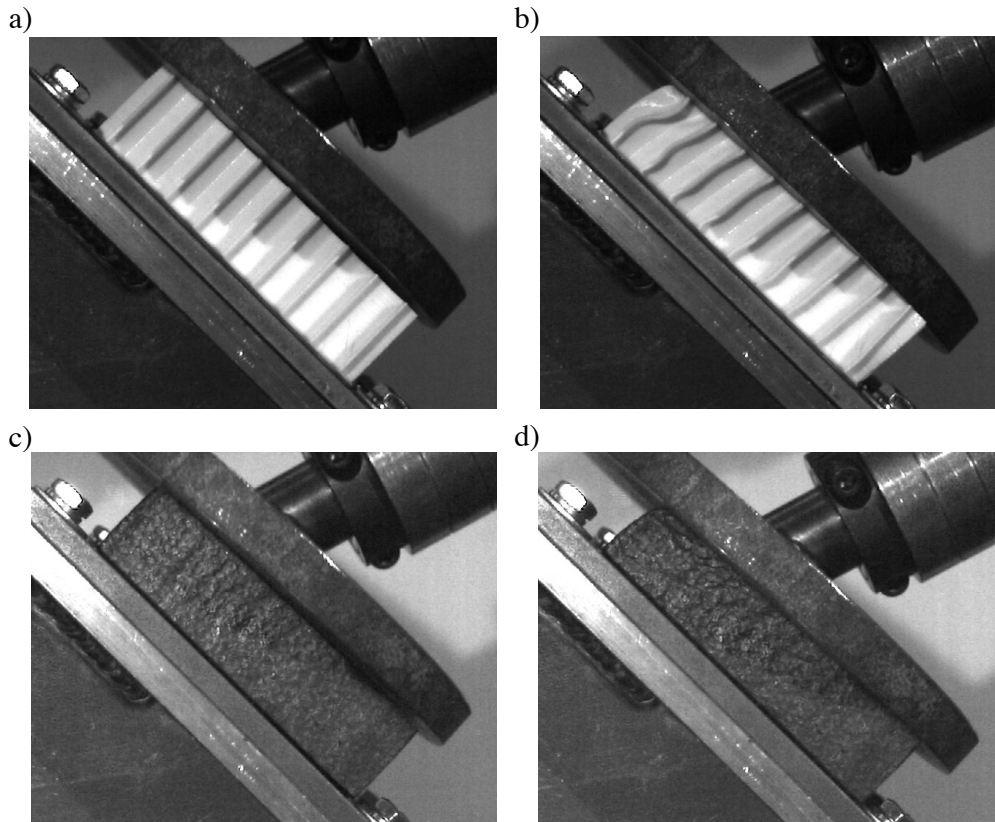
Figure 3.14: Deformation Patterns for Angled Platen Impacts
Photographs of honeycomb and EPS foam samples are shown at the point of first contact (a and c) and the point of maximum deformation (b and d).

There were no significant differences in compressive peak stress (σ_p) or shear peak stress (τ_p) between the initial impact and repeated impacts for honeycomb (Figure 3.15a and Figure 3.15b). In comparison compressive peak stress (σ_p) and shear peak stress (τ_p) increased significantly (by 9 to 15%) between initial and repeated impacts on EPS foam samples (Figure 3.15c and Figure 3.15d).
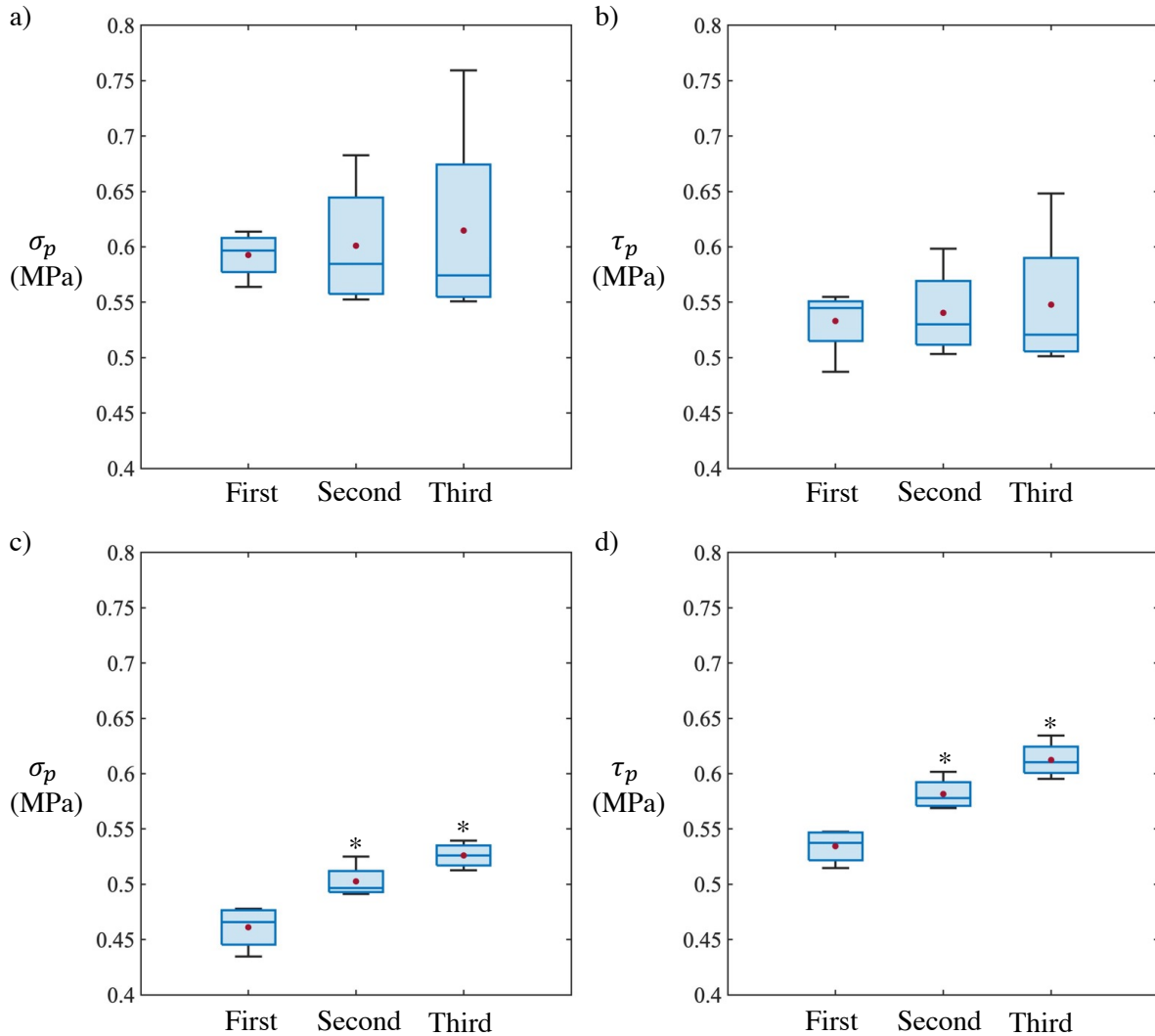
Figure 3.15: σ_p and τ_p Results for Initial and Repeated Impacts

Average σ_p and τ_p results are shown for the first, second and third angled platen impact tests. a) and b) Show results for honeycomb. c) and d) Show results for EPS foam. The median is given by the line inside each box, the edges of the box are the lower and upper quartiles, the whiskers represent the lowest and highest values, and the red dot is the mean. An asterisk (*) shows a significant difference from the first impact (p < 0.05).

Compressive peak stress (σ_p) results were compared between flat and angled impact scenarios (i. and iii.) and significant differences were found. Honeycomb compressive peak stress (σ_p) was 66% lower for angled platen tests compared to flat platen tests (Figure 3.16a). Similarly,

EPS foam compressive peak stress (σ_p) was 56% lower for angled platen tests compared to flat platen tests (Figure 3.16b).
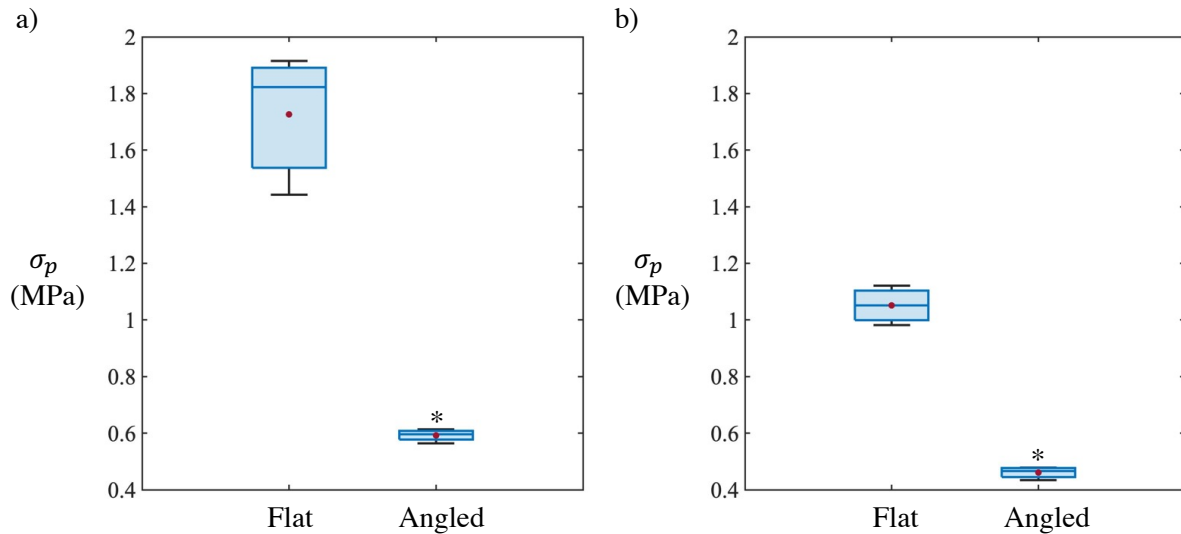
Figure 3.16: σ_p for Flat and Angled Impacts onto Honeycomb and EPS Foam
Average σ_p results are shown for initial flat and angled platen impacts. a) Shows results for honeycomb and b) shows results for EPS foam. The median is given by the line inside each box, the edges of the box are the lower and upper quartiles, the whiskers represent the lowest and highest values, and the red dot is the mean. An asterisk (*) shows a significant difference from the flat impact condition ($p < 0.05$).

3.4   Discussion

The effectiveness of hexagonal honeycomb for head protection in bicycle accidents was explored through drop tower impact tests on small, flat samples. The custom test setup successfully achieved pure compression and combined compressive and shear loading scenarios. As well, impact velocities and energies that represent real-world bicycle accidents were attained. The test samples were highly consistent in size and relative density ($\bar{\rho}$); and the size of the samples was representative of the structure that would attenuate energy during a helmeted collision and consistent with samples used in Chapter 2.

It is important to note that the samples were flat, not curved like in a full-scale bicycle helmet and this may have affected the results. This was however an important simplification to make for ease of 3D-printing and in using the results in conjunction with Chapter 2 results to make future design choices. As well, mitigation of head kinematics was assumed to be dependent on the honeycomb mechanical properties alone, whereas other factors may affect this, such as the weight of the helmet.

The conditions used in previous studies that performed full-scale oblique drop tower helmet testing were targeted. The fast impact velocity (v_i) of 5.76 m/s did not match the target of 6.2 m/s, which is used in testing standards, due to the height limitation of the drop tower. The difference between slow and fast impact velocities still allowed for comparisons and allowed strain rate dependence to be determined in the range of impact velocities seen in real-world accidents.

Results suggested that impact velocity (v_i) had a significant effect on honeycomb compressive peak stress (σ_p) in flat platen impact tests, which indicated the honeycomb's sensitivity to strain rate. Since the tested honeycomb design was based on the results of quasi-static testing (Chapter 2), this suggested the design should be scaled to ensure the compressive peak stress (σ_p) does not exceed the skull fracture threshold (σ_c), even for high-velocity impacts. However, the honeycomb samples also absorbed significantly more energy in the fast impact condition – this is likely due to the higher levels of deformation achieved. The differences between slow and fast impact scenarios were not statistically significant considering only the initial impacts; however, this is likely due to the small sample size, which is a limitation of the study. Densification did not occur in any of the impacts, also suggesting the possibility of reducing the strength of the design in the future.

Compressive peak stress (σ_p) and volumetric energy absorption (U_v) were significantly higher for honeycomb compared to EPS foam, which was also indicative of the honeycomb's strain rate sensitivity since in the quasi-static test condition (Chapter 2), volumetric energy absorption (U_v) was equal between materials. The lower volumetric energy absorption (U_v) achieved by the honeycomb samples compared to foam despite the increased compressive peak stress (σ_p) was due to the lesser degree of deformation experienced by the honeycomb samples.

In angled impact tests on the honeycomb samples, shear peak stress (τ_p) was significantly lower than compressive peak stress (σ_p), indicating the structure is anisotropic, as expected [61], and desired for TBI protection. Since densification during impact is not a consideration under shear loading, lower strength is beneficial to achieve sufficient deformation to mitigate rotational head kinematics. On the other hand, shear peak stress (τ_p) was significantly higher than compressive peak stress (σ_p) for EPS foam. This result was unexpected since EPS is isotropic [61]; however, it emphasizes the limitations of EPS foam for head protection and the benefits of honeycomb as a replacement.

Similar to the flat platen tests, the compressive peak stress (σ_p) was significantly higher for honeycomb compared to EPS foam in angled platen tests. There were no differences in shear peak stress (τ_p) between honeycomb and EPS foam, which indicated they would perform similarly for TBI protection, and reducing the strength of the honeycomb design to account for the strain rate dependence would likely make the honeycomb superior for TBI protection.

A limitation of this study is that volumetric energy absorption (U_v) could not be calculated in the angled impact scenario because the platen and impactor were not exactly parallel. To attain this outcome in future tests, the platen would need to be capable of precise adjustments. However,

the current test setup still achieved combined loading and allowed compressive peak stress (σ_p) and shear peak stress (τ_p) measurements, which gave meaningful results.

There were no differences in compressive peak stress (σ_p), shear peak stress (τ_p), or volumetric energy absorption (U_v) in repeated compared to initial impacts on honeycomb in both flat and angled testing scenarios. This suggested the design would be reusable for multiple impacts without requiring replacement – a novel contribution for bicycle helmet technology. Compressive peak stress (σ_p) for EPS foam were not different among repetitions in the flat platen impact scenario; however, the effect was in the direction of increasing compressive peak stress (σ_p) and this may have been detected with a larger sample size. Volumetric energy absorption (U_v) for EPS foam were also not significantly different among repetitions. The effect was in the direction of increasing volumetric energy absorption (U_v) but it is important to note that the volume was adjusted for the reduced thickness of the sample following each test. For angled platen tests, compressive peak stress (σ_p) and shear peak stress (τ_p) increased significantly among impact replications due to plastic deformation in the form of crack propagation, highlighting the need to replace traditional bicycle helmets following an accident.

The behaviours of honeycomb and EPS foam were explored under dynamic pure compressive and combined loading scenarios. The findings of this study suggest that honeycomb would be beneficial for bicycle helmets in comparison to EPS foam, due to its anisotropy that may allow sufficient deformation in the shear loading direction. However, the strain rate sensitivity of the design was also highlighted and suggested the need for further design modifications. This would involve reducing the relative density ($\bar{\rho}$) of the honeycomb systematically to achieve the design objectives outlined in Chapter 2, but under real-world dynamic impact conditions.

Chapter 4 – Full-Scale Helmet Design and Manufacturing

Overview: In this chapter, the strain rate sensitivity of the honeycomb design was quantified, and this was used to scale the design for protection in dynamic impact conditions. The honeycomb design was incorporated into the geometry of a full-scale helmet using Voronoi tessellation. Helmet prototypes were 3D-printed, and a suggested test method was presented to evaluate the full-scale helmet in comparison to existing bicycle helmets.

4.1   Introduction

Traditional EPS foam helmets effectively reduce the risk of skull fracture and severe traumatic brain injury (TBI) but not diffuse TBI (Section 1.3), which is primarily caused by the rotational motion of the head from the tangential force component of an impact. Hexagonal honeycomb could be a suitable replacement for expanded polystyrene (EPS) foam and could be made from an elastomeric material with the potential to be recoverable, and therefore effective for repeated impacts without requiring replacement.

Helmets in Canada must meet certain impact attenuation requirements defined by the Consumer Product Safety Commission (CPSC), where full-scale helmets are attached to an anthropomorphic test device (ATD) head and undergo drop tower impact tests onto a rigid platen (Section 1.6). Advanced testing methods also involve full-scale helmets evaluated through drop tower impact testing using an ATD head and neck, where linear and rotational kinematics of the headform are measured [60, 71, 75]. As such, new helmet designs must be manufactured as full-

scale prototypes to evaluate their effectiveness in preventing injury and make comparisons to existing helmets.

The focus of Chapter 2 and Chapter 3 was on the honeycomb structure itself, simplified in the form of small, flat samples. From this work, one specific honeycomb design was chosen, and then dynamic impacts were performed on this design. In incorporating these results into the design of a full-scale helmet, the curvature of the surface adds complexity, as hexagonal honeycomb cannot conform to a curved surface without modification [61]. The incorporation of 5-7 defects, which are seen in beeswax honeycomb, is an option to overcome this challenge without introducing any discontinuities in the architecture [91, 97]. To incorporate these 5-7 defects into engineered honeycomb, previous work has used Voronoi tessellation [92], where a set of seed points are generated, and from each point, a polygon grows outward until neighboring shapes begin to encroach.

Manufacturing the complex geometry of a honeycomb bicycle helmet would likely be unachievable by traditional subtractive manufacturing techniques. However, additive manufacturing (3-D printing) can allow the manufacturing of complex geometries and is also beneficial for creating small batches of design iterations (prototyping). Fused deposition modeling (FDM) is a type of 3D-printing, where plastic is melted and deposited in a specified pattern, layer-by-layer onto a build platform. A variety of solid materials (filaments) can be used with FDM 3D-printing, including elastomers such as thermoplastic polyurethane (TPU). Manufacturing a honeycomb helmet with TPU would mean that following the deformation of the structure it could potentially restore its original shape and mechanical properties [61], allowing it to be reusable.

A helmet design has been proposed that is made of honeycomb with 5-7 defects to accommodate the curvature of the human head, 3D-printed with TPU. The next step in evaluating

88

the honeycomb design was to incorporate the results based on small samples into the form of a full-scale helmet, to be used in future drop tower impact tests. Therefore, the goals of this Chapter were to design and manufacture full-scale helmet prototypes. The results of quasi-static and dynamic testing were used in conjunction to determine the most suitable honeycomb design according to the objectives defined in Chapter 2, but for dynamic impact conditions that would be seen in real-world bicycle accidents. The chosen honeycomb design was incorporated into a model of the helmet, which was then 3D-printed.

4.2   Honeycomb Design

A honeycomb design most suitable for head protection in dynamic impact conditions was found by comparing peak stress (σ_p) results among quasi-static compression testing (Chapter 2) and dynamic flat platen impact testing (Chapter 3), for one honeycomb design with constant $\bar{\rho}$ among test conditions. The average relative density ($\bar{\rho}$) of the honeycomb samples used for this analysis was $16.24 \pm 0.86\%$ and there were no statistical differences in relative density ($\bar{\rho}$) between test conditions. Compressive peak stress (σ_p) increased by 130% from the quasi-static condition to the 4.80 m/s condition (p = 0.0005) and 24% from the 4.8 m/s condition to the 5.76 m/s condition (p = 0.09) (Figure 4.1 and Table 4.). This indicated rate sensitivity and the need to tweak the parameters of the honeycomb design to be suitable for dynamic test conditions. In comparison, compressive peak stress (σ_p) was constant for EPS foam under quasi-static versus dynamic conditions (p = 0.5) (Figure 4.1 and Table 4.).
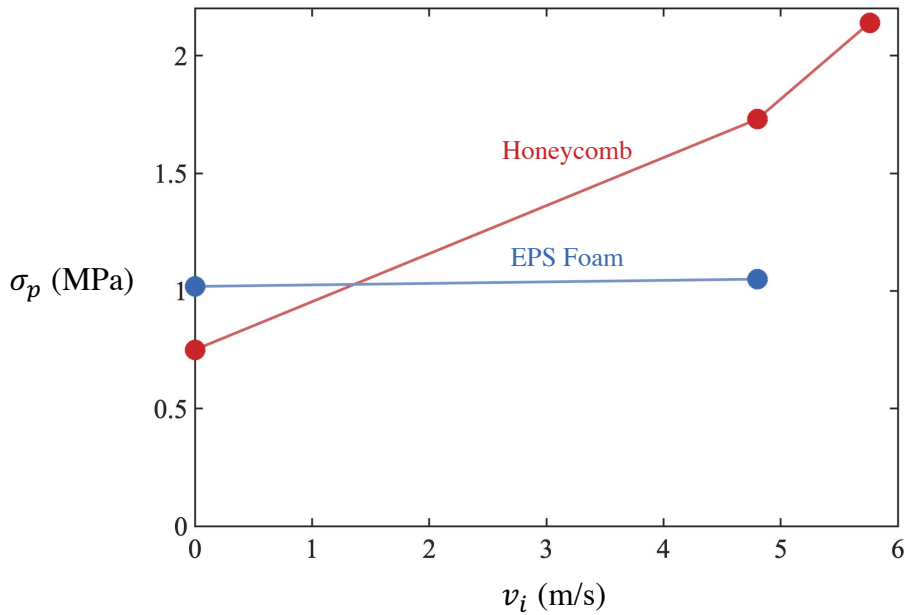
Figure 4.1: σ_p with Respect to v_i for Honeycomb and EPS Foam
σ_p is shown with respect to v_i, illustrating the effect of rate on honeycomb (red) and EPS foam (blue).

In quantifying the rate sensitivity of honeycomb, the relationship between compressive peak stress (σ_p) and relative density ($\bar{\rho}$) was assumed to follow the same trend for all impact velocities but scaled according to the strain rate sensitivity of the honeycomb. The strength of foams and lattice structures have been shown to scale with relative density as a power function [100][101], therefore this is given by Equation 4.1, where $\sigma_{p(dynamic)}$ is dynamic peak stress, $\sigma_{p(static)}$ is static peak stress, K is the scaling factor, and A and b are constants in the power regression.

The scaling factor (K) was defined as the ratio of dynamic peak stress ($\sigma_{p(dynamic)}$) to quasi-static peak stress ($\sigma_{p(static)}$) for a constant known relative density (Equation 4.2).

$$\sigma_{dynamic} = K\sigma_{static} = KA\bar{\rho}^b \qquad\qquad \textbf{Equation 4.1}$$

$$K = \frac{\sigma_{p(dynamic)}}{\sigma_{p(static)}}$$ **Equation 4.2**

A scaling factor (K) was determined for honeycomb with an average relative density ($\bar{\rho}$) of 16.24% under each dynamic condition (Table 4.), where the scaling factor (K) increased with increasing impact velocity (v_i). Using the calculated scaling factor values (K), relationships between compressive peak stress (σ_p) and relative density ($\bar{\rho}$) were predicted for each impact velocity (v_i) (Figure 4.2).

Table 4.1: σ_p for Flat Platen Tests on Honeycomb with Different Impact Velocities
A summary of average σ_p results is shown for flat platen quasi-static and dynamic tests on honeycomb from Chapter 2 and Chapter 3 with calculated values for the scaling factor (K). v_i is the impact velocity and N is the number of samples.

v_i (m/s)	N	Average σ_p (MPa)	K
2.5×10^{-5}	4	0.750 ± 0.03	-
4.80 ± 0.05	3	1.73 ± 0.25	2.3
5.76 ± 0.04	3	2.14 ± 0.20	2.85

Table 4.2: σ_p for Flat Platen Tests on EPS Foam with Different Impact Velocities
A summary of average σ_p results is shown for flat platen quasi-static and dynamic tests on EPS foam with percent difference and p-value from the quasi-static condition. v_i is the impact velocity and N is the number of samples. Percent difference and p-value compared to the quasi-static condition (2.5×10^{-5} m/s) are presented.

v_i (m/s)	N	Average σ_p (MPa)	% difference	p-value
2.5×10^{-5}	3	1.019 ± 0.05	-	-
4.80 ± 0.05	3	1.05 ± 0.07	3.15%	0.5
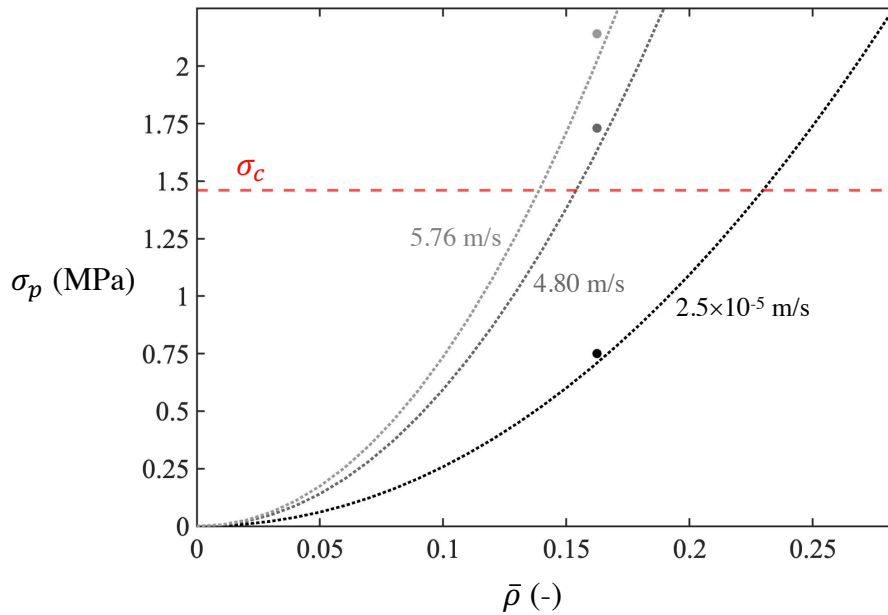
Figure 4.2: Power Regression Functions for σ_p with Respect to $\bar{\rho}$
The power regression relationship for σ_p with respect to $\bar{\rho}$ is shown from the results of quasi-static compression tests. Predicted relationships for the 4.80 m/s and 5.76 m/s impact conditions are also shown for comparison. Experimental data points for $\bar{\rho}$ of 16% are included.

Results from quasi-static compression testing (Chapter 2) suggested that the relationship between compressive peak stress (σ_p) and relative density ($\bar{\rho}$) could be represented by Equation 4.3, where the coefficient depends on the geometry of the cellular structure and the exponent depends on the deformation mechanism (a value of two indicates bending-dominated deformation) [100][101].

$$\sigma_{p(static)} = 31.2\bar{\rho}^{2.1} \qquad \qquad \textbf{Equation 4.3}$$

A new desired relative density ($\bar{\rho}$) was determined by first finding the static peak stress ($\sigma_{p(static)}$) that corresponded to a relative density ($\bar{\rho}$) of 17%, which was determined to be the most suitable relative density ($\bar{\rho}$) in quasi-static conditions (Chapter 2). Using Equation 4.3, the predicted peak stress was 0.78 MPa. A relative density ($\bar{\rho}$) of 11.4% was found to correspond to

0.78 MPa for a impact velocity (v_i) of 4.80 m/s, using the predicted relationship between dynamic peak stress ($\sigma_{p(dynamic)}$) and relative density ($\bar{\rho}$). To ensure the skull fracture threshold (1.46 MPa) would not be exceeded in other impact conditions, dynamic peak stress ($\sigma_{p(dynamic)}$) was calculated for the high-velocity condition. This resulted in a predicted value of 1.06 MPa for a relative density ($\bar{\rho}$) of 11.4% and impact velocity (v_i) of 5.76 m/s, which did not exceed the skull fracture threshold.

4.3　Full-Scale Helmet Modelling and Prototyping

For the design of a full-scale honeycomb helmet prototype, the shape was based on a Seven Star Sports (Hamilton, Ontario, Canada) multi-sport helmet (Figure 4.3). The helmet consisted of an EPS foam layer, an outer polyvinyl chloride (PVC) shell (Figure 4.4a), a retention system (Figure 4.4b), a strap (Figure 4.4c), and comfort padding. It was essential to replicate the shape of this existing EPS foam helmet to use its components for the honeycomb helmet assembly.
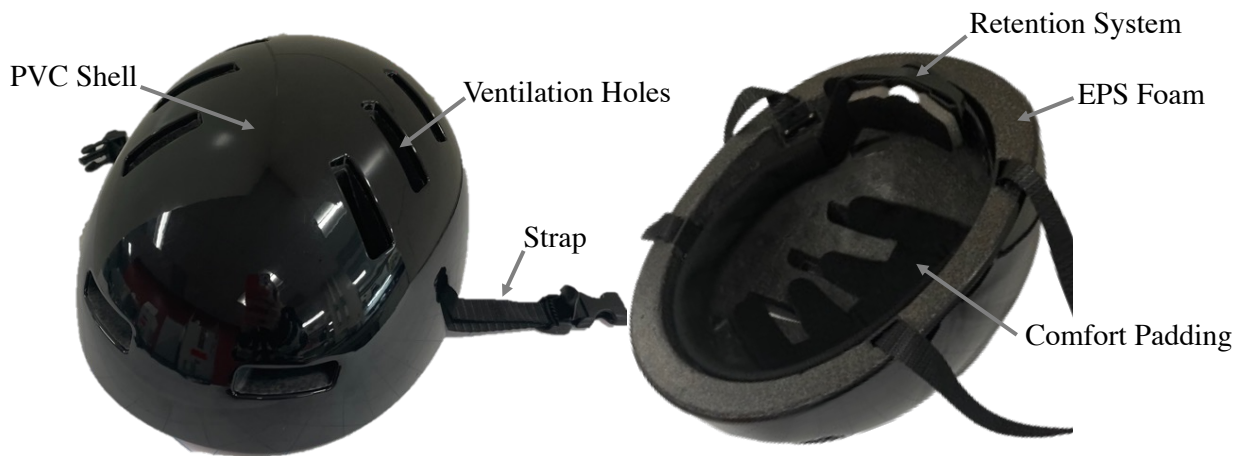
Figure 4.3: Seven-Star Multi-Sport Helmet
The Seven-Star multi-sport helmet consists of an EPS foam layer, PVC shell, retention system, strap, and comfort padding.

a)

b)   c)
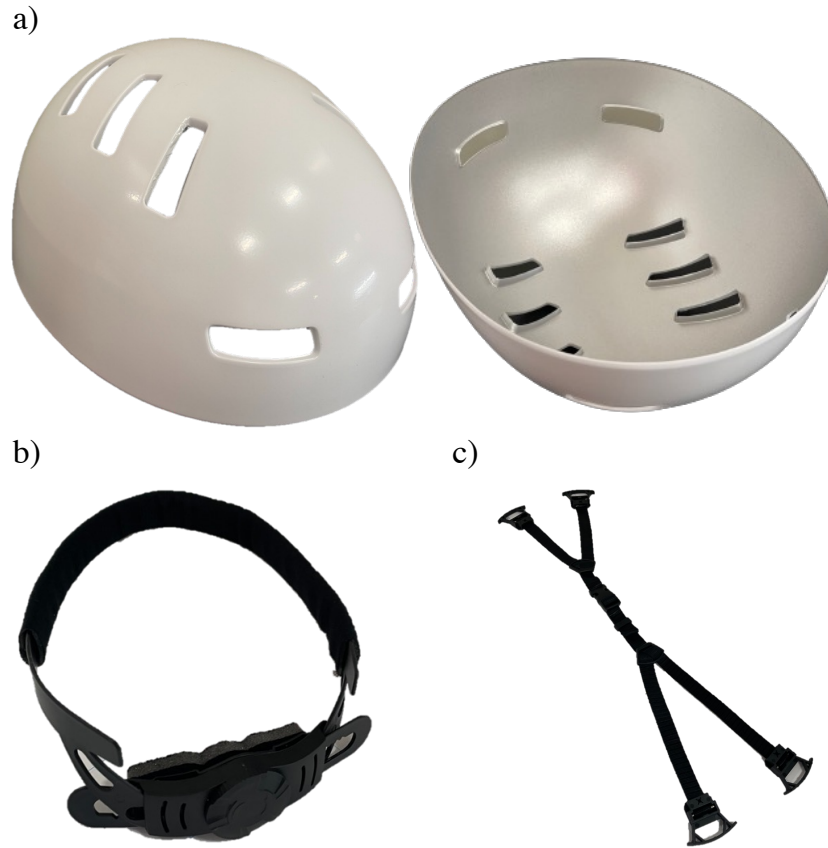
Figure 4.4: Components of an Assembled Helmet
The components of a Seven-Star multisport helmet include a) a PVC shell, b) a retention system, and c) a strap. These components would be included in the assembly of a full-scale honeycomb helmet.

In incorporating the final honeycomb design into the geometry of a full-scale helmet, first, a CAD model of the multi-sport helmet shape was received from Seven Star Sports. The helmet shape contained notches for attachment of the straps and ventilation holes for the comfort of the rider. The CAD model was uploaded to Autodesk Inventor (San Francisco, California, USA), and simplified by deleting ventilation holes, decals, and unwanted surfaces (Figure 4.5).

Figure 4.5: Model of Helmet Shape
A model of a helmet was simplified to remove unwanted geometry yet retain strap attachment points.

This helmet model was imported to nTopology (New York, USA). The outer helmet surface was extracted, and a set of 1000 random points was generated on the surface. Relaxation iterations were performed to ensure the points were as evenly spaced as possible. The number of points dictated the number of honeycomb cells and therefore the size of the honeycomb cells, which was 6 mm to match the cell size of the flat honeycomb models used for testing in Chapter 2 and Chapter 3. To create a honeycomb pattern on the outer surface of the helmet, a Voronoi boundary lattice was generated from the set of random points. In using this method, the 5-7 defects were randomly distributed throughout the helmet. The surface lattice was extruded into a 3D honeycomb structure and the cell walls were then thickened to 0.91 mm to achieve the desired relative density ($\bar{\rho}$) of 11.4% (Figure 4.6). A brim was made on the bottom surface of the helmet (perpendicular to the surface of the head) to close in the incomplete honeycomb cells, by extracting the bottom surface from the original helmet shape and thickening this to 1 mm. The honeycomb

and brim were joined, and a mesh was generated and then refined to improve the size, shape, and uniformity of the mesh elements.

Figure 4.6: Model of Full-Scale Honeycomb Helmet
a) Isometric view, b) side view, c) top view, and d) bottom view of the full-scale honeycomb helmet model.

A Raise3D (Irvine, California, USA) Fused Deposition Modelling (FDM) 3D-printer was used to manufacture prototypes of the full-scale honeycomb helmet (N=5) (Figure 4.7). Flexfill TPU (Fillamentum Addictive Polymers, Hulín, Czech Republic) filament was used, which has a density of 1.23 g/cm^3, a tensile strength of 53.7 MPa, a hardness of 98 shore A and an elongation at break of 318%. The helmet was printed with the brim flat on the print bed, and with a support structure in the centre-most part of the helmet to support areas with large overhangs or bridging

(Figure 4.8), which were removed after printing was complete. The dimensions of the 3D-printed

helmets were consistent with the CAD model. The average mass of the helmets was 339 ± 7 g.
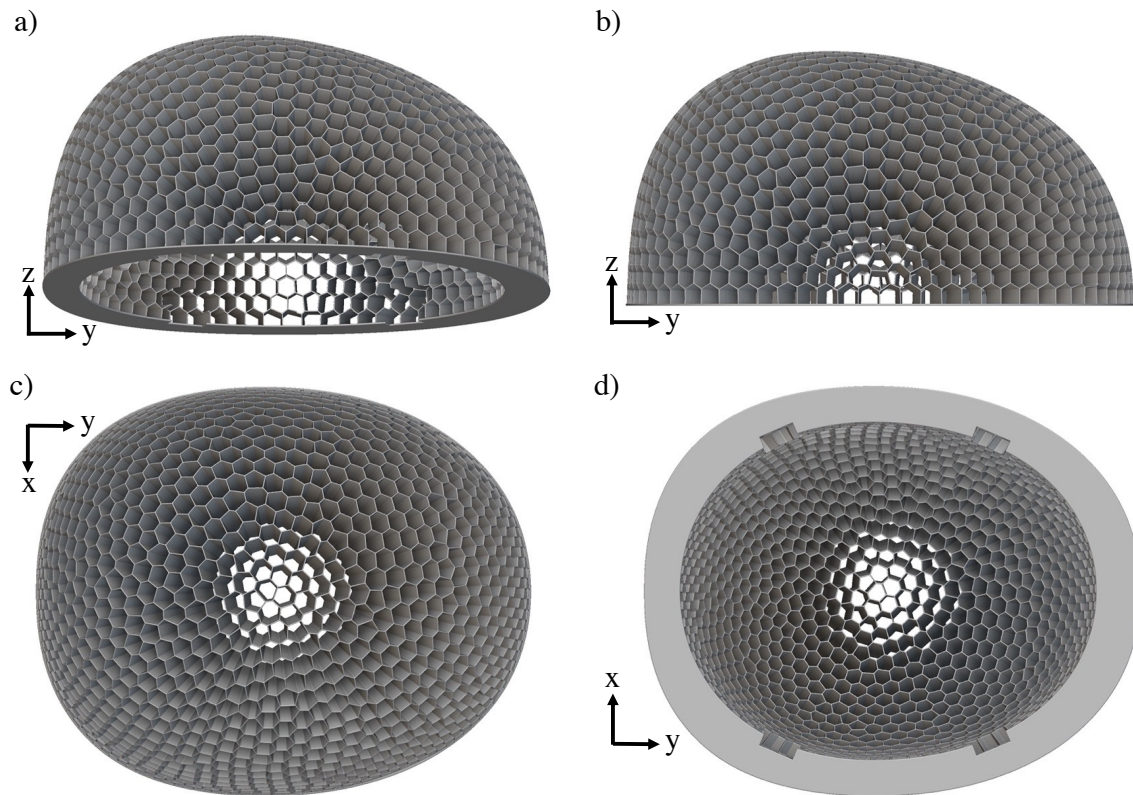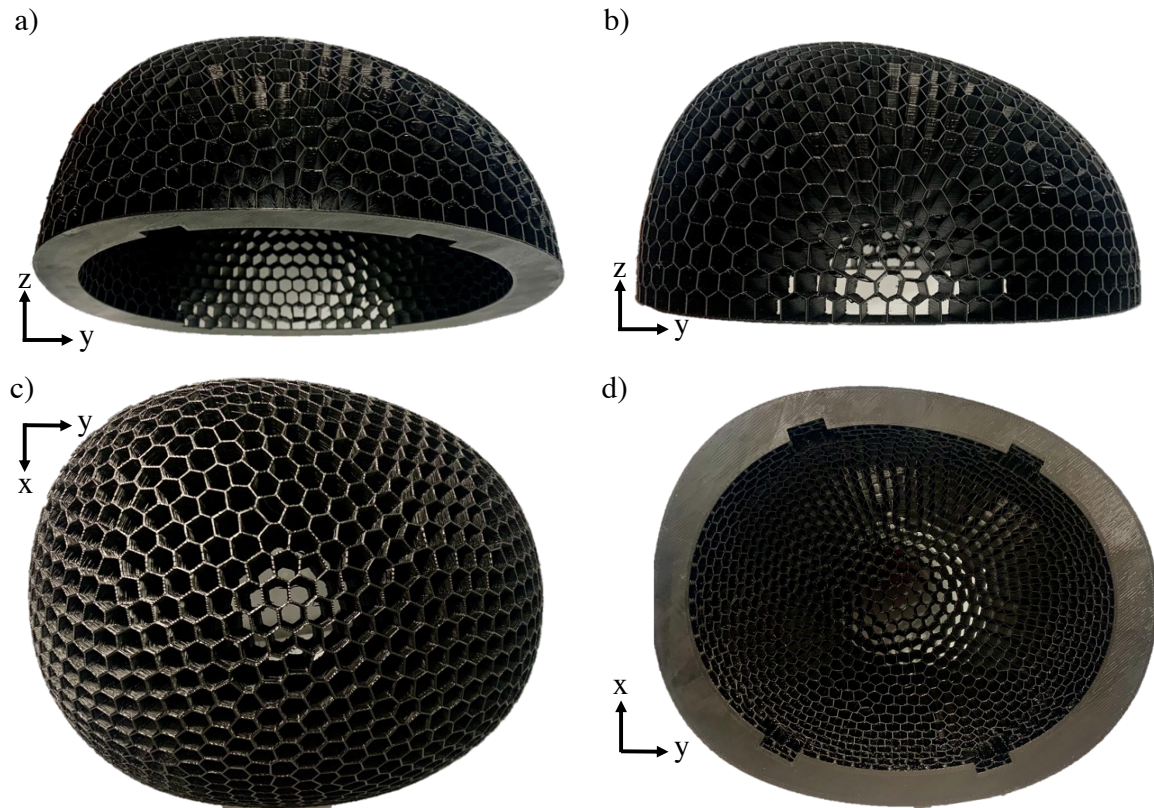

Figure 4.7: 3D-Printed Full-Scale Honeycomb Helmet
a) Isometric view, b) side view, c) top view, and d) bottom view of the full-scale helmet
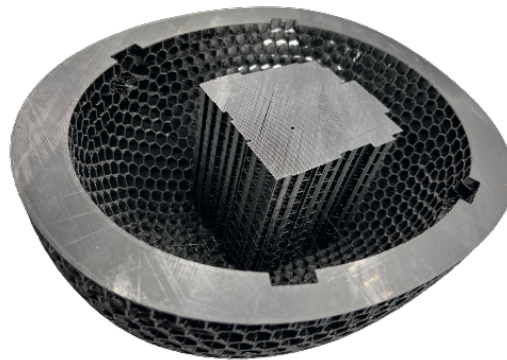prototype.

Figure 4.8: Honeycomb Helmet with Supports
The honeycomb helmet was 3D-printed with a support structure in the centre-most part of the
helmet to support areas with large overhangs or bridging.

4.4   Discussion

The results of quasi-static and dynamic testing were used to determine the most suitable honeycomb design for head protection and this design was applied to the geometry of a full-scale helmet model, which was 3D-printed with TPU. There was a significant effect of impact velocity on the desired relative density of the honeycomb and scaling the design to accommodate this was essential in not exceeding the injury threshold for skull fracture.

In this study, impact velocity effects were only considered in the normal loading direction – it was assumed that strain rate would have a similar effect in pure shear loading and combined loading scenarios. With the objective in this loading direction of minimizing shear modulus (G), lowering the relative density ($\bar{\rho}$) would benefit the outcome in terms of TBI protection.

In terms of helmet modeling, it was important for the shape and size to be consistent with existing EPS foam helmets to use its components for the honeycomb helmet assembly and for direct comparisons between honeycomb and EPS foam in future helmet testing (Section 4.4.1). By using a model of an existing helmet, the shape, size, and other helmet components were controlled, therefore any differences seen in helmet testing would be attributed to the honeycomb component. The position of 5-7 defects was random in the honeycomb helmet model. Although this method was effective at allowing the helmet to conform to the curvature of the head, in future design iterations, the position of 5-7 defects could be specified in a way that is beneficial for head protection, as determined through further small-sample testing.

In terms of helmet manufacturing, Flexfill TPU filament was used for 3D-printing due to its compatibility with the Raise3D printer, whereas NinjaTek Cheetah TPU filament was used for the honeycomb samples in Chapter 2 and Chapter 3. The material properties of NinjaTek Cheetah

differ slightly from those of Flexfill, where Cheetah has a density of 1.22 g/cm³ (compared to 1.23 g/cm³), a tensile strength of 39 MPa (27% lower than Flexfill), a hardness of 95 Shore A (compared to 98 Shore A), and an elongation at break of 580% (compared to 318%). With the difference in strength and hardness, the honeycomb in the full-scale helmet would likely have a higher compressive peak stress (σ_p) and volumetric energy absorption (U_v), and in future design iterations, the relative density ($\bar{\rho}$) of the honeycomb could be scaled down accordingly.

In this study, FDM printing was used since it had the lowest cost and was sufficient for proof-of-concept prototyping. However, FDM is not ideal for printing complex geometries because of the low resolution and accuracy and the need for support structures. Future iterations of the design should be 3D-printed with the Selective Laser Sintering (SLS) process, where a laser fuses together polymer powder. SLS printing is ideal for functional prototyping and end-use parts, with a low print time, high resolution and accuracy, and no need for support structures. Also, with FDM printing, the orientation of the print may affect the mechanical properties, therefore the properties of the honeycomb could vary in different areas on the head – this would be less of a consideration with SLS 3D-printing.

4.4.1 Recommended Future Testing

To evaluate the full-scale honeycomb helmet design, drop tower impact testing should be performed. The effectiveness of the honeycomb helmet design would be compared to commercially available EPS foam helmets that would be identical in terms of size, shape, shell material, retention system, and comfort padding. The only part of the helmets that would differ is the honeycomb versus EPS foam layer, therefore any differences in results would be attributed to this component.

The test setup would consist of a Hybrid III 50th percentile male head-and-neck Anthropomorphic Test Device (ATD) mounted to a National Operating Committee on Standards for Athletic Equipment (NOCSAE) carriage. The headform would be covered in nylon stockings to mimic hair friction. The carriage together with the impactor should weigh 14.0 kg, to represent the mass of the human head and include the effective torso mass in a head-first impact [102], and to be consistent with previous studies [60, 71, 75]. The carriage would be guided by two vertical wires and the ATD head would impact a steel platen, covered with 80-grit sandpaper to mimic a real-world impact surface. Two different impact scenarios would be tested:

i.   Horizontal impact platen

ii.   Angled impact platen (45° from the horizontal)

In the first impact scenario (i.), results could be compared to CPSC impact testing standards. The second impact scenario (ii.) is more representative of real-world head impacts in bicycle accidents, which typically occur at angles of 30° to 60° with respect to the horizontal impact surface [22–24]. For both scenarios, an impact velocity of 4.8 m/s would be targeted to represent real-world accidents and consistent with previous studies [60, 71, 75]. An impact location on the front of the head would be targeted since this is the most commonly impacted region according to an analysis of helmets following real-world bicycle accidents [103]. The Hybrid III ATD headform would be instrumented with a 6-axis accelerometer to measure the linear and rotational kinematics of the headform. A high-speed camera would be used to calculate the impact velocity. The main kinematic outcomes would be:

- Peak resultant linear acceleration

- Peak y-axis rotational acceleration (sagittal plane)

- Peak y-axis rotational velocity (sagittal plane)

The probability of sustaining TBI in each impact would be predicted based on the Brain Injury Criteria (BrIC) and Universal Brain Injury Criteria (UBrIC) (outlined in Section 1.4.4) for rotation in the sagittal plane. Kinematic response, BrIC, and UBrIC would be compared to the outcomes for EPS foam helmets to determine the effectiveness of the honeycomb helmet design for skull fracture and TBI protection.

4.4.2   Conclusions

The relative density ($\bar{\rho}$) of the honeycomb for a full-scale honeycomb helmet was determined according to the results of quasi-static and dynamic testing to be suitable in dynamic impact conditions. These results were incorporated into a full-scale helmet model, which was manufactured using FDM 3D-printing, where the shape, size, and other helmet components (shell, retention system, and strap) were consistent with an EPS foam helmet. This is an important step towards the potential implementation of the honeycomb bicycle helmet as a protective device and has incorporated methods to address the unique challenges of modeling and manufacturing curved honeycomb for head protection. The next step in evaluating the honeycomb helmet design would be to perform oblique drop tower impact testing as outlined above.

Chapter 5 – General Discussion and Conclusions

Overview: *This chapter reviews the study objectives that were established in Chapter 1, by summarizing the main outcomes from each component and their importance to the development of the honeycomb helmet design. Overall strengths and limitations of the thesis are presented, and future directions are proposed for helmet design and testing.*

5.1 Summary

Bicycling is a popular activity around the world and a frequent source of head injury, including skull fracture, facial fracture, and traumatic brain injury (TBI). Traditional expanded polystyrene (EPS) foam helmets effectively reduce the risk of fractures and severe TBI; however, there is no scientific evidence that EPS foam helmets reduce the risk of diffuse TBI, such as concussion (Section 1.3). The overall purpose of the studies presented in this thesis was to develop a helmet design that improves the head protection offered by current helmets in bicycle accidents. A helmet design was proposed that is made of 3D-printed hexagonal honeycomb with 5-7 defects.

Since this was a novel approach to bicycle helmet design, the properties of small, flat honeycomb samples were first explored, where 3D-printing was employed for rapid prototyping (Chapter 2). Accommodating the curvature of the head requires the inclusion of 5-7 defects, therefore two arrangements were tested under quasi-static compression and shown to decrease the strength of the honeycomb. A relative density ($\bar{\rho}$) most suitable for head protection was determined based on the results of quasi-static compression and shear testing, primarily relevant to skull

fracture and diffuse TBI protection, respectively. The design objectives were to meet a minimum energy absorption requirement (U_v), for the strength of the honeycomb (σ_p) to remain below the skull fracture threshold, and to minimize shear modulus (G) (and subsequently minimize rotational head motion for diffuse TBI protection). A design most suitable for head protection was chosen, and strain rate was found to influence the mechanical properties of the honeycomb.

Since helmet certification and real-world bicycle accidents occur at higher rates, and strain rate sensitivity was highlighted in mechanical testing, dynamic drop tower impact tests were then performed on the chosen honeycomb design (Chapter 3). Various impact scenarios were explored with two velocities representative of real-world bicycle accidents, and two orientations including purely linear (where the impactor and platen were horizontal) and oblique (where the impactor and platen angled at 45° from the horizontal). The strength of the honeycomb (σ_p) increased with impact velocity, highlighting the need to scale the design for dynamic impact conditions. Honeycomb shear strength (τ_p) was significantly lower than compressive strength (σ_p), indicating its anisotropy, which is beneficial for diffuse TBI protection. Performing repeated impacts on the honeycomb design did not affect the mechanical properties, indicating the helmet's potential to be reused for multiple impact events. The results of this dynamic testing suggested that honeycomb would be beneficial for bicycle helmets in comparison to EPS foam.

The above quasi-static and dynamic testing culminated in the design of a full-scale honeycomb helmet (Chapter 4). The rate sensitivity of the honeycomb was quantified, and the design was scaled to be suitable for dynamic impact conditions. The chosen honeycomb design was incorporated into the geometry of a full-scale helmet, where Voronoi tessellation was used for including 5-7 defects in the geometry. Five helmet prototypes were 3D-printed using fused

deposition modeling (FDM) with thermoplastic polyurethane (TPU). A suggested test method was presented to evaluate the honeycomb helmet design.

5.2   Strengths and Limitations

Specific strengths and limitations of each component of this research were discussed in each chapter; however, there are general strengths and limitations applicable to the entire thesis. A honeycomb helmet design was proposed, and various design parameters were investigated, including relative density and the presence of 5-7 defects. The effectiveness of the design was comprehensively explored in many impact scenarios involving different impact velocities and angles. The design showed potential improvement compared to EPS foam helmets, in small-scale quasi-static and dynamic testing scenarios. An effective method of applying the developed honeycomb design to a full-scale helmet was demonstrated, where the design omits EPS foam altogether, unlike MIPS and WaveCel helmets; and no discontinuities exist within the honeycomb, unlike HEXR helmets. It is expected that the full-scale honeycomb helmet would reduce the rotational motion of the head real-world impacts compared to current helmets and subsequently provide improved protection against TBI. The proposed design also showed potential to be reusable and provide protection for multiple impact events, unlike any commercially available helmets.

Small, flat honeycomb samples were used for quasi-static and dynamic testing, which may not have given identical results to the mechanical properties of a full-scale helmet with curvature. However, this simplification was reasonable for assessing head protection, and the results would be representative of the loading that would occur at the point of highest curvature. Using small, flat honeycomb samples was beneficial in that mechanical properties could be defined, many

104

samples could be 3D-printed with various design alterations, and many testing scenarios could be explored. As well, the size of the samples was chosen according to the typical effective contact area in a real-world head impact.

The design of the honeycomb helmet was based on the results of quasi-static testing and then scaled for dynamic impacts, which was not representative of the loading conditions in real-world bicycle accidents. As a limitation of experimental testing, the design was not directly optimized in a dynamic testing scenario. FEA is a tool that would allow that to be investigated, and the model could be validated against the data presented herein. However, the response of one honeycomb design was explored under dynamic loading conditions representative of real-world bicycle accidents and compared to the response of EPS foam (Chapter 3). The honeycomb design was also scaled according to the determined strain rate sensitivity and designed specifically for an impact velocity in the range seen in bicycle accidents. Although only one design was tested in the dynamic, combined compressive-and-shear loading scenario, exploring the honeycomb response to impact on a small scale was a strength of this work. With this, the honeycomb design could be compared to EPS foam and changes to the design could be made prior to full-scale helmet prototyping.

A further strength of this work was that design objectives were defined directly based on the mechanisms of various head injuries including skull fracture and TBI. These injury mechanisms were related to the mechanical properties of the helmet and the test setups were designed to obtain these primary outcomes. As well, 3D-printing was employed for rapid prototyping for all components of this research, which was beneficial for allowing complex designs, manufacturing samples on demand, minimizing waste compared to subtractive manufacturing methods, and minimizing cost for small-batch manufacturing.

Although the focus of this work was specific to bicycle helmets, many components may have use in future research. For example, the properties of elastomeric honeycomb were defined under shear loading – a new contribution to the literature. As well, the design concept may be relevant to other impact attenuation/energy absorption applications, especially those involving curvature.

5.3   Future Directions

5.3.1   Honeycomb Helmet Design

This work presented the preliminary design of a honeycomb bicycle helmet to protect against both skull fracture and TBI. Thus far, the concept of using a honeycomb structure for energy absorption has been introduced, 5-7 defects have been implemented to allow a continuous honeycomb design to cover the curvature of the human head, an elastomeric material has been chosen to allow for potential reusability of the design, and a relative density ($\bar{\rho}$) most suitable for head protection has been determined. Many future directions could be taken in developing iterations of the honeycomb helmet design.

The honeycomb samples that were explored in Chapter 2 included regular honeycomb, honeycomb with 'stacked' 5-7 defects, and honeycomb with 'staggered' 5-7 defects. Future work could consider the effect of multiple defect 'boundaries' on the mechanical properties, where two or more columns of 'stacked' or 'staggered' 5-7 defects would be placed within the hexagonal domain. These results could then be applied to the full-scale helmet by specifying the position of 5-7 defects in a way that is beneficial for head protection.

In future design iterations, 3D-printing could offer the potential to introduce a relative density 'gradient', where the strength of the honeycomb would be lower closer to the head, and higher at the outer surface. The objective of this design feature would be to prevent bottoming out of the helmet with the high-strength layer while allowing even more shear deformation in the low-strength layer to further reduce the rotational kinematics of the head following impact.

Another future design step could be to add creases in the honeycomb cell walls, parallel to the surface of the head. This would encourage the honeycomb walls to collapse under compressive loading, to reduce peak compressive stress (σ_p), without affecting the plateau stress. As outlined in Section 2.2, the design objectives for compressive loading were to have sufficient volumetric energy absorption (U_v), while peak stress (σ_p) remains below the injury threshold for skull fracture. With this design feature, volumetric energy absorption (U_v) is expected to be greater for identical peak stress(σ_p), improving the energy absorption efficiency of the honeycomb.

The orientation in which the honeycomb structure is fused deposition modeling (FDM) 3D-printed may affect the mechanical properties. Due to the curved geometry of the helmet, this means the mechanical properties of the current helmet design would vary between locations on the head. A suggested next step would be to quantify this difference in mechanical properties. If the difference is significant, then a multi-axis FDM 3D-printer should be used in future design iterations to allow the print orientation of the honeycomb to be consistent across the entire helmet. Alternatively, a different 3D-printing method, such as Selective Laser Sintering (SLS) could be used. 3D-printing is beneficial for developing prototypes; however, for future full-scale manufacturing of the honeycomb helmets, the injection molding process would be more time and cost effective.

As outlined in Section 2.2, the design objectives included ensuring the peak stress (σ_p) did not exceed the injury threshold for skull fracture. However, injury thresholds vary with factors like age and sex. Therefore, a future direction would be to design helmets specifically for different populations, for example, youth. This would likely involve reducing the strength of the honeycomb by reducing relative density ($\bar{\rho}$).

The reusability of the helmet was explored through quasi-static testing and small-scale dynamic drop tower impacts; however, the lifecycle/durability of the design would need to be quantified in future work. Further, a visual indication of whether the helmet is suitable for continued use would be necessary. For example, flexible pressure-sensor films could be attached to the helmet that changes colour according to the amount of force experienced in a single impact or the cumulative amount of force experienced by the helmet.

Although honeycomb is generally beneficial in terms of its strength-to-mass ratio, the mass of the helmet was not considered in the design process. For practical use of the helmet, future iterations of the design could be optimized to reduce mass while providing sufficient energy absorption capability.

5.3.2   Testing

In this work, quasi-static and dynamic testing was performed on flat honeycomb and EPS foam samples. For the preliminary design of the honeycomb helmet, these testing methods were appropriate; however additional considerations could be made in future work.

The design objectives defined in Chapter 2 were not specific to using an elastomeric material for the honeycomb design. Future work should consider the elastic rebound of the honeycomb, where under both compressive and shear loading, the honeycomb structure would

undergo elastic deformation and store elastic potential energy. This elastic potential energy would be translated to the head as kinetic energy when the honeycomb restores to its original position. Consideration should be made to ensure this kinetic energy does not have the potential to cause linear and rotational head kinematics at injurious levels.

Rather than scaling the design according to the strain rate sensitivity of the honeycomb, in future work, small-sample dynamic drop tower testing (Chapter 3) could be performed on samples with varying relative density ($\bar{\rho}$) and 5-7 defect arrangements to determine the most suitable design under these conditions. Alternatively, this could be done using FEA, which would reduce the number of 3D-printed samples required and allow the exploration of more test conditions, including a range of impact angles and velocities.

A test method was outlined for evaluating the full-scale helmet design (Chapter 4). The outcomes of this testing method would be linear and rotational head kinematics and from this, injury risk would be inferred and compared to that for EPS foam helmets. Future work could use these head kinematics as an input to a finite element model (FEM) of the human head, where resulting brain strain could be measured to predict injury risk more accurately.

5.4   Significance

In conclusion, this work presented a new helmet design that has the potential to reduce the risk of sustaining TBI in a bicycle accident, while also preventing skull fracture. TBIs are currently frequent in bicycle accidents, have long-term consequences on quality of life, and carry a substantial economic burden.

Current EPS foam helmets have substantial limitations for head protection and helmets with advanced helmet technology, such as MIPS, could still be improved upon. An innovative

solution was presented to address the gaps in head protection. The honeycomb helmet was designed specifically for real-world bicycle accident conditions and according to head injury mechanisms. The honeycomb helmet design could potentially further reduce the rotational motion of the head by providing sufficient deformation in the shear loading direction. A benefit to the honeycomb design is there are no disconnected cells like in HEXR helmets, to provide consistent mechanical properties across the head. As well, the honeycomb helmet design would likely be reusable for multiple impacts, which would have substantial benefits to consumers in further reducing injury risk, reducing cost, and reducing the environmental impact associated with helmet replacement following an accident. The reusable honeycomb helmet design presented would also have implications for other sports, especially those where multiple impact events can occur in one game, such as hockey and American football.

References

[1]   M. Hamer and Y. Chida, "Active commuting and cardiovascular risk: A meta-analytic review," *Preventive Medicine*, vol. 46, no. 1, pp. 9–13, Jan. 2008.

[2]   Centers for Disease Control and Prevention, "Bicycle helmet usage and head injury prevention," 2000. https://www.cdc.gov/program/performance/fy2000plan/ 2000xbicycle.htm.

[3]   G. M. Teasdale, "Head injury," *Neurosurgery and Psychiatry*, vol. 58, pp. 526–539, 1995.

[4]   D. Fife, J. Davis, L. Tate, J. K. Wells, D. Mohan and A. Williams, "Fatal injuries to bicyclists: the experience of Dade County, Florida.," *The Journal of Trauma*, vol. 23, no. 8, pp. 745–755, Aug. 1983.

[5]   T. Wood and P. Milne, "Head injuries to pedal cyclists and the promotion of helmet use in Victoria, Australia," *Accident Analysis and Prevention*, vol. 20, no. 3, pp. 177–185, 1988.

[6]   N. Persaud, E. Coleman, D. Zwolakowski, B. Lauwers and D. Cass, "Nonuse of bicycle helmets and risk of fatal head injury: a proportional mortality, case–control study," *Canadian Medical Association Journal*, vol. 184, no. 17, p. E921, Nov. 2012.

[7]   H. M. Bramlett and W. D. Dietrich, "Long-term consequences of traumatic brain injury: current status of potential mechanisms of injury and neurological outcomes," *Journal of Neurotrauma*, vol. 32, no. 23, pp. 1834–1848, Dec. 2015.

[8]   M. Faul, M. M. Wald, L. Xu and V. G. Coronado, "Traumatic brain injury in the United States: emergency department visits, hospitalizations, and deaths, 2002-2006." 2010.

[9]   V. G. Coronado, T. Haileyesus, T. A. Cheng, J. M. Bell, J. Haarbauer-Krupa, M. R. Lionbarger, J. Flores-Herrera, L. C. McGuire, and J. Gilchrist, "Trends in sports- and recreation-related traumatic brain injuries treated in US emergency departments: the National Electronic Injury Surveillance System-All Injury Program (NEISS-AIP) 2001-2012," *The Journal of head trauma rehabilitation*, vol. 30, no. 3, pp. 185–197, May 2015.

[10]   K. Sarmiento, T. Haileyesus, D. Waltzman, and J. Daugherty, "Emergency department visits for bicycle-related traumatic brain injuries among children and adults - United States, 2009-2018," *Centers for Disease Control and Prevention - Morbidity and Mortality Weekly Report*, vol. 70, no. 19, 2021.

[11]   K. B. Arbogast, A. E. Curry, M. R. Pfeiffer, M. R. Zonfrillo, J. Haarbauer-Krupa, M. J. Breiding, V. G. Coronado, and C. L. Master, "Point of health care entry for youth with

concussion within a large pediatric care network," *JAMA pediatrics*, vol. 170, no. 7, Jul. 2016.

[12] P. A. Cripton, D. M. Dressler, C. A. Stuart, C. R. Dennison and D. Richards, "Bicycle helmets are highly effective at preventing head injury during head impact: head-form accelerations and injury criteria for helmeted and unhelmeted impacts," *Accident Analysis and Prevention*, vol. 70, pp. 1–7, Sep. 2014.

[13] A. S. McIntosh, A. Lai and E. Schilter, "Bicycle helmets: head impact dynamics in helmeted and unhelmeted oblique impact tests," *Traffic Injury Prevention*, vol. 14, no. 5, pp. 501–508, Jul. 2013.

[14] E. J. Alfrey *et al.*, "Helmet usage reduces serious head injury without decreasing concussion after bicycle riders crash," *Journal of Surgical Research*, vol. 257, pp. 593–596, Jan. 2021.

[15] A. Gilroy, M. Voll and K. Wesker, *Anatomy: an essential textbook*, 3rd ed. New York: Thieme Medical Publishers, 2021.

[16] W. L. Nowinski, *Introduction to brain anatomy*. Biomechanics of the Brain, 2011.

[17] M. A. Patestas and L. P. Gartner, *A textbook of neuroanatomy*, 2nd ed. John Wiley & Sons, 2016.

[18] P. Schepers and K. Klein Wolt, "Single-bicycle crash types and characteristics," *Cycling Research International*, vol. 2, no. October, pp. 119–135, 2012.

[19] B. Depreitere, C. Van Lierde, S. Maene, C. Plets, J. Vander Sloten, R. Van Audekercke, G. Van der Perre, and J. Goffin, "Bicycle-related head injury: a study of 86 cases," *Accident Analysis and Prevention*, vol. 36, no. 4, pp. 561–567, 2004.

[20] S. Linn, D. Smith and S. Sheps, "Epidemiology of bicycle injury, head injury, and helmet use among children in British Columbia: a five year descriptive study. Canadian Hospitals Injury, Reporting and Prevention Program (CHIRPP)," *Injury prevention: journal of the International Society for Child and Adolescent Injury Prevention*, vol. 4, no. 2, pp. 122–125, Jun. 1998.

[21] J. Nie and J. Yang, "A study of bicyclist kinematics and injuries based on reconstruction of passenger car–bicycle accident in China," *Accident Analysis & Prevention*, vol. 71, pp. 50–59, Oct. 2014.

[22] N. Bourdet, C. Deck, T. Serre, C. Perrin, M. Llari and R. Willinger, "In-depth real-world bicycle accident reconstructions," *International Journal of Crashworthiness*, vol. 19, no. 3, pp. 222–232, May 2014.

[23] N. Bourdet, C. Deck, R. P. Carreira and R. Willinger, "Head impact conditions in the case of cyclist falls," *Proceedings of the Institution of Mechanical Engineers, Part P: Journal*

of Sports Engineering and Technology, vol. 226, no. 3–4, pp. 282–289, Sep. 2012.

[24]   D. Otte, "Injury mechanism and crash kinematic of cyclists in accidents - An analysis of real accidents," *SAE Technical Papers*, Oct. 1989.

[25]   A. H. S. Holbourn, "Mechanics of head injuries," *The Lancet*, vol. 242, no. 6267, pp. 438–441, Oct. 1943.

[26]   T. A. Gennarelli, "Mechanisms of brain injury," *Journal of Emergency Medicine*, vol. 11, no. SUPPL. 1. pp. 5–11, Jan. 01, 1993.

[27]   J. C. Park, I. B. Chang, J. H. Ahn, J. H. Kim, J. K. Oh and J. H. Song, "Epidemiology and risk factors for bicycle-related severe head injury: a single center experience," *Korean Journal of Neurotrauma*, vol. 13, no. 2, p. 90, 2017.

[28]   A. E. Forbes, J. Schutzer-Weissmann, D. A. Menassa and M. H. Wilson, "Head injury patterns in helmeted and non-helmeted cyclists admitted to a London major trauma centre with serious head injury," *PLoS ONE*, vol. 12, no. 9, Sep. 2017.

[29]   S. Kleiven, "Why most traumatic brain injuries are not caused by linear acceleration but skull fractures are," *Frontiers in Bioengineering and Biotechnology*, vol. 1, 2013.

[30]   D. Gao and C. W. Wampler, "Head injury criterion," *IEEE Robotics and Automation Magazine*, vol. 16, no. 4, pp. 71–74, 2009.

[31]   N. Yoganandan, A. M. Nahum and J. W. Melvin, *Accidental Injury*, 3rd ed. Springer, 2015.

[32]   C. Catanese, *Traumatic brain injury: methods for clinical and forensic neuropsychiatric assessment*. CRC Press, 2007.

[33]   D. Bauer, M. L. Tung and J. W. Tsao, "Mechanisms of traumatic brain injury: biomechanical, structural and cellular considerations," *Seminars in Neurology*, vol. 35, no. 1. pp. e17–e22, 2015.

[34]   R. Gerlach, S. Dittrich, W. Schneider, H. Ackermann, V. Seifert and M. Kieslich, "Traumatic epidural hematomas in children and adolescents: outcome analysis in 39 consecutive unselected cases," *Pediatric Emergency Care*, vol. 25, no. 3, pp. 164–169, 2009.

[35]   J. L. Stone, M. H. S. Rifai, O. Sugar, R. G. R. Lang, J. B. Oldershaw and R. A. Moody, "Subdural hematomas: I. Acute subdural hematoma: progress in definition, clinical pathology, and therapy," *Surgical Neurology*, vol. 19, no. 3, pp. 216–231, 1983.

[36]   N. K. Joshi and Y. Okuda, "Intracranial hemorrhage," in *Simwars Simulation Case Book: Emergency Medicine*, Cambridge University Press, pp. 159–163, 2015.

[37]   K. L. Monson, W. Goldsmith, N. M. Barbaro and G. T. Manley, "Axial mechanical properties of fresh human cerebral blood vessels," *Journal of Biomechanical Engineering*, vol. 125, no. 2, pp. 288–294, Apr. 2003.

[38]   J. H. McElhaney, V. L. Roberts and J. F. Hilyard, "Properties of human tissues and components: nervous tissues," *Handbook of Human Tolerance (Tokyo: Automobile Research Institute Inc)*, 1976.

[39]   O. AK and G. TA, "Cerebral concussion and traumatic unconsciousness. Correlation of experimental and clinical observations of blunt head injuries," *Brain: a journal of neurology*, vol. 97, no. 4, pp. 633–654, 1974.

[40]   A. Post and T. Blaine Hoshizaki, "Rotational acceleration, brain tissue strain, and the relationship to concussion," *Journal of Biomechanical Engineering*, vol. 137, no. 3. American Society of Mechanical Engineers (ASME), Mar. 01, 2015.

[41]   A. I. Maas, N. Stocchetti and R. Bullock, "Moderate and severe traumatic brain injury in adults," *The Lancet Neurology*, vol. 7, no. 8. Elsevier, pp. 728–741, Aug. 01, 2008.

[42]   V. Singh, *Textbook of anatomy: head, neck, and brain*, Vol. 3. Elsevier Health Sciences, 2014.

[43]   B. S. Elkin and B. Morrison, "Region-specific tolerance criteria for the living brain.," *Stapp Car Crash Journal*, vol. 51, pp. 127–138, 2007.

[44]   A. C. Bain and D. F. Meaney, "Tissue-level thresholds for axonal damage in an experimental model of central nervous system white matter injury," *Journal of Biomechanical Engineering*, vol. 122, no. 6, pp. 615–622, 2000.

[45]   B. Morrison, H. L. Cater, C. C. Wang, F. C. Thomas, C. T. Hung, G. A. Ateshian, and L. E. Sundstrom, "A tissue level tolerance criterion for living brain developed with an in vitro model of traumatic mechanical loading," *SAE Technical Papers*, Oct. 2003.

[46]   J. A. W. van Dommelen, M. Hrapko and G. W. M. Peters, "Mechanical properties of brain tissue: characterisation and constitutive modelling," *Mechanosensitivity of the Nervous System*, pp. 249–279, 2009.

[47]   D. H. Smith and D. F. Meaney, "Axonal damage in traumatic brain injury," *The Neuroscientist*, pp.483-495, 2000.

[48]   D. F. Meaney, D. H. Smith, D. I. Shreiber, A. C. Bain, R. T. Miller, D. T. Ross, and T. A. Gennarelli, "Biomechanical analysis of experimental diffuse axonal injury," *Journal of Neurotrauma*, vol. 12, no. 4, pp. 689–694, 1995.

[49]   L. E. Thibault, "Brain injury from the macro to the micro level and back again: what have we learned to date?," *Proceedings of the International Research Council on the Biomechanics of Injury conference*, vol. 21, 1993.

[50]   T. A. Gennarelli, L. E. Thibault, J. H. Adams, D. I. Graham, C. J. Thompson, and R. P. Marcincin, "Diffuse axonal injury and traumatic coma in the primate," *Annals of neurology*, vol. 12, no. 6, pp. 564–574, 1982.

[51]   T. A. Gennarelli, L. E. Thibault and A. K. Ommaya, "Pathophysiologic responses to rotational and translational accelerations of the head," in *SAE Technical Papers*, Feb. 1972.

[52]   S. Kleiven, "Predictors for traumatic brain injuries evaluated through accident reconstructions," *SAE Technical Paper*, 2007.

[53]   K. Ueno and J. W. Melvin, "Finite element model study of head impact based on hybrid head acceleration: the effects of rotational and translational acceleration," *Journal of Biomechanical Engineering*, vol. 117, no. 3, pp. 319–328, 1995.

[54]   N. Dodds, R. Johnson, B. Walton, O. Bouamra, D. Yates, F. E. Lecky, and J. N. Thompson, "Evaluating the impact of cycle helmet use on severe traumatic brain injury and death in a national cohort of over 11000 pedal cyclists: A retrospective study from the NHS England Trauma Audit and Research Network dataset," *BMJ Open*, vol. 9, no. 9, Sep. 2019.

[55]   K. Bian and Haojie Mao, "Mechanisms and variances of rotation-induced brain injury: a parametric investigation between head kinematics and brain strain," *Biomechanics and Modeling in Mechanobiology*, vol. 19, pp. 2323–2341, 2020.

[56]   B. M. Knowles and C. R. Dennison, "Predicting cumulative and maximum brain strain measures from HybridIII head kinematics: a combined laboratory study and post-hoc regression analysis," *Annals of Biomedical Engineering*, vol. 45, no. 9, pp. 2146–2158, Sep. 2017.

[57]   E. G. Takhounts, M. J. Craig, K. Moorhouse, J. McFadden and V. Hasija, "Development of brain injury criteria (BrIC)," *SAE Technical Papers*, Nov. 2013.

[58]   L. F. Gabler, J. R. Crandall and M. B. Panzer, "Development of a metric for predicting brain strain responses using head kinematics," *Annals of Biomedical Engineering*, vol. 46, no. 7, pp. 972–985, Jul. 2018.

[59]   M. Bottlang, A. Rouhier, S. Tsai, J. Gregoire and S. M. Madey, "Impact performance comparison of advanced bicycle helmets with dedicated rotation-damping systems," *Annals of Biomedical Engineering*, vol. 48, no. 1, pp. 68–78, Jan. 2020.

[60]   L. Di Landro, G. Sala and D. Olivieri, "Deformation mechanisms and energy absorption of polystyrene foams for protective helmets," *Polymer Testing*, vol. 21, no. 2, pp. 217–228, Jan. 2002.

[61]   L. J. Gibson and M. F. Ashby, *Cellular solids: structure and properties, second edition*. Cambridge University Press, 2014.

[62]   A. Simpson, I. G. Rattigan, E. Kalavsky and G. Parr, "Thermal conductivity and conditioning of grey expanded polystyrene foams," *Cellular Polymers*, vol. 39, no. 6, pp. 238–262, 2020.

[63]   J. Wang, Y. Cao and S. P. Zhu, "Influence of the geometric parameters on the densification onset strain of double-walled honeycomb aluminum under out-of-plane compression," *Advances in Materials Science and Engineering*, 2020.

[64]   J. Y. Sone, D. Kondziolka, J. H. Huang and U. Samadani, "Helmet efficacy against concussion and traumatic brain injury: A review," *Journal of Neurosurgery*, vol. 126, no. 3. American Association of Neurological Surgeons, pp. 768–781, Mar. 01, 2017.

[65]   B. Leng, D. Ruan and K. M. Tse, "Recent bicycle helmet designs and directions for future research: A comprehensive review from material and structural mechanics aspects," *International Journal of Impact Engineering*, vol. 168, 2022.

[66]   S. J. Bonin, A. L. DeMarco and G. P. Siegmund, "The effect of MIPS, headform condition, and impact orientation on headform kinematics across a range of impact speeds during oblique bicycle helmet impacts," *Annals of Biomedical Engineering*, vol. 50, no. 7, pp. 860–870, 2022.

[67]   "Bicycle Helmet Liners: Foam and much more." https://helmets.org/liners.htm.

[68]   K. Hansen *et al.*, "Angular impact mitigation system for bicycle helmets to reduce head acceleration and risk of traumatic brain injury," *Accident Analysis and Prevention*, vol. 59, pp. 109–117, Oct. 2013.

[69]   M. L. Bland, C. McNally and S. Rowson, "Differences in impact performance of bicycle helmets during oblique impacts," *Journal of Biomechanical Engineering*, vol. 140, no. 9, Sep. 2018.

[70]   E. Bliven *et al.*, "Evaluation of a novel bicycle helmet concept in oblique impact testing," *Accident Analysis and Prevention*, vol. 124, pp. 58–65, 2019.

[71]   S. J. Bonin, A. L. DeMarco and G. P. Siegmund, "The effect of hair and football helmet fit on headform kinematics," *Proceedings of the International Research Council on the Biomechanics of Injury conference*, vol. 1, 2018.

[72]   "MIPS Helmet." https://www.explorethousand.com/products/mips-helmet.

[73]   "Bontrager WaveCel Helmets." https://www.trekbikes.com/us/en_US/wavecel/.

[74]   V. W. J. Chung, L. Dias, G. Booth and P. A. Cripton, "Incorporating neck biomechanics in helmet testing: evaluation of commercially available WaveCel helmets," *Clinical Biomechanics*, vol. 94, p. 105628, Apr. 2022.

[75]   "Bontrager XXX WaveCel Road Bike Helmet."

https://www.trekbikes.com/ca/en_CA/equipment/cycling-accessories/bike-helmets/wavecel-helmets/bontrager-xxx-wavecel-road-bike-helmet/p/25365/.

[76]   "HEXR - The world's first custom-fit cycling helmet." https://hexr.com/.

[77]   Consumer Product Safety Commission, "Safety standard for bicycle helmets." https://www.law.cornell.edu/cfr/text/16/part-1203.

[78]   "EN960 Standard Full Headform." 2013.

[79]   R. Daly, D. Furstinger, T. Sashegyi, and M. Shah, "Wireless impact sensing headband - W . I . S . H .," 2014.

[80]   R. Willinger, C. Deck, P. Halldin and D. Otte, "Towards advanced bicycle helmet test methods," *International Cycling Safety Conference*, pp. 1–11, 2014.

[81]   A. Sances, F. Carlin and S. Kumaresan, "Biomechanical analysis of head-neck force in hybrid III dummy during inverted vertical drops," in *Biomedical Sciences Instrumentation*, vol. 38, pp. 459–464, Jan. 2002.

[82]   J. Paver, D. Friedman, G. Mattos and J. Caplinger, "The development of IARV's for the Hybrid III neck modified for dynamic rollover crash testing," *Proceedings of the ICRASH Conference*, 2010.

[83]   B. Arosio, D. Benetton, M. Anghileri, M. Mongiardini, G. Mattos and R. Gzerbieta, "Comparison of Hybrid III and human body model in head injury encountered in pendulum impact and inverted drop tests," *Proceedings of the First International Roadside Safety Conference*, 2017.

[84]   J. K. Foster, J. O. Kortge and M. J. Wolanin, "Hybrid III - A biomechanically-based crash test dummy," *SAE Technical Papers*, Feb. 1977.

[85]   H. J. Mertz, P. Prasad and A. L. Irwin, "Injury risk curves for children and adults in frontal and rear collisions," *SAE Technical Papers*, 1997.

[86]   W. Goldsmith, G. T. Wang, K. Li and D. Crane, "Perforation of cellular sandwich plates," *International Journal of Impact Engineering*, vol. 19, no. 5–6, pp. 361–379, May 1997.

[87]   S. D. Papka and S. Kyriakides, "Biaxial crushing of honeycombs: - Part 1: Experiments," *International Journal of Solids and Structures*, vol. 36, no. 29, pp. 4367–4396, May 1999.

[88]   C. Baumgart, T. Halle, C. Weigelt, L. Krüger and C. G. Aneziris, "Effect of honeycomb cell geometry on compressive properties: finite element analysis and experimental verification," *Science and Technology of Materials*, vol. 30, no. 1, pp. 35–42, Jan. 2018.

[89]   A. Mughal, T. Libertiny and G. E. Schröder-Turk, "How bees and foams respond to curved confinement: Level set boundary representations in the Surface Evolver," *Colloids*

and Surfaces A: Physicochemical and Engineering Aspects, vol. 534, pp. 94–104, 2017.

[90]   "How to Tell if You Have a Strong Hive." https://beekeepinglikeagirl.com/how-to-tell-if-you-have-a-strong-hive/.

[91]   T. Zhang, X. Li and H. Gao, "Designing graphene structures with controlled distributions of topological defects: A case study of toughness enhancement in graphene ruga," *Extreme Mechanics Letters*, vol. 1, pp. 3–8, 2014.

[92]   B. Yu, D. A. van Egmond, K. A. Samk, U. Erb, D. Wilkinson, D. Embury, and H. Zurob, "The design of 'Grain Boundary Engineered' architected cellular materials: The role of 5-7 defects in hexagonal honeycombs," *Acta Materialia*, vol. 243, 2023.

[93]   J. Zhang and M. F. Ashby, "The out-of-plane properties of honeycombs," *International Journal of Mechanical Sciences*, vol. 34, no. 6, pp. 475–189, 1992.

[94]   P. G. Davis, "The bioerosion of bird bones," *International Journal of Osteoarchaeology*, vol. 7, no. 4, pp. 388–401, 1997.

[95]   M. L. Smith, N. Napp and K. H. Petersen, "Imperfect comb construction reveals the architectural abilities of honeybees," *Proceedings of the National Academy of Sciences of the United States of America*, vol. 118, no. 31, pp. 1–8, 2021.

[96]   H. Delye, P. Verschueren, B. Depreitere, I. Verpoest, D. Berckmans, J. Vander Sloten, G. Van Der Perre, and J. H. Goffin, "Biomechanics of frontal skull fracture," *Journal of Neurotrauma*, vol. 24, no. 10, pp. 1576–1586, 2007.

[97]   M. L. Bland, C. McNally, J. B. Cicchino, D. S. Zuby, B. C. Mueller, M. L. McCarthy, C. D. Newgard, P. E. Kulie, B. N. Arnold, and S. Rowson, "Laboratory reconstructions of bicycle helmet damage: investigation of cyclist head impacts using oblique impacts and computed tomography," *Annals of Biomedical Engineering*, vol. 48, no. 12, pp. 2783–2795, Sep. 2020.

[98]   ASTM, "Standard test method for shear properties of sandwich core materials"

[99]   K. C. Chan and L. S. Xie, "Dependency of densification properties on cell topology of metal foams," *Scripta Materialia*, vol. 48, no. 8, pp. 1147–1152, 2003.

[100] N. A. Fleck, V. S. Deshpande and M. F. Ashby, "Micro-architectured materials: past, present and future," *Proceedings of the Royal Society A: Mathematical, Physical and Engineering Sciences*, vol. 466, no. 2121, pp. 2495–2516, 2010.

[101] M. F. Ashby, "The properties of foams and lattices," *Philosophical Transactions of the Royal Society A: Mathematical, Physical and Engineering Sciences*, vol. 364, pp. 15–30, 2006.

[102] R. Nightingale, J. McElhaney, W. Richardson and B. Myers, "Dynamic responses of the

head and cervical spine to axial impact loading," *Journal of biomechanics*, vol. 29, no. 3, pp. 307–318, 1996.

[103] R. P. Ching, D. C. Thompson, R. S. Thompson, D. J. Thomas, W. C. Chilcott and F. P. Rivara, "Damage to bicycle helmets involved with crashes," *Accident Analysis and Prevention*, vol. 29, no. 5, pp. 555–562, 1997.

Appendix A – Glossary of Anatomical Terms

Arachnoid mater	Thin membrane between the brain and the skull with a spiderweb-like appearance (part of the meninges).
Axons	Part of a neuron that signals travel through.
Brain	Complex organ, that with the spinal cord, makes up the central nervous system.
Cerebrum	Region of the brain that makes up the majority of its volume.
Cortex	The outer layer of the brain (also known as grey matter).
Cranium	Bony structure that encloses the brain (also known as the skull).
Dura mater	Strong layer of connective tissue between the brain and the skull (part of the meninges).
Epidural	Space between the skull and the dura mater.
Intracerebral	Within the cerebrum.
Limbic system	Set of structures in the brain involved in behavioural and emotional responses.
Microtubules	Polymers of tubulin that form part of the cytoskeleton.
Neck extension	Movement of bending the head backward.
Neck flexion	Movement of bending the head forward.
Neuron	Functional cells of the brain that transmit signals to other nerve cells, muscles, or gland cells.
Pia mater	Membrane around the surface of the that allows the flow of blood vessels to the brain tissue and helps to contain cerebrospinal fluid.
Sagittal plane	Anatomical plane that divides the body into left and right sections.
Subdural	Between the dura mater and the arachnoid membrane.
Tissue	Group of cells that perform a specific function.

Thalamus   Area of the brain that processes information from the senses.

White matter   Deep tissue of the brain.

Appendix B – Shear Modulus to Rotational Acceleration Derivation

This appendix contains the derivation that defines the relationship between the shear modulus (G) of the honeycomb and the rotational acceleration of the head (α_h) following an impact.

Symbols in relation to honeycomb:

τ = shear stress

G = shear modulus

γ = shear strain

Δ = shear deformation

b = depth of honeycomb

Symbols in relation to the impact:

F_{tan} = tangential component of impact force

A = estimated contact area

r_h = radius of head

I_h = moment of inertia of head (assuming it is a sphere)

α_h = rotational acceleration of head

m_h = mass of head

v_{tan} = tangential component of impact velocity

$v_{tan,0}$ = initial tangential component of impact velocity

Symbols in relation to the differential equation:

t = time (0 is instant of impact)

$\Delta(t)$ = shear deformation

$\Delta'(t)$ = rotational velocity of head

$\Delta''(t)$ = rotational acceleration of head

In the linear-elastic regime of the honeycomb stress-strain curve, shear stress (τ) is given by Hooke's law:

$$\tau = G\gamma = G\left(\frac{\Delta}{b}\right)$$

The tangential force component applied to the head by the impact (F_{tan}) is related to shear stress on the honeycomb helmet:

$$F_{tan} = \tau A$$

The tangential component of the impact force (F_{tan}) is given by Newton's law:

$$F_{tan}r_h = I_h\alpha_h = \frac{2}{5}m_h r_h^2 \alpha_h$$

$$F_{tan} = \frac{2}{5}m_h r_h \alpha_h$$

The above equations give an ordinary differential equation:

$$\frac{2}{5}m_h r_h \alpha_h = G\left(\frac{\Delta}{b}\right)A$$

$$\Delta''(t) = -\left(\frac{GA}{m_{head}r_{head}b}\right)\Delta(t)$$

The instant of impact gives the boundary conditions:

$\Delta(0) = 0$ and $v_{tan}(0) = \Delta(0) = v_{tan,0}$

The solution to the ordinary differential is as follows:

$$\Delta(t) = \frac{v_{tan,0}}{\sqrt{\left(\frac{GA}{m_h b}\right)}}\sin\left(\sqrt{\left(\frac{GA}{m_h b}\right)}t\right)$$

$$\Delta'(t) = v_{tan} \cos\left(\sqrt{\frac{GA}{m_h b}}\, t\right)$$

$$\Delta''(t) = -\sqrt{\frac{GA}{m_h b}}\, v_{tan,0} \sin\left(\sqrt{\frac{GA}{m_h b}}\, t\right)$$

According to the solution of the differential equation, to minimize rotational head acceleration ($\Delta''(t)$), the G of the honeycomb must be minimized.

Appendix C – 3D-Printing Settings

This appendix contains the settings used in Creality Slicer (Creality 3D Technology Co., Shenzhen, China) for 3D-printing flat honeycomb samples (Chapter 2 and Chapter 3).

Quality		
Layer Height	0.2	mm
Initial Layer Height	0.3	mm
Line Width	0.38	mm

Shell		
Wall Thickness	0.76	mm
Wall Line Count	2	
Top/Bottom Thickness	0.9	mm
Top Thickness	0.9	mm
Top Layers	0	
Bottom Thickness	0.9	mm
Bottom Layers	999999	
Top/Bottom Pattern	Lines	
Outer Before Inner Walls		
Fill Gaps Between Walls	Everywhere	

Infill		
Infill Density	100	%
Infill Line Distance	0.38	mm
Infill Pattern	Lines	
Minimum Infill Area	0	mm²

Material		
Printing Temperature	220	°C
Build Plate Temperature	60	°C
Flow	100	%

| Speed | | |

Print Speed		50.0	mm/s
Infill Speed		50.0	mm/s
Wall Speed	↺ 𝑓𝑥	30.0	mm/s
Outer Wall Speed		30.0	mm/s
Inner Wall Speed		30.0	mm/s
Top/Bottom Speed	↺ 𝑓𝑥	30	mm/s
Travel Speed		120.0	mm/s
Skirt/Brim Speed	🔗 ↺ 𝑓𝑥	40	mm/s
Number of Slower Layers	🔗	2	

⬚ Travel

Enable Retraction		✓	
Retraction Distance	↺	3	mm
Retraction Speed	↺	25	mm/s
Retraction Extra Prime Amount		0	mm³

✴ Cooling ⚙

Enable Print Cooling		✓	
Fan Speed		100.0	%
Regular Fan Speed at Height		0.7	mm
Minimum Layer Time		10	s

⬗ Support

⬦ Build Plate Adhesion

Build Plate Adhesion Type	🔗	Brim	⌄
Skirt/Brim Minimum Length	↺	500	mm
Brim Width	🔗 ↺	5.0	mm
Brim Distance	🔗	0	mm

Appendix D – Technical Drawings

This appendix contains detailed and dimensioned drawings of components for shear testing (Chapter 2) and dynamic impact testing (Chapter 3). The drawings were made in AutoCAD Inventor (San Francisco, California, USA) and the parts were machined by the author in the McMaster University Mechanical Engineering Machine Shop.
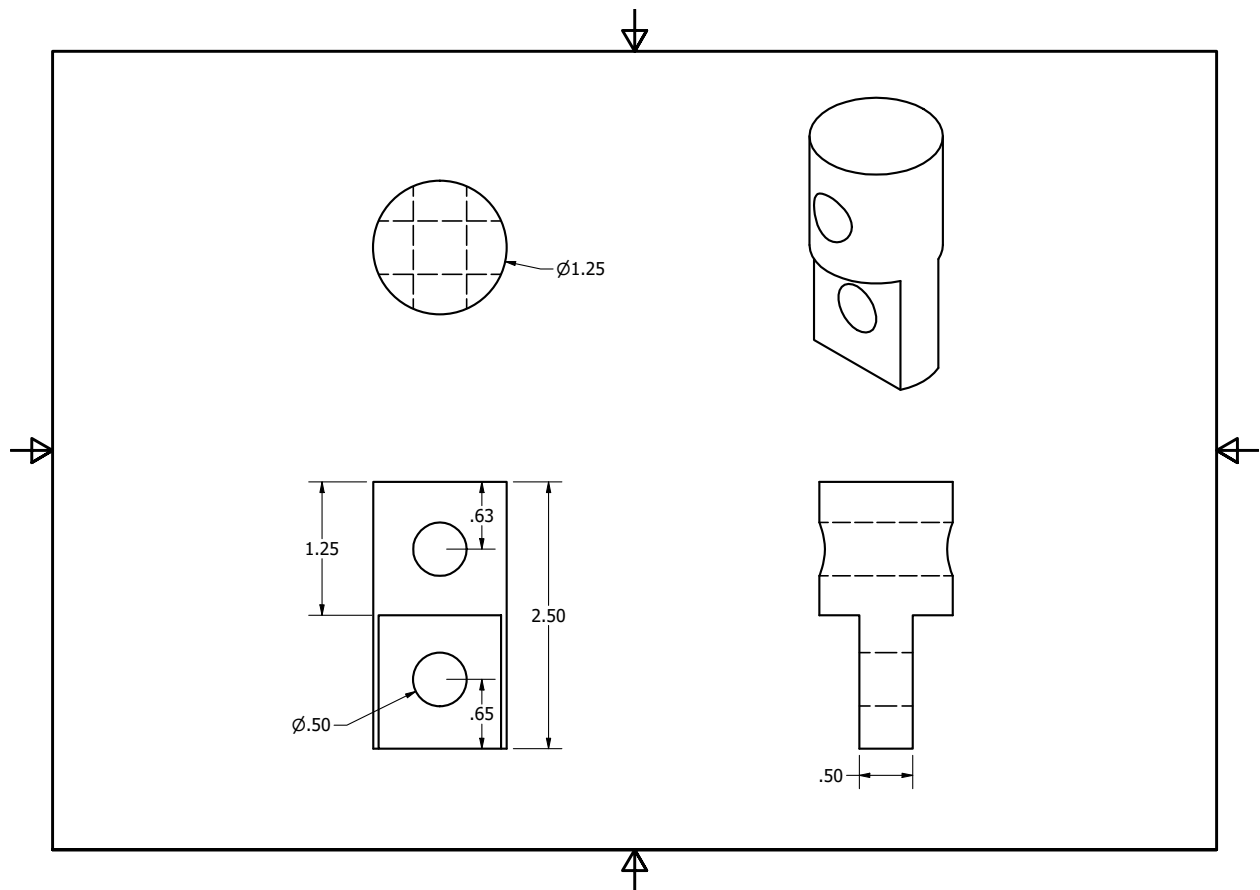

Figure D.1: Dimensioned Drawing of Connection from Intron to Shear Apparatus
Dimensions are in inches, part was made of steel.

Figure D.2: Dimensioned Drawing of Shear Loading Plates
Dimensions are in inches, part was made of steel.

Figure D.3: Dimensioned Drawing of Intermediate Plates for Shear Apparatus
Dimensions are in inches, part was made of steel.

Figure D.4: Dimensioned Drawing of Load Cell Connector
Dimensions are in inches, part was made of steel.

Ø2.00

Ø1.00

Ø6.00

Ø.375

1.25   1.125

.50

Figure D.5: Dimensioned Drawing of Flat Anvil
Dimensions are in inches, part was made of steel.
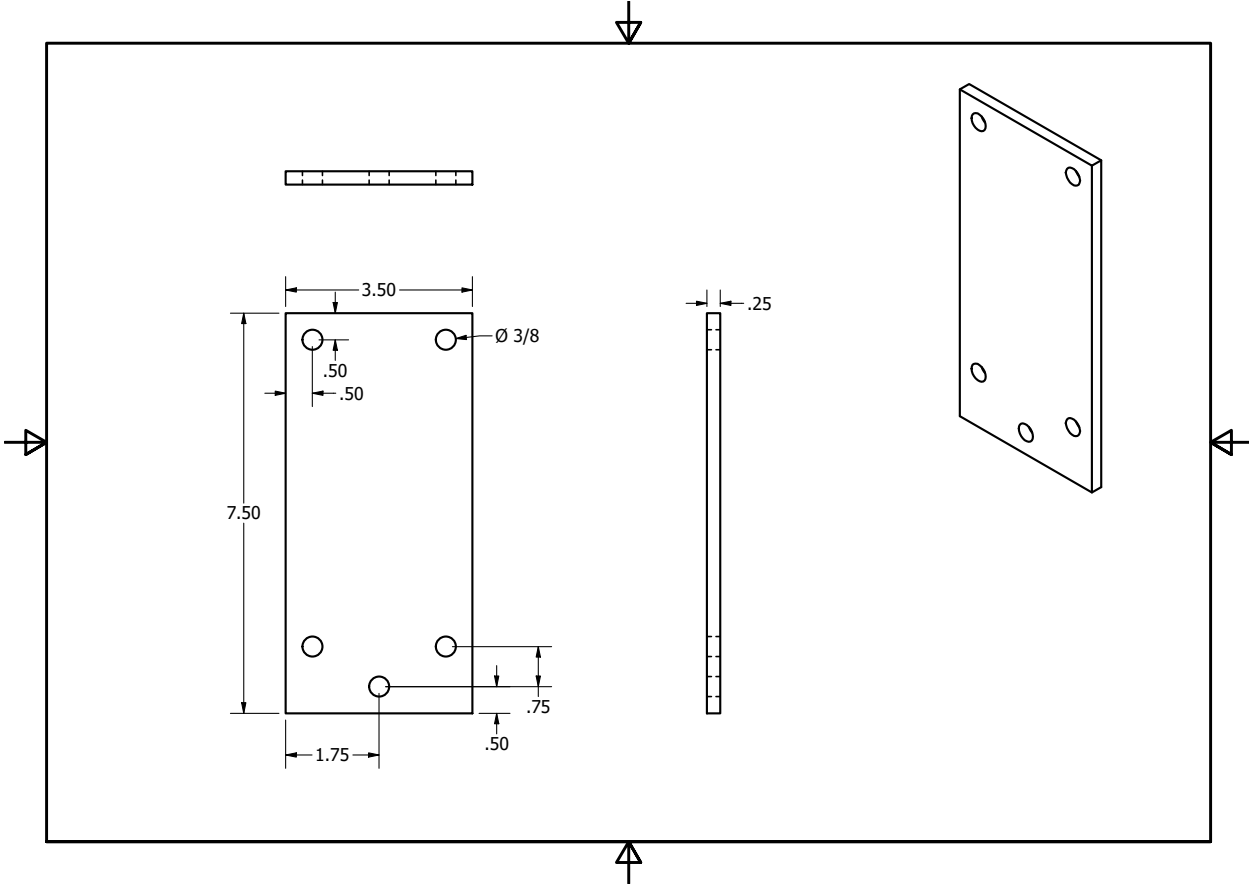
Ø6.00

.281

6.00

3.855

155°

.50

Ø1.00

.592

3.085

Figure D.6: Dimensioned Drawing of Flat Impactor
Dimensions are in inches, part was made of steel.

Figure D.7: Dimensioned Drawing of Angled Anvil
Dimensions are in inches, part was made of steel.

Figure D.8: Dimensioned Drawing of Angled Impactor
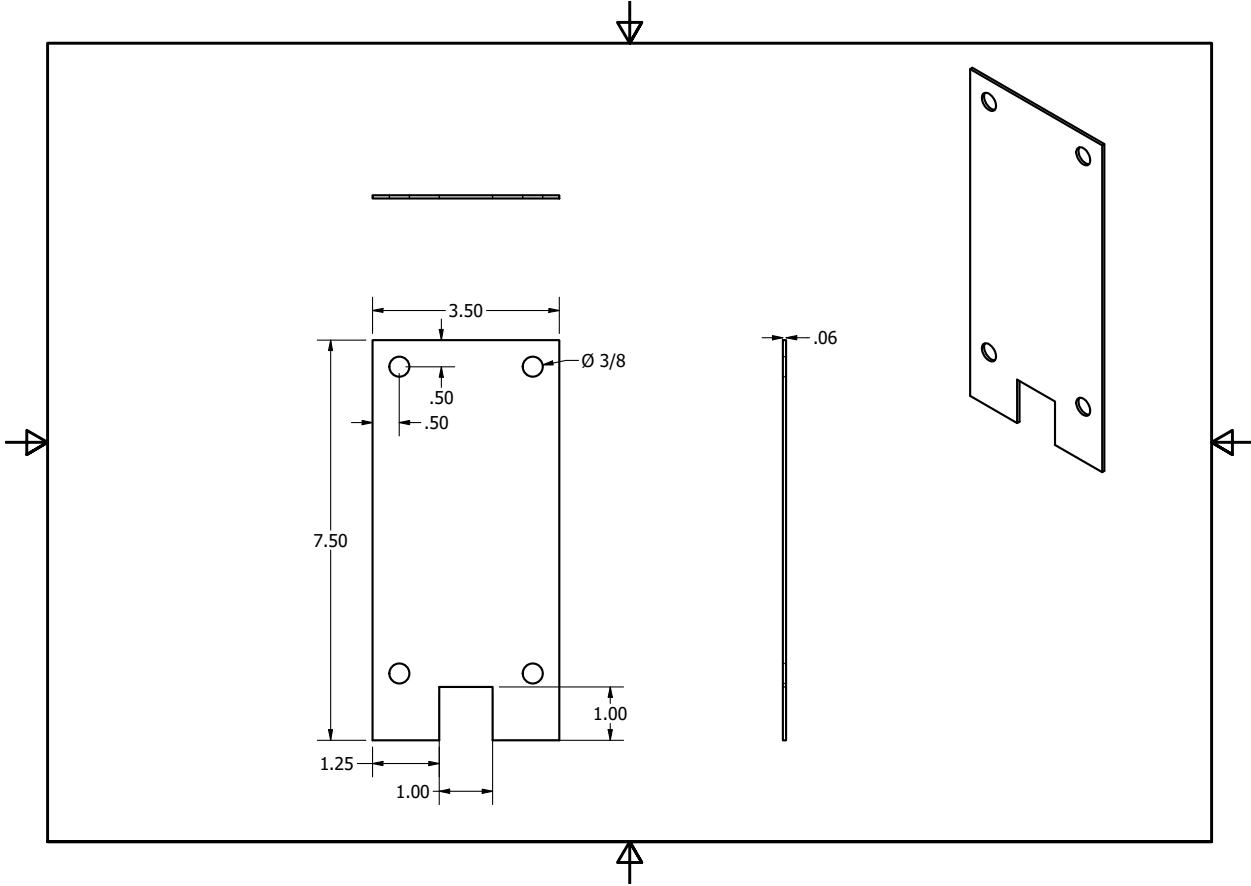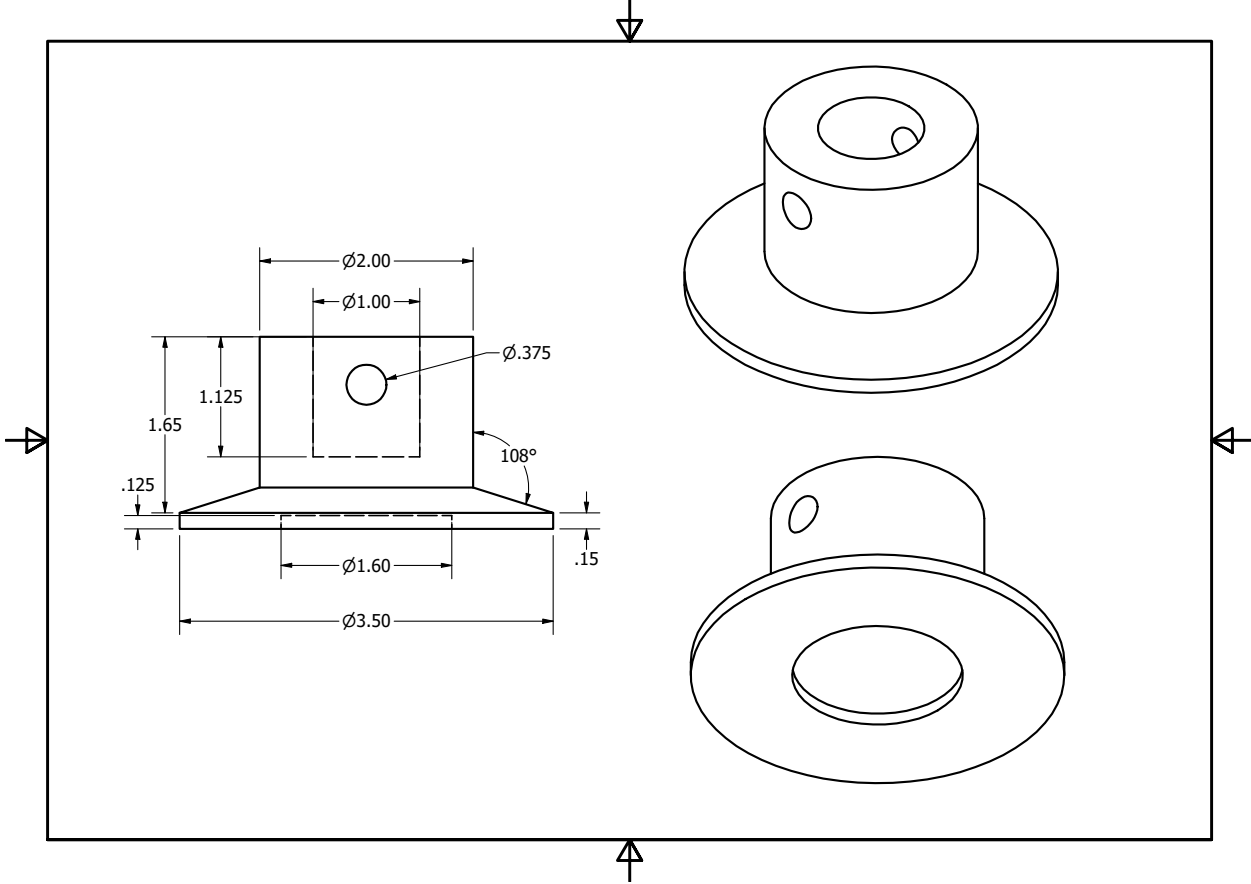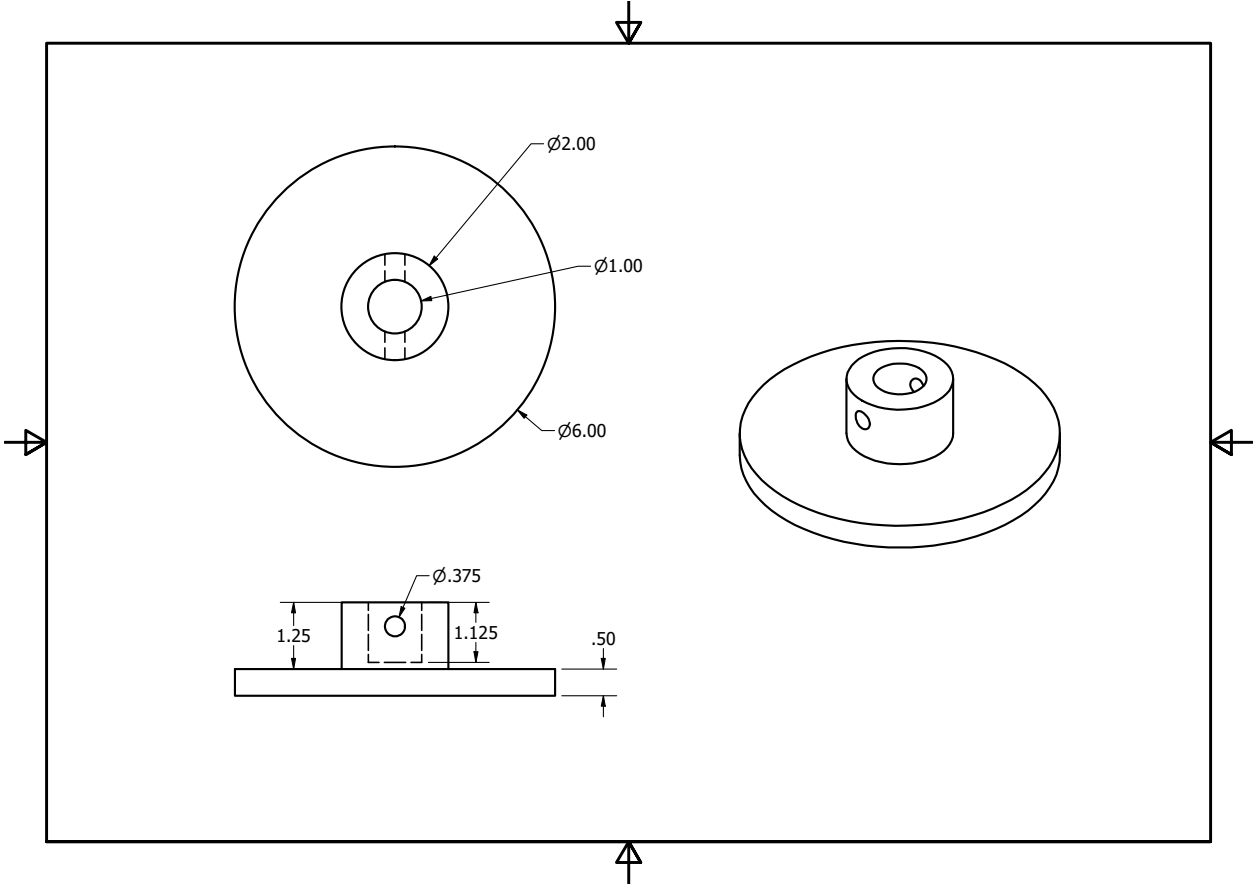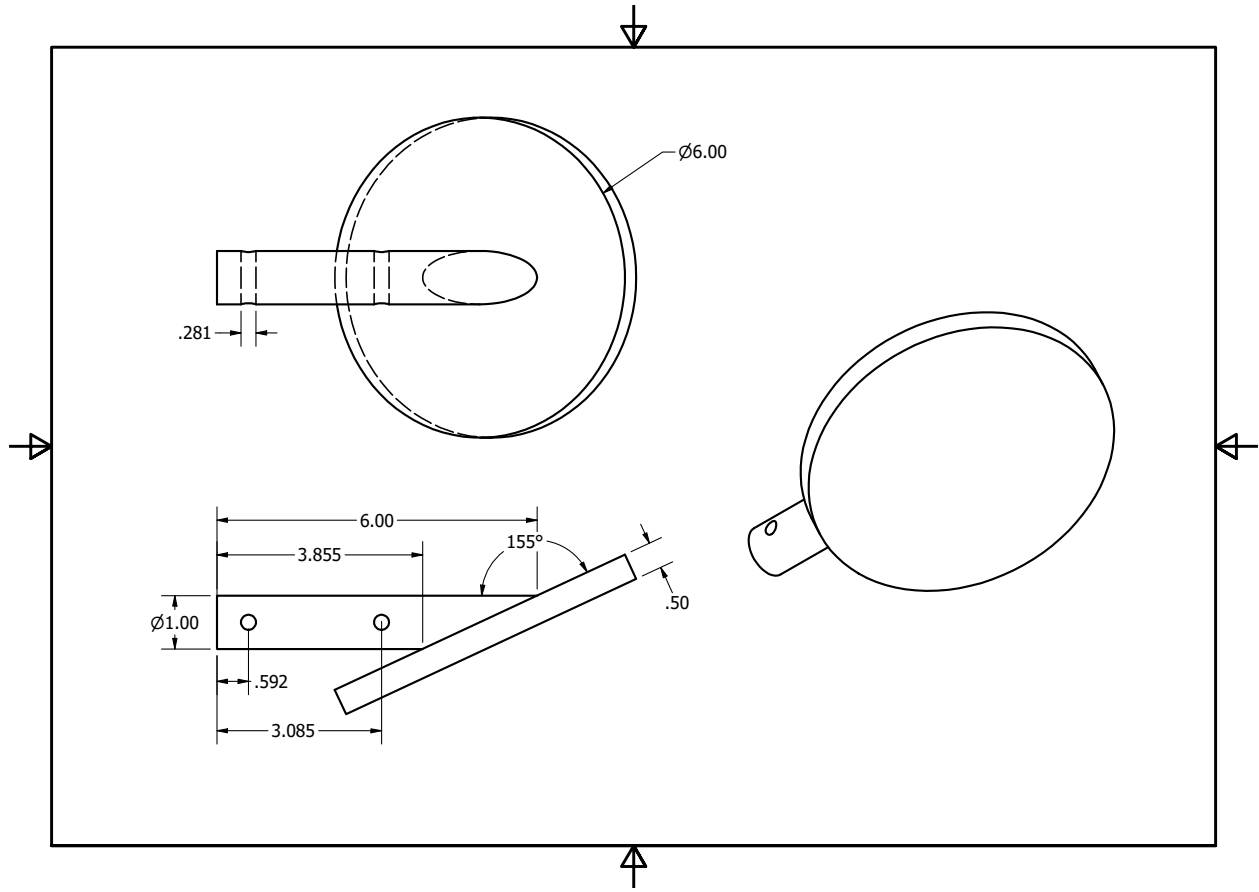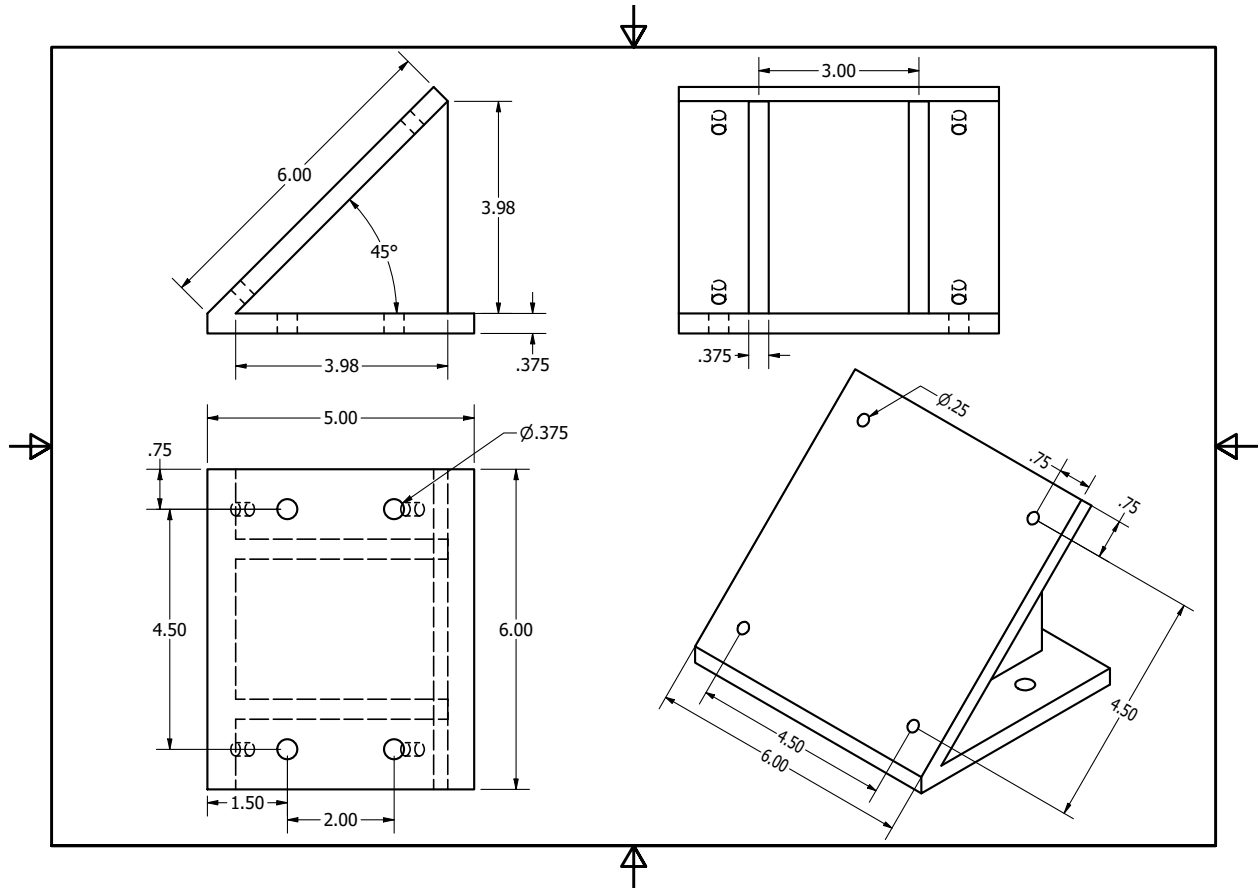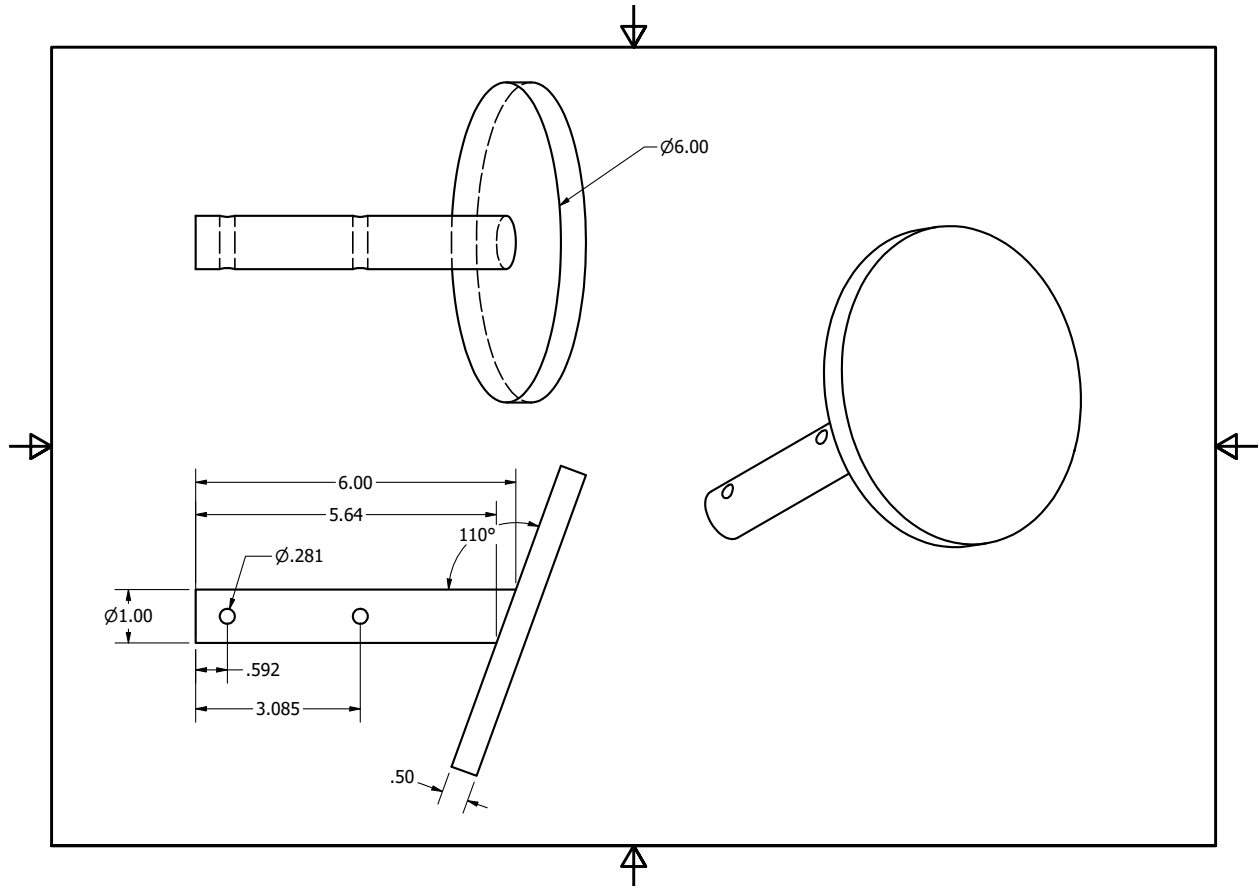Dimensions are in inches, part was made of steel.

Appendix E – MATLAB Code

This appendix contains important parts of the MATLAB (The MathWorks Inc., Natick, MA, USA) code used for analyzing data in Chapter 2 and Chapter 3.

```matlab
%% QUASI-STATIC COMPRESSION

%% General parameters
initial_height = 25; %thickness of honeycomb/EPS foam sample (mm)
initial_area = 94*94; %area of honeycomb/EPS foam sample (mm^2)

%% Sample data (honeycomb)
force_displacement = csvread('T21-timeforcedisplacement.csv'); %change name
according to sample (force in N, displacement in mm)
displacement = force_displacement(:,2); %mm
force = force_displacement(:,3); %N
strain = displacement/initial_height; %unitless
stress = force/initial_area; %MPa
rows = height(force_displacement); %finds number of data points

%draw line with max slope down to x-axis and shift to origin
for i = 40 : 1000
    rise = stress(i+10)-stress(i-10); %change in stress
    run = strain(i+10)-strain(i-10); %change in strain
    slope = rise/run; %approximating instantaneous slopes
    sl(i,1) = slope; %fills matrix of slope values
end

[M, start_row] = max(sl(:,1)); %M is max slope, start_row is row M occurs
bvalue = stress(start_row) - (M * strain(start_row)); %current y-intercept
xintercept = -bvalue/M; %current x-intercept

T21strain_data = (vertcat(xintercept, strain(start_row:rows)))-xintercept;
%strain data shifted to origin
T21stress_data = vertcat(0, stress(start_row:rows)); %stress data

%find densification strain
l = 5000;
while l < rows
    rise = T21stress_data(l+10)-T21stress_data(l-10); %change in stress
    run = T21strain_data(l+10)-T21strain_data(l-10); %change in strain
    slope = rise/run; %approxinating instantaneous slopes
    if slope > M %find when slope reaches max slope in linear-elastic regime
        Densrow = l; %current row is when densification occurs
        T21Densstrain = T21strain_data(Densrow); %define densification strain
        l = rows; %exit loop
    end
```

```matlab
    l = l + 40;
end

%find U_v (energy absorption per unit volume) and sigma_p (peak stress)
T21stress_before_dens = T21stress_data(1:Densrow); %stress data points before
densifcation only
T21strain_before_dens = T21strain_data(1:Densrow); %strain data points before
densifcation only
T21energy_ab = trapz(T21strain_before_dens, T21stress_before_dens);
%approximate intergral of strain w.r.t. strain
T21peak_stress = max(T21stress_data(1:Densrow-2000)); %finds peak stress
value

%this code is repeated for each sample

%% Find densification strain – EPS foam

integrate = cumtrapz(EPS1strain_data, EPS1stress_data); %integrate using
trapazoid method
nu = zeros(rows2,1); %empty matrix for instantaneous energy absorption
efficiency
for i = 2 : rows2
    New = integrate(i,1)/EPS1stress_data(i,1); %calculate instantaneous
energy absorption efficiency
    nu(i,1) = New; %fill energy absorption efficiency matrix
end
[maxvalue, Densrow] = max(nu); %global maximum of energy absorption
efficiency and row in nu matrix where it occurs
EPS1Densstrain = EPS1strain_data(Densrow) %find densification strain value

%this code replaces 'find densification strain' in code above for all EPS
%foam samples

%% Average data for samples in the same group (ex: regular honeycomb,
relative density = 15%)
T2_Rd = mean([0.1456, 0.1499, 0.1472]); %average relative density of samples
in group

T2strain_data = cat(1,T21strain_plot,T22strain_plot, T23strain_plot);
%concatenate strain data for samples in the same group
T2stress_data = cat(1,T21stress_plot,T22stress_plot, T23stress_plot);
%concatenate stress data for samples in the same group

T2Xnew = min(T2strain_data):0.001:max(T2strain_data); %resample strain to be
equally distributed
T21Ynew = interp1(T21strain_data, T21stress_data, T2Xnew); %interpolate
sample 1 stress data according to resampled strain data
T22Ynew = interp1(T22strain_data, T22stress_data, T2Xnew); %interpolate
sample 2 stress data according to resampled strain data
T23Ynew = interp1(T23strain_data, T23stress_data, T2Xnew); %interpolate
sample 3 stress data according to resampled strain data
T2Yavg = (T21Ynew + T22Ynew + T23Ynew)/3; %find average of stress at each
strain point
```

```matlab
T2peak_stresses = [T21peak_stress, T22peak_stress, T23peak_stress]; %peak
stress for each sample
T2peak_stress_av = mean(T2peak_stresses); %average peak stress in group
T2peak_stress_delta = std(T2peak_stresses); %standard deviation of peak
stress in group
T2peak_stress_SEM = std(T2peak_stresses)/sqrt(length(T2peak_stresses));
%standard error of peak stress in group

T2energy_ab = [T21energy_ab, T22energy_ab, T23energy_ab]; %energy absorption
per unit volume for each sample
T2energy_ab_av = mean(T2energy_ab); %average energy absorption per unit
volume in group
T2energy_delta = std(T2energy_ab); %standard deviation of energy absorption
per unit volume in group
T2energy_SEM = std(T2energy_ab)/sqrt(length(T2energy_ab)); %standard error of
energy absorption per unit volume in group

%this code is repeated for each group

%% Plot average stress-strain curves
%plot average stress strain curve for each group (ex: each relative
%density)
figure("Stress-Strain")
plot(T1Xnew, T1Yavg, 'color',[0.8500 0.3250 0.0980], 'LineWidth', 3)
hold on
plot(T2Xnew, T2Yavg, 'color', [0 0.4470 0.7410], 'LineWidth', 3)
hold on
plot(T3Xnew, T3Yavg, 'color', [0.6350 0.0780 0.1840], 'LineWidth', 3)
hold on
plot(T5Xnew, T5Yavg, 'color', [0 0.5 0], 'LineWidth', 3)
hold on
plot(T7Xnew, T7Yavg, 'color', [0.9290 0.6940 0.1250], 'LineWidth', 3)
hold on
plot(T6Xnew, T6Yavg, 'color', [0.4940 0.1840 0.5560], 'LineWidth', 3)
hold off
set(gca,'FontSize',30, 'LineWidth', 2, 'FontName', 'Times')
set(gcf, 'Position',[100,100,1000,700])
xlim([0 0.68])
ylim([0 2.2])
yticks([0 0.25 0.5 0.75 1 1.25 1.5 1.75 2 2.25])

%this code is repeated for each comparison (relative density, 5-7 defects,
strain rate, reusability, honeycomb vs EPS foam)

%% Peak stress data for all groups
x_Rd_values = [T1_Rd T2_Rd T3_Rd T5_Rd T7_Rd T6_Rd]; %average relative
density for all groups
Rd_extra = [0 0.01 0.02 0.03 0.04 0.05 0.06 0.07 0.08 0.09 0.1 0.11 0.12
T1_Rd T2_Rd T3_Rd T5_Rd T7_Rd T6_Rd 0.29 0.30 0.31 0.32 0.33 0.34]; %extra
values for plotting regression
y_peak_stress = [T1peak_stress_av T2peak_stress_av T3peak_stress_av
T5peak_stress_av T7peak_stress_av T6peak_stress_av]; %average peak stress for
all groups
```

```
[peak_stress_p, peak_stress_S] =
polyfit(log(x_Rd_values),log(y_peak_stress),1); %p returns coefficients for
best fit polynomial on log of rd and peak stresses
peak_stress_regression = polyval(peak_stress_p, Rd_extra); %evaluates
polynomial at each relative density value
mvalue_peak_stress = peak_stress_p(1); %coefficient of power function
bvalue_peak_stress = exp(peak_stress_p(2)); %exponent of power function
R2_peak_stress = 1 – (peak_stress_S.normr/norm(log(y_peak_stress) –
mean(log(y_peak_stress))))^2; %find coefficient of determination (R^2)

skull_fracture_threshold = 1.46; %from literature (MPa)

figure("Peak Stress")
err = [T1delta, T2delta, T3delta T5delta T7delta T6delta]; %standard
deviation for peak stress in each group
errorbar(x_Rd_values, y_peak_stress, err, '.r', 'MarkerSize', 50,
'LineWidth', 3) %make points with standard deviation error bars
xlim([0 0.285])
ylim([0 2.25])
xticks([0 0.05 0.1 0.15 0.2 0.25])
yticks([0 0.25 0.5 0.75 1 1.25 1.5 1.75 2])
hold on
plot(Rd_extra, bvalue_peak_stress*Rd_extra.^mvalue_peak_stress, ':k',
'LineWidth', 3) %plot regression
hold on
yline(skull_fracture_threshold, '--r', 'LineWidth', 3) %plot skull fracture
threshold
hold off
set(gca,'FontSize',30, 'LineWidth', 2, 'FontName', 'Times')
set(gcf, 'Position',[100,100,1000,700])

%this code is repeated for each comparison (relative density, 5–7 defects,
strain rate, reusability, honeycomb vs EPS foam)

%% Energy absorption per unit volume data for all groups
y_energy_ab = [T1energy_ab_av T2_energy_ab_av T3energy_ab_av T5energy_ab_av
T7energy_ab_av T6energy_ab_av]; %average energy absoption per unit volume for
all groups

[energy_ab_p, energy_ab_S] = polyfit(log(x_Rd_values),log(y_energy_ab),1); %p
returns coefficients for best fit polynomial on log of rd and energy
absorption
energy_ab_regression = polyval(energy_ab_p, Rd_extra); %evaluates polynomial
at each relative density value
mvalue_energyab = energy_ab_p(1) %coefficient of power function
bvalue_energyab = exp(energy_ab_p(2)) %exponent of power function
R2_energyab = 1 – (energy_ab_S.normr/norm(log(y_energy_ab) –
mean(log(y_energy_ab))))^2 %find coefficient of determination (R^2)

figure("Energy Ansorption per Unit Volume")
err = [T1energydelta T2energydelta, T3energydelta T5energydelta T7energydelta
T6energydelta]; %standard deviation for enerby absorption in each group
errorbar(x_Rd_values, y_energy_ab, err, '.b', 'MarkerSize', 50, 'LineWidth',
3) %make points with standard deviation error bars
```

```matlab
xlim([0 0.3])
ylim([0 inf])
xticks([0 0.05 0.1 0.15 0.2 0.25 0.3])
yticks([0 0.2 0.4 0.6 0.8 1.0 1.2 1.4 1.6 1.8 2.0])
hold on
plot(Rd_extra, bvalue_energyab*Rd_extra.^mvalue_energyab, ':k', 'LineWidth',
3) %plot regression
hold off
set(gca,'FontSize',30, 'LineWidth', 2, 'FontName', 'Times')
set(gcf, 'Position',[100,100,1000,700])

%this code is peated for each comparison (relative density, 5-7 defects,
strain rate,
%reusability, honeycomb vs EPS foam)


%% QUASI-STATIC SHEAR

%% General parameters
initial_height = 10; %thickness of sample to determine stress/strain (mm)
initial_area = 120*74;

%% Sample data

Force_displacement = csvread('ST01S1-forcedisplacement.csv'); %change name
according to sample (force in N, displacement in mm)
Displacementdata = Force_displacement(:,1); %mm
Forcedata = Force_displacement(:,2); %N
strain = Displacementdata/initial_height; %unitless
stress = Forcedata/initial_area; %MPa
rows = height(Force_displacement); %finds number of data points

%filtering peaks due to movement of the test apparatus
starta = 48; %row where movement starts (chosen by observing data)
enda = 154; %row where movement ends (chosen by observing data)
valuea = strain(enda)-strain(starta); %range of strain during movement
straina = vertcat(strain(1:starta), (strain(enda:rows)-valuea)); %shifted
strain data
stressa = vertcat(stress(1:starta), stress(enda:rows)); %new stress data
rowsa = height(straina); %new number of data points
%repeated for all occurances of movement of the test apparatus

%linear regression on portion of graph before elbow
i = 1;
while i < 2000
    if stressa(i) > 0.2 %observed elbow
        chooserow = i;
        i = 2001; %exit loop
    end
    i = i + 1;
end
```

```matlab
[p, S] = polyfix(straina(1:chooserow), stressa(1:chooserow), 1, straina(1), 
stressa(1)); %p returns coefficients for best fit polynomial on stress and 
strain
lregression = polyval(p, straina(1:chooserow)); %evaluates polynomial at each 
strain value
mvalue = p(1); %slope of linear regression
bvalue = stress(1) – (mvalue * straina(1)); %y-intercept of linear regression
xin = –bvalue/mvalue; %x-intercept of linear regression

ST01S1strain = vertcat(xin, straina)–xin; %strain data shifted to origin
ST01S1stress = vertcat(0, stressa(1:rowsa)); %stress data
ST01S1G = mvalue; %sample shear modulus

%this code is repeated for each sample

%% Average data for samples in the same group (ex: relative density = 14%)
ST01_Rd = mean([ST01S5_Rd ST01S6_Rd ST01S7_Rd]); %average relative density of 
samples in group
ST01_Rdsd = std([ST01S5_Rd ST01S6_Rd ST01S7_Rd]); %standard deviation of 
relative density for samples in group

ST01strain_data = cat(1, ST01S1strain, ST01S2strain, ST01S3strain); 
%concatenate strain data for samples in the same group
ST01stress_data = cat(1, ST01S1stress, ST01S2stress, ST01S3stress); 
%concatenate stress data for samples in the same group

ST01Xnew = min(ST01strain_data):0.0001:max(ST01strain_data); %resample strain 
to be equally distributed
ST01S5Ynew = interp1(ST01S5strain, ST01S5stress, ST01Xnew); %interpolate 
sample 1 stress data according to resampled strain data
ST01S6Ynew = interp1(ST01S6strain, ST01S6stress, ST01Xnew); %interpolate 
sample 2 stress data according to resampled strain data
ST01S7Ynew = interp1(ST01S7strain, ST01S7stress, ST01Xnew); %interpolate 
sample 3 stress data according to resampled strain data
ST01Yavg = (ST01S5Ynew + ST01S6Ynew + ST01S7Ynew)/3; %find average of stress 
at each strain point

ST01Gs = [ST01S5G ST01S6G ST01S7G]; %shear modulus for each sample
ST01Gav = mean(ST01Gs); %average shear modulus in group
ST01stdevG = std(ST01Gs); %standard deviation of shear modulus in group

%this code is repeated for each group

%% Plot Stress–Strain
%plot average stress strain curve for each group (ex: each relative density)

figure("Stress–Strain")
plot(ST01Xnew, ST01Yavg, 'color',[0.8500 0.3250 0.0980], 'LineWidth', 3)
hold on
plot(ST015Xnew, ST015Yavg, 'color', [0 0.4470 0.7410], 'LineWidth', 3)
hold on
plot(ST02Xnew, ST02Yavg, 'color', [0.6350 0.0780 0.1840], 'LineWidth', 3)
hold on
plot(ST025Xnew, ST025Yavg, 'color', [0 0.5 0], 'LineWidth', 3)
```

```matlab
hold off
set(gca,'FontSize',30, 'LineWidth', 2, 'FontName', 'Times')
set(gcf, 'Position',[100,100,1000,700])
xlim([0 3.5])
yticks([0 0.25 0.5 0.75 1 1.25 1.5 1.75 2 2.25])

%this code is repeated for each comparison (relative density, 5-7 defects,
strain rate, reusability, honeycomb vs EPS foam)

%% Shear modulus data for all groups (relative densities)
y_Gs = [ST01Gav ST015Gav ST02Gav ST025Gav]; %average shear modulus for all
groups
x_rdvalues = [ST01_Rd ST015_Rd ST02_Rd ST025_Rd]; %average relative density
for all groups

[p, S] = polyfit(log(x_rdvalues),log(y_Gs),1); %p returns coefficients for
best fit polynomial on log of rd and shear modulus
Gregression = polyval(p, Rd_extra); %evaluates polynomial at each relative
density value
mvalue = p(1); %coefficient of power function
bvalue = exp(p(2)); %exponent of power function
R2G = 1 - (S.normr/norm(log(y_Gs) - mean(log(y_Gs))))^2 %find coefficient of
determination (R^2)

figure("Shear Modulus")
err = [ST01stdevG ST015stdevG ST02stdevG ST025stdevG]; %standard deviation
for shear modulus in each group
errorbar(x_rdvalues, y_Gs, err, '.r', 'MarkerSize', 50, 'LineWidth', 3) %make
points with standard deviation error bars
hold on
plot(Rd_extra, bvalue*Rd_extra.^mvalue, ':k', 'LineWidth', 3) %plot
regression
xlim([0 0.3])
ylim([0 2])
yticks([0 0.25 0.5 0.75 1 1.25 1.5 1.75 2])
set(gca,'FontSize',30, 'LineWidth', 2, 'FontName', 'Times')
set(gcf, 'Position',[100,100,1000,700])
hold off

%this code is repeated for each comparison (relative density, 5-7 defects,
strain rate, reusability, honeycomb vs EPS foam)

%% SMALL-SCALE IMPACT TESTING
initial_height = 25; %thickness of sample to determine stress/strain (mm)
initial_area = 94*94; %area of sample

%% Sample data (flat impact scenario)
importforce = xlsread('honeyflat1.xlsx'); %change name according to sample
(force in N)
importdef = xlsread('defmeasurements_imageJ.xlsx'); %position data from
ImageJ (mm)

positiondef = importdef(1:8,3); %position data from imageJ (mm)
deformation = positiondef - positiondef(1); %deformation data (mm)
```

141

```matlab
force = importforce(:, 4); %force data from loadcell in z-direction (N)
startforce = mean(force(1:8000)); %average force value before load is applied
forceadjusted = -(force - startforce); %zero force data
timelabview = 0.00002:0.00002:5; %time values according to sampling rate of
50000Hz
timelabview2 = timelabview(:); %make columns into rows
timelast = height(timelabview2); %number of data points

%find where force starts to increase (i.e. moment of impact)
i = 1;
while i < rows
    if forceadjusted(i) > 75 %using 75 N as preload
        start = i;
        i = rows+1;
    end
    i = i+2;
end
startforce = forceadjusted(start); %first force value after preload

%resample force data
timenew2 = timelabview2(start):(1/7500):timelabview2(timelast); %downsample
time values according to sample rate of high-speed camera
timenew3 = timenew2(:); %make columns into rows
forcenew = interp1(timelabview2(start:timelast),
forceadjusted(start:timelast), timenew3); %interpolate force values according
to down sampled time
forcenew2 = forcenew(:); %make columns into rows
points = height(deformation); %number of strain data points from first
contact to max strain
forcedata = forcenew2(1:points); %force data starting at preload (syncs with
strain)

%outcomes
HF1strain = deformation/initial_height; %strain data points
HF1stress = forcedata/initial_area; %stress data points
HF1peakstress = max(forceadjusted)/initial_area; %peak stress value
HF1energyabsorbed = trapz(HF1strain, HF1stress); %energy absorption per unit
volume until max strain

%this code is repeated for each sample

%% Sample data (angled impact scenario)

theta = 135; %angle for rotation matirx
importforce = xlsread('honeyoblique1.xlsx'); %change name according to sample
(force in N)

% stress data
force_i = importforce(:, 1); %force data from loadcell in the x-direction (N)
force_j = importforce(:, 3); %force data from loadcell in the z-direction (N)
force_s = force_i*cosd(theta) - force_j*sind(theta); %find shear force data
using rotation matrix
```

```matlab
force_c = force_i*sind(theta) + force_j*cosd(theta); %find compressive force
data using rotation matrix
force_s1 = force_s – mean(force_s(1:8000)); %zero shear force data
force_c1 = force_c – mean(force_c(1:8000)); %zero compressive force data
timelabview = 0.00002:0.00002:5; %time values according to sampling rate of
50000Hz
timelabview2 = timelabview(:); %make columns into rows
rows_s = height(force_s1); %number of shear data points
rows_c = height(force_c1); %number of compression data points

%find where shear force starts to increase (i.e. moment of impact)
i = 1;
while i < rows_s
    if force_s1(i) > 75 %using 75 N as preload
        start_s = i;
        i = rows_s+1;
    end
    i = i+2;
end

%find where compressive force starts to increase (i.e. moment of impact)
i = 1;
while i < rows_c
    if force_c1(i) > 75 %using 75 N as preload
        start_c = i;
        i = rows_c+1;
    end
    i = i+2;
end

force_s2 = force_s1(start_s:maxforcerow_s); %first shear force value after
preload
force_c2 = force_c1(start_c:maxforcerow_c); %first compressive force value
after preload

%outcomes
HO1stress_s = force_s1/initial_area; %shear stress data points
HO1stress_c = force_c1/initial_area; %compressive stress data points
HO1peakstress_s = max(force_s1(1:17000))/initial_area; %peak shear stress
value
HO1peakstress_c = max(force_c1)/initial_area; %peak compressive stress value

%this code is repeated for each sample

%% Average data for samples in the same group
% ex: flat, slow impact scenario)
HFslowpeakstresses = [HF1peakstress HF2peakstress HF3peakstress] %peak stress
values for all samples in a group
HFslowpeakstress_mean = mean(HFslowpeakstresses) %mean peak stress for group
HFslowpeakstress_stdev = std(HFslowpeakstresses) %standard deviation in peak
stress for group

HFslowenergyab = [HF1energyab HF2energyab HF3energyab] %energy absorption per
unit volue values for all samples in a group
```

143

```matlab
HFslowenergyab_mean = mean(HFslowpenergyab) %mean energy absorption per unit
volume for group
HFslowenergyab_stdev = std(HFslowenergyab) %standard deviation in energy
absorption per unit volume for group

%this code is repeated for each group

%% Example t-test
% flat, slow versus fast impact scenarios. outcome: peak stress)
diffmeans = HFfastpeakstress_mean – HFslowpeakstress_mean %difference in
means between groups
diffpercent = (diffmeans/HFslowpeakstress_mean)*100 %percent difference in
means between groups
[h,p] = ttest2(HFslowpeakstresses, HFfastpeakstresses) %t-test: h is whether
or not a statistical difference is found, p is p-value

%this code is repeated for all t-test comparisons

%% Example 1-way ANOVA
% flat, slow impact scenario. first vs second vs third repetition. outcome:
peak stress)
peakstresses = [HF1peakstress HF1bpeakstress HF1cpeakstress;
    HF2peakstress HF2bpeakstress HF2cpeakstress;
    HF3peakstress HF3bpeakstress HF3cpeakstress]; %columns are groups of data

means = [mean([HF1peakstress HF2peakstress HF3peakstress])
mean([HF1bpeakstress HF2bpeakstress HF3bpeakstress]) mean([HF1cpeakstress
HF2cpeakstress HF3cpeakstress])] %mean for each group
stds = [std([HF1peakstress HF2peakstress HF3peakstress]) std([HF1bpeakstress
HF2bpeakstress HF3bpeakstress]) std([HF1cpeakstress HF2cpeakstress
HF3cpeakstress])] %standard deviation in each group

[p,tbl,stats] = anova1(peakstresses, [], 'off'); %returns p-value, ANOVA
table, and info for multiple comparisons
c = multcompare(stats); %multiple comparisons post hoc tukey test

%this code is repeated for all 1-way anova comparisons

%% Example 2-way ANOVA
% flat, slow versus fast impact scenarios & first vs second vs third
repetitions. outcome: peak stress)
peakstresses = [HF1peakstress HF5peakstress;
    HF2peakstress HF6peakstress;
    HF3peakstress HF7peakstress;
    HF1bpeakstress HF5bpeakstress;
    HF2bpeakstress HF6bpeakstress;
    HF3bpeakstress HF7bpeakstress;
    HF1cpeakstress HF5cpeakstress;
    HF2cpeakstress HF6cpeakstress;
    HF3cpeakstress HF7cpeakstress]; %columns are groups of data, sets of 3
rows are groups of data

samplesize = 3; % Number of samples in each group
[~,~,stats] = anova2(peakstresses, samplesize);
```

144

```matlab
c1 = multcompare(stats, 'direction', 2);
c2 = multcompare(stats,"Estimate","row");

%this code is repeated for all 2-way anova comparisons

%% Example box and whisker plot
% flat, slow. honeycomb versus EPS foam. outcome: peak stress)
peakstresses = [HF1peakstress EF1peakstress;
    HF2peakstress EF2peakstress;
    HF3peakstress EF3peakstress]; %columns are groups of data

means = [mean([HF1peakstress HF2peakstress HF3peakstress])
mean([EF1peakstress EF2peakstress EF3peakstress])] %mean for each group
std = [std([HF1peakstress HF2peakstress HF3peakstress]) std([EF1peakstress
EF2peakstress EF3peakstress])] %standard deviation in each group

figure("Box and Whisker")
b = boxchart(peakstresses, 'MarkerStyle', 'x', 'MarkerSize', 10, 'LineWidth',
3)
hold on
plot(means, '.', 'MarkerSize', 30, 'Color', [0.6350 0.0780 0.1840])
set(gca,'FontSize',30, 'LineWidth', 2, 'FontName', 'Times')
set(gcf, 'Position',[100,100,750,750])
set(gca,'XTickLabel',{' '})
b.BoxFaceColor = [0 0.4470 0.7410]
box on
ylim([0.9 2.5])
yticks([1.0 1.2 1.4 1.6 1.8 2.0 2.2 2.4])

%this code is repeated for all comparisons
```

Appendix F – LabView Program

This appendix contains the LabVIEW back panel programming for the collection of data

from the load cell and high-speed camera in flat and angled impact testing (Chapter 3).
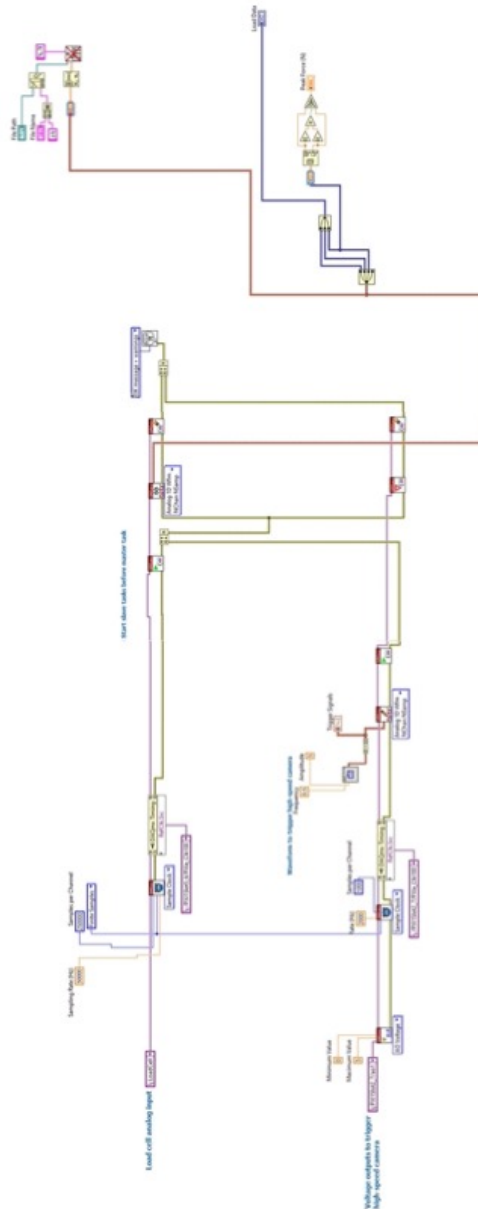

Figure F.1: Data Collection Program Back Panel
Triggers load cell and high-speed camera data collection.